

THESIS FOR THE DEGREE OF DOCTOR OF PHILOSOPHY

IN

MACHINE AND VEHICLE SYSTEMS

**Performance of Compact Heat Exchanger in  
Non-Perpendicular Cooling Airflows**

LISA HENRIKSSON

Department of Applied Mechanics  
CHALMERS UNIVERSITY OF TECHNOLOGY  
Gothenburg, Sweden, 2015

Performance of Compact Heat Exchanger in Non-Perpendicular Cooling Airflows

LISA HENRIKSSON

ISBN: 978-91-7597-164-3

©LISA HENRIKSSON, 2015

Doktorsavhandling vid Chalmers Tekniska Högskola

Ny serie nr 3845

ISSN: 0346-718X

Department of Applied Mechanics

Chalmers University of Technology

SE-412 96 Gothenburg

Sweden

Telephone +46 (0)31-772 1000

This document was typeset using L<sup>A</sup>T<sub>E</sub>X.

Printed at Chalmers Reproservice

Gothenburg, Sweden

---

# Performance of Compact Heat Exchanger in Non-Perpendicular Cooling Airflows

Lisa Henriksson  
Department of Applied Mechanics  
Chalmers University of Technology

## ABSTRACT

During recent years the main focus in the vehicle industry has been on cutting the fuel consumption and emissions as well as improving the vehicle performance. To be able to meet these demands additional systems are being introduced into the vehicle. These implementations do not only affect the engine power and the emission levels, they also tend to increase the operating temperature in the engine bay, which in turn increases the cooling demand. Therefore, a trend toward increased cooling performance for vehicles is also seen. There are a number of solutions to solve this demand and for heavy vehicles the most suitable way is to install additional heat exchangers positioned at other locations in the vehicle, due to the limited underhood space. These extra heat exchangers may not be located in the most appropriate position and it is not unusual that the airflow is not perpendicular to the heat exchanger core. For some vehicles today these types of installations can already be seen. Therefore, it is important to evaluate the effects on cooling airflows. Since both heat transfer and pressure drop over the heat exchanger will be affected by the angled airflow these parameters as well as the flow field characteristics, have to be analysed and evaluated.

This thesis presents a performance evaluation of standard automotive compact heat exchangers and their performance in non-perpendicular airflows. Four angles have been tested to predict variances in pressure drop, heat transfer rates and airflow characteristics. Laboratory experiments and 3D Computational Fluid Dynamics (CFD) simulations have been conducted to study the effects. Methods have been developed to simulate heat exchangers in angled conditions as well as internal parts of the core. The results have been correlated with the experiments to find similarities and deviations.

The results showed that the additional loss due to the angling of the heat exchanger, is due to the forced re-direction of the airflow into the core. This loss is increased with the magnitude of the angling. Neither the static pressure drop nor the heat transfer rate was significantly affected by the inclination angle of the heat exchanger relative to the airflow. To reduce the pressure drop within the installation the surrounding geometries had to be considered to prevent areas of losses. If a specific installation is going to be evaluated the information presented in this thesis is of great importance and could be used to find an optimal design for the system.

**Keywords:** Heat exchanger, Pressure drop, Heat transfer, Simulations, CFD, Experiments, Angled, Inclined



---

## LIST OF PUBLICATIONS

This thesis concludes the research carried out from 2012 to 2015 at Chalmers University of Technology. The thesis is based on the following publications, referred to by Roman numerals in the text:

- I Henriksson L., Dahl E., Gullberg P., Löfdahl L., CFD Method and Simulations on a Section of a Detailed Multi-Louvered Fin Where the Incoming Air is Directed at 90° and 30° Relative to the Compact Heat-Exchanger, SAE Paper 2013-01-2417, SAE Commercial Vehicle Engineering Congress, 2013
- II Larsson L., Dahl E., Gullberg P., Contet A., Skåre T., Löfdahl L., CFD Simulation and Experimental Investigation of Pressure-Drop Through 90° and 30° Angled Compact Heat-Exchangers Relative to the Oncoming Airflow, VTMS11, 2013
- III Henriksson L., Dahl E., Gullberg P., Löfdahl L., Experimental Investigation of Heat Transfer Rates and Pressure Drops through Compact Heat Exchangers, International Journal of Automotive Engineering 6, pp. 7-14, 2015
- IV Henriksson L., Dahl E., Gullberg P., Contet A., Skåre T., Löfdahl L., Experimental Investigation of Heat Transfer Rate and Pressure Drop through Angled Compact Heat Exchangers Relative to the Incoming Airflow, SAE International Journal of Commercial Vehicles 7 (2), pp. 448-457, 2014
- V Henriksson L., Dahl E., Gullberg P., Löfdahl L., CFD Simulations of one Period of a Louvered Fin where the Airflow is Inclined Relative to the Heat Exchanger, to be published in SAE International Journal of Engines 8 (4), 2015



---

## ACKNOWLEDGEMENTS

It would not have been possible to perform this work without all the support and inspiration that I have gained from both companies and individuals. First I would like to acknowledge my supervisor and examiner *Prof. Lennart Löfdahl* at Chalmers University of Technology for given me the opportunity to extend my knowledge within such an interesting topic.

The quality of the work would not have been possible to reach without having my supervisors at Volvo Group Truck Technology (GTT) by my side; *Erik Dahl* and *Dr. Peter Gullberg*. Whenever I have had a question, whatever the subject area, Erik was the man to ask. His wide knowledge is impressive and together with Peter's knowledge and positive/strict feedback they have been the perfect supervisors! We have had many interesting discussions involving theoretical phenomenon as well as basic fluid mechanics and thermal management. Both of you have been to a great help for me to learn topics within the area and I have really enjoyed solving all "interesting" problems, as Peter would have said. This is one of the things I will miss the most from my time as a PhD student.

I would also like to acknowledge my co-supervisors at Chalmers: *Prof. Simone Sebben* and *Prof. Ulf Häll*.

From Volvo GTT Gothenburg I would also like to thank *Torbjörn Wiklund*, *Dr. Sassan Etemad* and *Dr. Zinitha Chroner* for software support. I have had lots of tricky questions, which you have kindly helped me to solve. Moreover, I would like to acknowledge *Peter Nilsson*, *Kjell Andersson* and *Tommy Rosgardt* for giving me support and help with practical issues and showing interest into the project. In addition I would like to thank the division at Volvo GTT, which has been my main working location during my PhD study. I have had a great time with all of you and I have really appreciated working close to the industry.

Lots of thanks for all interesting discussions and support from my former colleagues in the Vehicle Aerodynamics research group; *Dr. Lasse Malmkjær Christoffersen*, *Dr. David Söderblom*, *Dr. Peter Gullberg*, *Dr. Christoffer Landström* and *Dr. Jesper Marklund*. We have had a really great time with lots of cheerful moments together. I would also like to thank the present researchers in the Vehicle Aerodynamics group; *Helena Martini*, *Alexey Vdovin*, *Lennert Sterken*, *Blago Minovski*, *Teddy Hobeika*, *Sabine Bonitz* and *Emil Ljungskog*.

There are several persons I would also like to acknowledge at TitanX Engine Cooling AB. *Dr. Thomas Skåre* and *Arnaud Contet* for being a part of the project and contributing with their knowledge. I would also like to acknowledge *Olof Erlandsson*, *Anders Brorsson*, *Magnus Nilsson* and *Bo Lindgren* for interesting discussions and for the help during the experiments.

At the fan test rig at Volvo GTT I had a great time while preparing and performing calibration of the Ruijsink probes, with the supervision of *Mikael Englund*.

Moreover, I would like to acknowledge *Andrew Dawkes* for proof reading the manuscript for this thesis and published documents. In addition I would like to thank *Prof. Bengt Sunden* and *Dr. Lin Wamei* at Lund University for the interesting discussions and for being a part of this project during the first two years.

---

A number of companies have contributed to this project; CD-adapco for supporting with licenses and software support at the London office and VINNOVA/FFI and the Swedish Energy Agency for the funding of this project.

Finally, I would like to thank my dear *family* and *friends* for all the support during my years at Chalmers.

---

## NOMENCLATURE

$A$	Area	$m^2$
$A_f$	Vehicle projected frontal area	$m^2$
$C$	Flow steam capacity	$J/sK$
$C_D$	Drag coefficient	—
$C_p$	Specific heat, at constant pressure	$J/kg K$
$C_v$	Specific heat, at constant volume	$J/kg K$
$C_\mu$	Empirical coefficient	—
$c$	Cold medium	—
$d$	Diameter	$m$
$d_h$	Hydraulic diameter	$m$
$e_0$	Total energy	$m^2/s^2$
$F_{res}$	Total resistance	$N$
$f$	Friction coefficient	—
$f_r$	Rolling resistance coefficient	—
$g$	Gravitational acceleration	$m/s^2$
$h$	Hot medium	—
$K$	Overall heat transfer coefficient	$W/m^2 K$
$KA$	Thermal conductivity	$W/K$
$K_x$	Loss coefficient	—
$k$	Turbulent kinetic energy	$m^2/s^2$
$k_x$	Coefficients	—
$L$	Length	$m$
$m$	Mass	$kg$
$\dot{m}$	Mass flow rate	$kg/s$
$n$	Rotational speed	$rps$
$P$	Perimeter	$m$
$P_i$	Inertial resistance	$kg/m^4$
$P_R$	Power	$W$
$P_r$	Porous resistance	$kg/m^3 s$
$P_v$	Viscous resistance	$kg/m^3 s$
$Pr$	Prandtl number	—
$p$	Pressure	$Pa$
$Q$	Heat flux	$W$
$q$	Volume airflow rate	$m^3/s$
$R$	Specific gas constant	$J/kg K$
$Re$	Reynolds number	—
$S$	Sutherland's constant	—
$S_p$	Source term due to porous resistance	$kg/m^2 s^2$
$T$	Temperature	$K$
$t$	Time	$s$
$V$	Velocity	$m/s$
$v$	Local velocity	$m/s$

---

## Greek Letter Symbols

$\alpha$	Angle	$^{\circ}$
$\alpha_c$	Convective heat transfer coefficient	$W/m^2K$
$\Delta$	Denotes difference	—
$\delta_{ij}$	Kronecker delta	—
$\varepsilon$	Dissipation	$m^2/s^3$
$\varepsilon_x$	Efficiency	—
$\xi$	Expansion loss factor	—
$\lambda$	Thermal conductivity	$W/mK$
$\mu$	Dynamic viscosity	$kg/ms$
$\mu_t$	Turbulent viscosity	$kg/ms$
$\nu_t$	Kinematic viscosity	$m^2/s$
$\rho$	Density	$kg/m^3$
$\tau$	Viscous stress	$N/m^2$
$\omega$	Specific rate of dissipation	$1/s$

## ABBREVIATIONS

AC	Air Condition
CAC	Charge Air Cooler
CAD	Computer Aided Design
CFD	Computational Fluid Dynamics
DES	Detached Eddy Simulation
DNS	Direct Numerical Simulation
EGR	Exhaust Gas Recirculation
FVM	Finite Volume Method
GTT	Group Trucks Technology
ITD	Inlet Temperature Difference
LES	Large Eddy Simulation
NTU	Number of Transfer Units
RANS	Reynolds Averaged Navier Stokes
SA	Surface Averaged
SCR	Selective Catalytic Reduction
UTM	Underhood Thermal Management
WHR	Waste Heat Recovery

## Contents

<b>1</b>	<b>Introduction</b>	<b>1</b>
1.1	Project background . . . . .	2
1.2	Project objectives . . . . .	4
<b>2</b>	<b>Theory and preceding work</b>	<b>5</b>
2.1	Engine cooling system . . . . .	5
2.1.1	Compact heat exchanger properties . . . . .	7
2.2	Cooling drag and cooling airflows . . . . .	9
2.2.1	Cooling module positions effects on vehicle aerodynamics	10
2.3	Numerical expressions . . . . .	12
2.3.1	Porous media model . . . . .	15
2.4	Preceding work . . . . .	15
2.4.1	Preceding work based on experiments . . . . .	16
2.4.2	Preceding work based on simulations . . . . .	18
<b>3</b>	<b>Method</b>	<b>21</b>
3.1	Heat exchanger specification . . . . .	21
3.1.1	Definition of the experiments . . . . .	22
3.2	Experimental measurements . . . . .	25
3.2.1	Angled heat exchangers relative to the incoming airflow .	25
3.2.2	Calibration of Ruijsink microprobes . . . . .	33
3.3	Numerical simulations . . . . .	35
3.3.1	Simulations of the experimental set-up . . . . .	36
3.3.2	Simulations of one period of a fin . . . . .	38

<b>4</b>	<b>Results and discussion</b>	<b>43</b>
4.1	Airflow observations of experimental set-up . . . . .	43
4.2	Experimental results . . . . .	47
4.2.1	Isothermal experimental results . . . . .	48
4.2.2	Thermal experimental results . . . . .	52
4.2.3	Heat exchanger layouts for angled installations . . . . .	57
4.3	CFD simulations of the experimental set-up . . . . .	61
4.4	CFD simulations of one period of a fin . . . . .	66
4.4.1	Constant mass airflow rate . . . . .	66
4.4.2	Constant velocity in the x-direction . . . . .	75
4.4.3	Thermal simulations . . . . .	80
4.5	Confirmation of airflow distribution . . . . .	82
4.6	Final remarks . . . . .	83
4.6.1	Ideas to decrease the static pressure drop . . . . .	83
4.6.2	Consequences of increased size of the heat exchanger . . .	84
<b>5</b>	<b>Conclusions</b>	<b>85</b>
<b>6</b>	<b>Summary of papers</b>	<b>87</b>
	<b>References</b>	<b>91</b>
<b>I</b>	<b>Appendix</b>	<b>159</b>
<b>A</b>	$\varepsilon - NTU$ method	159
<b>B</b>	Influences of porosity effects and core mesh for simulations of the experimental set-up	162
<b>C</b>	Fan laws	165
<b>D</b>	Pressure drop for variations in fin geometry	166
<b>E</b>	Convergence strategy for a period of a fin in an arrangement of $10^\circ$	167

---

## 1 Introduction

Trucks are important for transporting goods from one place to another. Around 90% of all freight transportation is carried out by commercial vehicles [1] and even if transportation by trains or ships are increasing, the part carried out by commercial vehicles still remains dominant. According to the information presented in [2] the number of registered trucks in USA has increased every year since the 1970's, a similar trend is also seen in many other countries. The demand on the transportation system will continue to increase as a result of the consumer society we live in, and due to increased wealth of the world population. To fulfil everybody's needs, increased demand for transportations of goods will be dominated by commercial vehicles [3].

As the number of vehicles increases the fuel demand will increase as well. In 2011 data presented that stated approximately one third of the energy consumed in Europe was used by the transportation sector [4]. In USA this value was lower, where approximately 19% was from the medium and heavy-duty market [5].

A consequence of the combustion process of fossil fuel is the emissions, whose negative effects on our planet we are all aware of. Since the number of vehicles is increasing the impact on the planet is growing quickly. Emissions from vehicles which have negative effects on the Earth are: carbon dioxide ( $CO_2$ ), carbon monoxide ( $CO$ ), nitrous oxide ( $NO_X$ ), hydrocarbon ( $HC$ ) and particulate matter ( $PM$ ). In 2008 31% of all  $CO_2$  emissions in USA was from the transportations sector, were 68% was from medium and heavy-duty busses and trucks. Medium and heavy-duty trucks account for 22% of all transportation related green-house gases in the U.S. In figure 1.1 the amount of green-house gases from different vehicle sectors are presented [6]. Note that the emissions from trucks reach similar levels as passenger vehicles. The green-house gases from heavy-duty trucks have increased by over 72% for the period 1990 – 2008. The corresponding value for passenger cars is approximately 20% [7].

With this information together with the environmental debates, higher fuel prices and the decrease of cheap crude oil, have all resulted in vehicle manufacturers being obliged to develop more energy-efficient vehicles. Thus, every part of the vehicle must be optimized to provide an emission and fuel efficient transportation solution.

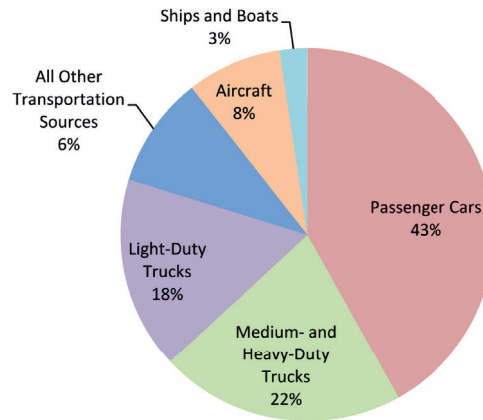


Figure 1.1: Green-house gas for different transportation sectors [6].

## 1.1 Project background

The automotive industry faces big challenges with ever stricter emissions legislation and increased fuel prices. To sell vehicles that fulfil these regulations, manufacturers implement optimized systems and sub-systems for their vehicles. Charge Air Cooler (CAC), Selective Catalytic Reduction (SCR), Exhaust Gas Recirculation (EGR), Waste Heat Recovery (WHR), diesel particulate filter and fuel injection systems, are examples of such improvements. At the same time a higher power outputs from the engines are seen for most vehicles. A consequence when introducing some of these systems, together with increased engine power, is the increased demand for cooling. Higher power output from the engine requires more engine cooling, since higher temperatures are developed. When introducing a cooled EGR system, a portion of the exhaust gases are re-entered into the engine for a second combustion; although, before it can enter it has to be cooled by the cooling system, thus increasing the cooling demand. Other after-treatment systems are added after the engine, which will generate additional back-pressure. The fuel injection systems are optimized for reducing emissions rather than for cooling. Consequently, these systems affect the cooling demand in one way or another. To meet upcoming emissions legislation the temperature in the engine bay also tends to increase more, according to [8], hence increasing the cooling demand. To ensure sufficient cooling in the future, the cooling module and its location must be investigated to find alternative solutions to maintain or increase its effectiveness and to decrease the overall parasitic losses.

Numerous investigations are on-going concerning alternative ways to propel vehicles. In the future there might not be internal-combustion engines as the main energy source. Instead hybrid solutions, electrically-driven wheels, batteries etc. could be proposed as solutions. Each technical solution will place different demands on the cooling module. For example, batteries must have

their temperature controlled to maintain performance and lifetime [9]. This is a significant challenge for the cooling module.

To be able to meet upcoming emissions regulation and market requirements, additional systems will be required and a further increase in cooling demand will be seen. To fulfil the cooling demand increased efficiency of the cooling device or an increased size of the cooling package are required. There are many investigations, looking to increase the effectiveness of the cooling device, for example [10, 11, 12, 13, 14, 15, 16, 17, 18]. Due to limitations of space at the front of the vehicles, behind the grill, an increase in size of the cooling device could be difficult to implement. Therefore, alternative positions of additional heat exchangers have to be evaluated. The truck in figure 1.2 shows possible positions for additional heat exchangers. What is common for many of these is that the airflow is not necessarily entering the heat exchanger core squarely, as is the case for the cooling package mounted at the front. Heat exchangers, where the airflow enters non-perpendicular are already on the market for some vehicles. The positions employed for buses are for example: in the front, at the rear, in the middle and on the roof. The main reason for the cooling module location for buses is due to the different engine and Air Condition (AC) condenser positions, resulting in several cooling module positions. For trucks, the most common cooling package location is in the front, behind the grill.



Figure 1.2: Possible heat exchanger positions for a truck.

Another motivation for this project is the discussions regarding the re-definition of the length regulation for trucks [19]. The legislation within Europe is defined as a total length of the complete tractor and trailer unit. Different countries allow various maximum lengths. Since the tractor is included in the length definition cab-over-engine designs of the tractor are common in these countries. In USA the length legislation only limits the trailer unit, which allows a longer tractive unit. Therefore, it is more common to have the conventional “front-engine” design of the tractor, which in general is longer than a cab-over-engine design. The discussion about the redefinition of the length is that the cab should be allowed to be extended, to permit a more rounded shape of the cabin. This extension zone should work as a deformable zone to improve impact incidents with pedestrians as well as with other vehicles. The change in design will improve the field of vision of the driver as well as improve the aerodynamics of the vehicle. As the zone should be deformable, heat exchangers could be installed within this area. To improve heat transfer rates and static pressure drop the heat exchangers could be installed at an angle relative to the air intakes.

Investigations regarding permitting longer vehicle combinations and heavier gross weights for certain applications are also on-going. One example is the Volvo's ETT Project, which is an extra large round timber hauler, which has a gross combination weight of 100 ton. In the future the engine power for heavy-duty trucks will be further increased for some markets. These factors increase the cooling demand for these vehicles, which is another argument for carrying out this investigation.

## 1.2 Project objectives

The main objective of this thesis was to investigate the effects of having a compact crossflow heat exchanger angled relative to the incoming airflow. Static pressure drops, heat transfer rates and airflow characteristics were evaluation parameters. The results should give an indication of heat exchanger thickness and magnitude of inclination for a specific installation in a vehicle. A second aim was to develop and evaluate engineering methods of simulating angled heat exchangers and validate the methods with experimental results.

---

## 2 Theory and preceding work

The focus for this project has been to evaluate heat exchanger performance for non-perpendicular airflows. For such installations in a vehicle supporting theory of vehicle technology and various methods are required to generate an optimal solution. In this chapter information regarding theory and preceding work carried out for angled heat exchangers relative the airflow are presented.

### 2.1 Engine cooling system

Underhood Thermal Management (UTM) has become an important topic within the automotive industry. The engine for on-road vehicles is cooled by mainly two principles. Direct cooling is the first and the oldest method, where heat is rejected to the air flowing through the underhood as a result of the forward motion of the vehicle. For todays vehicles this method does not generate enough cooling and an additional liquid cooling system is required. This is an indirect air cooling system, consisting of a number of heat exchangers and other components, to fulfil the thermal requirements of the vehicle. Most vehicles have at least three heat exchangers: AC condenser; CAC; and the coolant radiator. The AC condenser is part of the climate system, used to dissipate heat when cooling in the driver compartment is required or to de-humidify the air entering the cab. The CAC cools the intake air from the turbo before it enters the combustion chamber. The radiator cools the coolant, which is circulated through the engine and the transmission. Maximum heat-rejection rate for each component for a heavy-duty truck is typically:  $8kW$  for the AC condenser;  $80kW$  for the CAC; and  $220kW$  for the radiator; depending on driving conditions and ambient temperature [8]. In figure 2.1 a schematic picture of the cooling system is shown. There are two cooling circuits in the figure; one for the radiator and one for the CAC. The radiator circuit includes the coolant pump, which transports the coolant around the circuit. In the engine the coolant is heated, as a consequence of the combustion process, and thereafter flows to the thermostat, which opens and guides the cooling medium into the radiator if the coolant temperature is high enough. Otherwise the coolant flows through the shorter circuit and bypasses the heat exchanger, and is thereafter transported to the coolant pump and engine once again. The CAC circuit starts by air entering the compression part of the turbocharger where the air is compressed, resulting in a pressure and temperature increase. Thereafter the air flows through the CAC to lower the temperature and to increase the density of air, to increase the efficiency of the combustion process. After combustion the exhaust gases exit through the expansion part of the turbocharger, this expansion propels the compression side. A second effect of cooled charge air is the lowered temperature of the combustion, which lowers the  $NO_x$  generation. Some vehicles have additional thermal management systems. For example EGR cooling, where part of the

exhaust gas is recirculated into the combustion chamber for a second combustion to either control emissions or to improve engine efficiency. To recover some of the energy in the exhaust gas WHR systems can be implemented into a vehicle. There have been many studies performed within this area, as well as on-going [20, 21, 22]. Some companies claim that they can reduce the fuel consumption by 7.5% for a heavy-duty truck by implementing a waste-heat recovery system [23]. Though, to recover the energy into useful work the process involves cooling, which will continue to increase the cooling requirement of future vehicles.

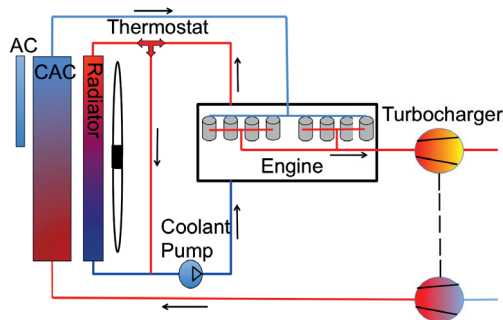


Figure 2.1: Schematic picture of the cooling system and cooling circuits.

For heavier vehicles the diesel engine is an efficient power-delivery system and it is the most common type of propulsion system currently used. Though, it is far from 100% efficient. The maximum efficiency for a compression ignition engine is up to 45% [8], where the remaining energy is equally distributed to the cooling system and into the exhaust. If the vehicles were more efficient less cooling would be needed and lower fuel consumption would be seen. In figure 2.2 a diagram of the energy distribution for this type of engine is shown.

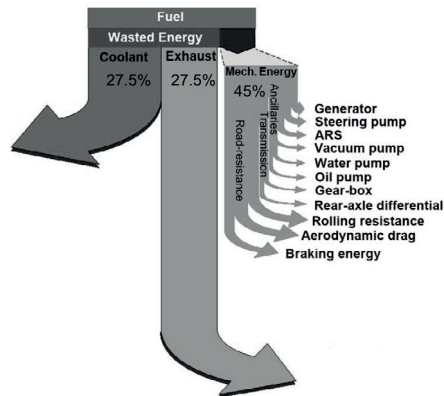


Figure 2.2: Energy distribution in a vehicle.

The cooling demand is dependent on the engine power, which in turn is depen-

dent on the driving condition. A higher heat transfer rate is usually required when the engine has to deliver a higher power output and for high ambient temperatures. Higher ambient temperatures make the driver also want to use the AC in the cab compartment to cool, which further increases the cooling demand. To prevent engine overheating in critical driving situations, the cooling module must be dimensioned for extreme conditions. The fan will operate less frequently for driving conditions not requiring much cooling; since ram-air flow is likely to be enough to obtain sufficient cooling. From earlier tests carried out at Volvo GTT [24] it has been seen that the fan had an average operation time of 2% of a typical highway driving cycle.

### 2.1.1 Compact heat exchanger properties

Compact heat exchangers are widely used within a variety of domestic, industrial and vehicle applications. There are many different internal designs of plate-finned heat exchangers, this work is based on the louvered fin type. For automotive applications the multi-louvered finned and flat tube heat exchanger are commonly used for enhancing air-side heat transfer [25]. This type of heat exchanger is for example used as radiators, evaporators, condensers and heating elements. In figure 2.3 the design of the heat exchanger is shown. The core consists of tubes and fins, where the tubes are mounted between the tanks, where the cooling fluid passes through. In between the tubes, there are fins, where the air is flowing through the core. The fins are louvered in order to break up the boundary layer, to increase the heat transfer rate. As a consequence of the increased mixing of air the static pressure drop through the core also increases. For low Reynolds numbers the airflow is mainly aligned with the stream-wise direction and for higher Reynolds numbers the flow is louver-directed [26, 27]. It has been shown that the louver-directed airflow has a positive impact on heat transfer [10]. Within the tubes the walls are commonly dimpled in order to have a transition from laminar to turbulent flow to increase heat transfer.

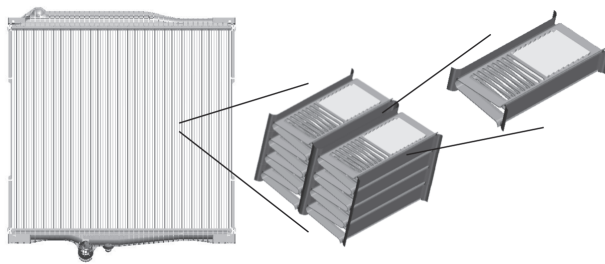


Figure 2.3: A compact louvered finned heat exchanger, including detail views.

A heat exchanger is defined by a number of parameters, shown in figure 2.4. The left picture shows a plane of the centreline of the core, while the right picture shows the entrance to the core.

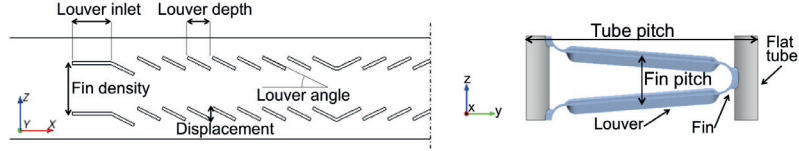


Figure 2.4: Definition of heat exchanger parameters.

### Pressure drop

The pressure drop over a heat exchanger is normally formed by four components; entrance loss, losses due to acceleration of the medium, friction losses and exit losses, according to Kays and London [28]. The pressure drop expression can be re-written in a simplified form, as equation 2.1, expressed as the dynamic pressure multiplied by the loss coefficients.  $K_{in}$  and  $K_{out}$  are inlet and exit loss coefficients due to the abrupt contraction at the entrance and the abrupt expansion at the outlet, which are dependent on the geometry. The entrance effect will act as pressure drop and the exit effects as pressure rise, according to Kays and London [28].  $f$  is the friction loss coefficient, which describes the losses due to friction. The pressure drop will increase when adding high temperature into the system since the specific volume is increased due to decreased density, resulting in an accelerating airflow. This loss is defined as  $K_{acc}$ . Due to this effect, together with an increased friction loss, the pressure drop over the core will increase. The pressure drop is highly dependent on the internal design of the core and the velocity of the air.

$$\Delta p = \frac{\rho V^2}{2} \left( K_{in} + K_{acc} + f \frac{L}{d_h} + K_{out} \right) \quad (2.1)$$

### Thermal properties

Heat exchangers are subject to the incoming airflow as a result of the forward motion of the vehicle. When more cooling is required and the ram air is not sufficient the fan has to operate to increase the mass airflow through the cooling package. This fluid motion of the air through the core will result in forced convection. The heat transfer for a two-fluid heat exchanger is a combination of convection and conduction from the hot to the cold fluid. Conduction takes place within the solid walls of the tubes and the fins, and convection takes place inside the tubes (hot side) as well as at the air-side (cold side). The heat transfer rate is described for the hot or the cold side separately. Since the rejected heat from the hot fluid should correspond to the absorbed heat of the cold fluid the heat transfer rates should be equal, due to the heat balance. Expressions of the heat transfer for the hot and the cold side are defined in equations 2.2 and 2.3. Where  $C_h$  and  $C_c$  are the flow-stream capacity rates and are the product of the mass flow rate and the specific heat coefficient for each fluid. To calculate the

performance of a crossflow heat exchanger the  $\varepsilon - NTU$  (Number of Transfer Units) method can be applied, which is described in Appendix A.

$$Q_h = C_h(T_{h,in} - T_{h,out}) \quad (2.2)$$

$$Q_c = C_c(T_{c,out} - T_{c,in}) \quad (2.3)$$

## 2.2 Cooling drag and cooling airflows

The air passing through the inlet grill, cooling module and the underhood area, gives rise to aerodynamic resistance, referred to as cooling drag [29]. This resistance contributes to a substantial part of the aerodynamic drag of the vehicle created by the pressure drop at the entrance and exit of the engine bay, as well as the underhood area itself [30]. At higher vehicle speeds, such as highway driving, the ram-air is usually adequate to meet the cooling demand. The airflow through the inlet grill, which is not needed for cooling, will act as an aerodynamic resistance for the vehicle and will be present whenever the vehicle is moving forward. This resistance will be present even though no cooling is required. To reduce the resistance when cooling is not needed, devices that restrict the amount of air entering can be implemented. These devices are referred to as for example grill shutter, which is an old technique, where the complete or parts of the air intake can be covered. When no device is used a substantial part of the vehicle power requirement is due to the air flowing through the cooling module and the underhood area [29]. The cooling drag for a passenger vehicle is typically somewhere around 5 – 10% of the total drag. Experiences have shown that the corresponding value for a truck is a little lower, where the value varies for different combinations of the tractor and the trailer unit. Generally the cooling drag as a percentage of the total drag is lower for a vehicle with higher aerodynamic resistance. A study has shown a value of approximately 5% cooling drag of the total drag, where the length of the vehicle combination was 9.2m [31]. Kuthada and Wiedemann [29] investigated the cooling airflow for a sedan passenger vehicle and obtained a cooling drag of approximately 4%.

The pressure drop through the components in the engine bay can be illustrated as in figure 2.5, defined by Gullberg [8]. The stagnation point of the vehicle is at a distance of  $X = 0$  and behind this point the grill, the heat exchangers and the fan are located. The black line, represents full load of the fan and a low vehicle speed. This is usually a common dimensioning criteria, since the largest amount of cooling is required for vehicles operating fully laden, driving in a hilly environment, and using maximum power; therefore maximum cooling is usually required for lower vehicle speeds when the ram-air is low and the fan is the main source of air passing through the cooling module. Due to the low vehicle speed the ram air contribution is low, and as an effect of high fan speed the volumetric flow rate is high, generating a high pressure drop over the components. The second scenario is the grey line, representing cruise condition

at a higher vehicle speed. The ram air is increased while the pressure drop is decreased.

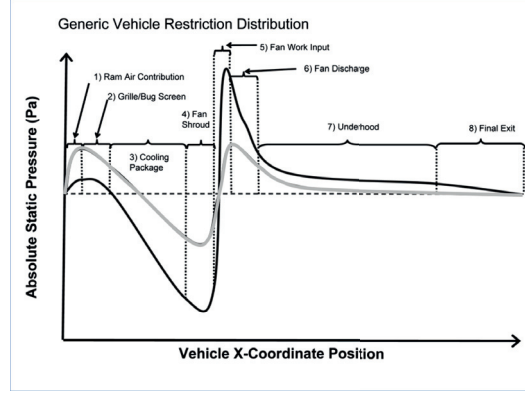


Figure 2.5: Static pressure drop through the engine bay [8].

### 2.2.1 Cooling module positions effects on vehicle aerodynamics

When looking into new cooling module positions it is important to consider their effect on the vehicle aerodynamic resistance. Placing the air intake and outlets at other positions will affect the resistance of the vehicle, as well as the amount of air entering and exiting the cooling air intakes in a positive or negative manner. A vehicle is subjected to a number of resistance forces when driving on a road. The total resistance for the forward motion is defined by Wong [32], by equation 2.4.

$$F_{res} = m \frac{dV}{dt} + f_r mg \cos \alpha + mg \sin \alpha + \frac{1}{2} C_D \rho A_f V^2 \quad (2.4)$$

The first term is inertial resistance such as acceleration, the second term is the rolling resistance with,  $f_r$ , as the rolling resistance coefficient, the third term denotes the climbing resistance, and the last term is the aerodynamic forces. Hence, the aerodynamic drag for a vehicle is dependent on the air density,  $\rho$ , the frontal projected area of the vehicle,  $A_f$ , the vehicle velocity,  $V$ , squared and the drag coefficient,  $C_D$ . The last mentioned parameter is dimensionless and is used to quantify the resistance of a body in a fluid environment.

As a consequence of increased fuel prices the aerodynamic resistance of vehicles has become more important in recent years. The aerodynamic resistance is a result of the vehicle being forced through the surrounding air. It can be reduced, and hence decrease fuel consumption, by making appropriate design changes to the body. The aerodynamic drag consists of friction and pressure drag. Friction drag is the resistance due to the shearing motion of the airflow near the surface; while pressure drag is the difference in pressure around the body. For a truck the aerodynamic drag is usually higher compared to a passenger car since it

has a larger frontal area and a higher  $C_D$  value due to its squared shape. At zero degree yaw of the airflow the  $C_D$  value for the truck as in figure 1.2 is approximately 0.4, while passenger cars have a value around 0.3. The  $C_D$  value is dependent on the wind direction and heavy vehicles are more sensitive to yaw conditions since they have a large side area. This is especially important for longer vehicle combinations.

On a level road, at constant speed, the driving resistance is mainly a consequence of rolling resistance and aerodynamic drag; where the aerodynamic drag becomes dominant at approximately  $80\text{km/h}$  [33]. In figure 2.6 the power demand to overcome the aerodynamic drag and the rolling resistance in  $\text{kW}$ , versus the vehicle speed is plotted for a fully-laden heavy vehicle. In the figure it can be seen that rolling resistance is linear while the aerodynamic resistance increases by the cube of velocity. To reduce the aerodynamic drag, the frontal area of the vehicle or the drag coefficient has to be decreased. Since heavy vehicles frequently operate above the velocity where aerodynamic drag is dominant, the aerodynamic resistance must be considered when investigating new cooling air intakes and outlets positions.

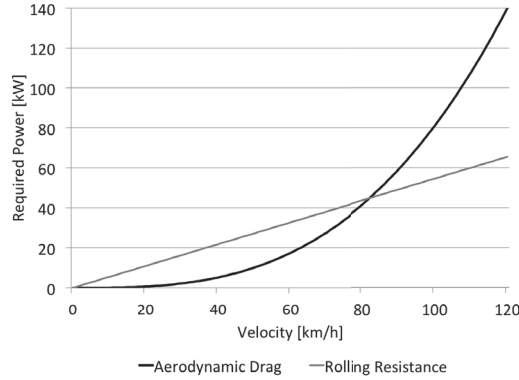


Figure 2.6: Engine power required to overcome the aerodynamic drag and the rolling resistance, versus the vehicle velocity.

In front of the vehicle the stagnation point is located where the velocity is zero and the static pressure has its maximum value. Along and behind the vehicle separated regions are created since the air cannot stay attached to the surface when the adverse pressure gradient is too large. In these areas, including the base wake behind the vehicle, the pressure is low. The larger the difference in static pressure around the vehicle, the larger the pressure drag and hence an increased  $C_D$  value. Separated areas are common for trucks since they have a squared design. The body is therefore dominated by pressure drag and is referred to as a bluff body. A study performed by Martini et al. [34] showed that approximately 95% of the total drag for a truck as in figure 1.2, is due to pressure drag. By making well considered design changes the separated areas can be reduced, decreasing the pressure drag, along with the  $C_D$  value. For a

body that has almost no separated areas, such as a tear-drop shaped body, the drag coefficient will be friction-drag dominated and is then referred to as being a slender body. To increase the airflow through the cooling module, without using the fan, the air inlet should be positioned in areas of high pressure without separated flows and the outlet should be positioned in low-pressure regions. The airflow through the cooling module would then be pressure driven. As mentioned in Chapter 2.2 the overall aerodynamic drag will increase due to the pressure drop over the grill, friction losses through the heat exchanger cores and on the walls, flow interaction at the air inlet, and turbulence and separation at the air outlet [30].

### 2.3 Numerical expressions

The governing equations of fluid dynamics consist of three conservation laws; conservation of mass, momentum and energy. These equations are based on the Reynolds Transport Theorem, which establish a relation between system rates of change and control volume surface and volume integrals. Hence, for a pre-defined control volume the theorem describes the quantity of the original volume of the control volume and what enters and exits to it. The motion of the fluid is described by the Navier Stokes equations, which are special cases of the conservation laws. These include the continuity, the momentum and the energy equations [35]. These three equations are displayed in equation 2.5, 2.6 and 2.7 respectively for a compressible fluid [36].

Continuity equation:

$$\frac{\partial \rho}{\partial t} + \frac{\partial}{\partial x_j}(\rho u_j) = 0 \quad (2.5)$$

Momentum equation:

$$\frac{\partial}{\partial t}(\rho u_i) + \frac{\partial}{\partial x_j}(\rho u_i u_j + p \delta_{ij} - \tau_{ji}) = S_p \quad (2.6)$$

Energy equation:

$$\frac{\partial}{\partial t}(\rho e_0) + \frac{\partial}{\partial x_j}(\rho u_j e_0 + u_j p + Q_j - u_i \tau_{ij}) = 0 \quad (2.7)$$

These equations are non-linear partial differential equations, which need to be modelled and discretized to be practically solvable for larger problems. The parameter on the right-hand side,  $S_p$ , is a source term, defined further on. To solve the energy equation there are some parameters that need to be defined. The ideal gas law, defined in equation 2.8, is used to express the density as a function of temperature and pressure; where  $R$  is the specific gas constant and  $P_{abs}$  is the absolute pressure.

$$\rho = \frac{P_{abs}}{RT} \quad (2.8)$$

In the momentum and energy equation the viscous stress,  $\tau_{ij}$ , has to be defined. For a Newtonian fluid it is defined by equation 2.9, where  $\mu$  is the dynamic viscosity.

$$\tau_{ij} = 2\mu \left( \frac{1}{2} \left( \frac{\partial u_i}{\partial x_j} + \frac{\partial u_j}{\partial x_i} \right) - \frac{1}{3} \frac{\partial u_k}{\partial x_k} \delta_{ij} \right) \quad (2.9)$$

There are two more parameters in the energy equation that have to be defined; the total energy,  $e_0$ , and the heat flux,  $Q_j$ . The heat flux,  $Q_j$ , is given by Fourier's law defined in equation 2.10, where  $Pr$  is the Prandtl number seen in equation 2.11, [36, 37]. The total energy,  $e_0$ , is defined by equation 2.12, with the specific heat at constant volume,  $C_v$ .

$$Q_j = -\lambda \frac{\partial T}{\partial x_j} = -C_p \frac{\mu}{Pr} \frac{\partial T}{\partial x_j} \quad (2.10)$$

$$Pr = \frac{C_p \mu}{\lambda} \quad (2.11)$$

$$e_0 = C_v T + \frac{u_k u_k}{2} \quad (2.12)$$

Parameters used in the above equations are the specific heat at constant pressure,  $C_p$ , and the thermal conductivity,  $\lambda$ . For more information about these expressions, see [35, 36, 38]. The relationship between the specific heat at constant volume and pressure is the gas constant;  $C_p - C_v = R$ .

Depending on the problem different methods can be applied to model the Navier Stokes equations, for example by using: Reynolds Averaged Navier Stokes (RANS) based simulations, Large Eddy Simulation (LES) or Detached Eddy Simulation (DES). The Direct Numerical Simulation (DNS) model covers all physical phenomena that have to be solved, but this requires considerable computer resources since it numerically solves the Navier Stokes equations without any turbulence model. It is important to consider the specific problem in order to simulate the flow-field by a suitable model, to obtain results as similar to reality as possible.

For the RANS based solvers an engineering simplification of the Navier Stokes equations is made to be able to solve the equations. This simplification is modelled with the so-called Reynolds decomposition, where each transport parameter is divided into a mean, denoted by a 'bar', and a fluctuating, denoted by a 'prime', value. In equation 2.13 this is seen for the velocity.

$$u_i = \bar{u}_i + u_i' \quad (2.13)$$

The mean value in this expression corresponds to equation 2.14, where  $t$  denotes a time step.

$$\overline{u_i} = \frac{1}{t} \int_0^t u_i dt \quad (2.14)$$

For steady simulations the equations are thereafter time-averaged. After re-writing the equations there will be one additional non-linear term,  $\overline{\rho u'_j u'_i}$ , in the momentum transport equation, known as the Reynolds stresses. Since there are more unknown parameters than equations, this defined turbulent term has to be modelled by making assumptions to be able to solve the equations system.

Two frequently used models to predict the turbulence behaviour for the RANS-based turbulence models are the eddy viscosity model, and the Reynolds stress transport model [37]. The eddy viscosity model uses the turbulent viscosity,  $\mu_t$ , to model the Reynolds stress tensor as a function of mean flow quantities, where the most common model is the Boussinesq approximation [37]. Examples of Eddy Viscosity turbulence models are the Two-equation models, which introduce two extra transport parameter equations, which represent the turbulent properties of the flow that have to be solved to close the equation system. The two-equation models include for example the standard  $k - \varepsilon$ , the Realizable  $k - \varepsilon$  and the *SST*  $k - \omega$  (NSC) models.  $k$  is a transport variable and is the turbulent kinetic energy, which determines the energy in the turbulence,  $\varepsilon$  is the turbulent dissipation and determines the rate of dissipation of the turbulent kinetic energy.  $\omega$  is the specific dissipation of the turbulent kinetic energy and determines the scale of the turbulence. The relation of  $k - \varepsilon$  is as in equation 2.15, where the parameter  $C_\mu$  is an empirical coefficient. For  $k - \omega$  the relation is as in equation 2.16, where  $\nu_t$  is the kinematic eddy viscosity.

$$\mu_t = \rho C_\mu \frac{k^2}{\varepsilon} \quad (2.15)$$

$$\nu_t = \frac{k}{\omega} \quad (2.16)$$

To find the relation between  $k - \varepsilon - \omega$  the two previous equations with equation 2.17 are combined, resulting in equation 2.18.

$$\nu_t = \frac{\mu_t}{\rho} \quad (2.17)$$

$$\omega = \frac{\varepsilon}{k C_\mu} \quad (2.18)$$

### 2.3.1 Porous media model

Resolving the geometry of a heat exchanger with the tubes and baffles is complex; its large surface with boundary layer is complex to model and should result in high calculation time and cost. Hence, for practical reasons heat exchangers are modelled as porous media. The porous media models the pressure drop over the heat exchangers without resolving its detailed geometry. Each heat exchanger can then be modelled as a rectangular volume where the porosity model is applied. The porosity is defined by the inertial resistance,  $P_i$ , and the viscous resistance,  $P_v$ , resulting in a porosity value per unit length,  $P_r$  [37]. The relationship between the parameters is presented in equation 2.19, which is based on the Darcy-Forchheimer equation. The parameters are obtained from pressure drop test-bench measurements for each component in isothermal condition. These values are thereafter applied for both thermal and isothermal simulations. The magnitudes of the constants are dependent on the internal design of the core and the airflow through it. Therefore, the coefficients apply to a specific heat exchanger. The porosity is added as a source term,  $S_p$ , in the momentum equation 2.6 and is given by equation 2.20.

$$P_r = P_v + P_i V \quad (2.19)$$

$$S_p = -P_r V \quad (2.20)$$

## 2.4 Preceding work

There are a large number of preceding investigations regarding experiments on heat exchangers and their design parameters. Within the area of inclined airflow relative to heat exchangers, some experiments have been carried out. Simulations on the internal parts of the core of the heat exchanger have also been studied, but without the effect of inclining the entrance airflow direction. Previous work that has been carried out within these areas is summarised in the following sub-sections.

For investigations on inclined heat exchangers relative to the airflow there are two methods that can be applied: either a constant; or a variable height of the entrance duct. Figure 2.7 shows the two methods. For the first scenario: *A*, the size of the heat exchanger core, subjected to the incoming airflow, will vary for all inclinations; for the second scenario, *B*, the size of the heat exchanger core will be unchanged independent of the inclination angle. It should be noted that the velocity of the airflow within the core will vary between the two scenarios for a constant mass airflow definition. The velocity in the core for scenario *A* at 30° will be half compared to the 90° arrangement since the core area is doubled. For scenario *B* the core area is constant, resulting in the same core velocity for both inclinations, even though the velocity of the air in the duct is higher for the 30° angle.

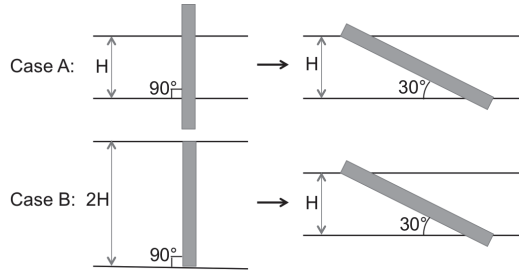


Figure 2.7: Definition of test set-up for inclined heat exchangers relative to the airflow.

#### 2.4.1 Preceding work based on experiments

Already by the 1940's, investigations were carried out where the airflow was angled relative to the heat exchanger. Nichols at NACA [39] performed this work, which included pressure drop and airflow uniformity analysis for angled heat exchangers relative to the airflow. The study was based on scenario *B*, where the thickness of the intercooler was  $240\text{mm}$ . The results showed that the flow losses increased only slightly for angles between  $30^\circ$ - $80^\circ$  compared to the perpendicular case; where the tests were carried out at  $10^\circ$  intervals from  $10^\circ$  to  $90^\circ$ . The velocity of the air at the heat exchanger face, was constant for all angles. For inclinations larger than  $30^\circ$  the pressure loss increased dramatically towards infinity. The heat exchanger was evaluated both when the tanks were at the top/bottom, and at the sides of the core. For all inclination angles the configuration with the tanks at the sides, later referred to as crossflow configurations, resulted in a lower pressure drop compared to when the tanks were at the top/bottom of the core. The explanation of this result was that the flow could enter the core more gradually. For a face velocity of  $5\text{m/s}$  the pressure loss, for an inclination of  $30^\circ$ , was increased by approximately 6% compared to the perpendicular case for the downflow orientation. For the crossflow orientation the corresponding value was 3%. A wool-tuft visualisation study was carried out to investigate airflow uniformity over the core. Up to an angle of  $30^\circ$  the airflow distribution at the face of the heat exchanger was fairly uniform. For more inclined heat exchangers the airflow was irregular, explained by the extreme abruptness between the duct and the heat exchanger.

Another experiment, evaluating pressure losses over a heat exchanger core inclined relative to the airflow, was conducted by Kim et al. [40]. A multi-louvered fin and flat tube heat exchanger with a thickness of  $20\text{mm}$  was investigated with the method as scenario *B*. Four angles were tested;  $90^\circ$ ,  $\pm 60^\circ$ ,  $\pm 45^\circ$  and  $\pm 30^\circ$ , where the airflow entered from both below and above. Five face velocities were tested within an interval of  $0.6$ - $2.1\text{m/s}$ . The tests were conducted both with and without an upstream duct. All arrangements had a downstream duct, mounted on three sides of the core, whose length varied between the inclinations to end at the most downstream part of the heat exchanger. The results from that study showed that neither the upstream duct or the inclination angle affected

the heat transfer rates significantly. For an increased inclination angle of the heat exchanger the pressure drop was increased consistently, where the pressure drop due to the entrance duct was up to 14%. No thoughts were expressed regarding pressure losses occurring at the exit duct. Though, it could be seen that the downstream duct disturbed the outlet airflow, increasing pressure losses for more inclined angles. They also suggested that the airflow direction at the exit of the core was dependent on the inlet direction.

Another experiment, which investigated heat transfer and pressure loss effects when angling a heat exchanger is Rivers et al. [41]. This study was conducted for a Grand Prix racing car, where the experiments were defined for a provided in- and outlet duct size, as in scenario A. Five angles were tested: 90°, 75°, 57.5°, 45° and 35°. The conclusion from this work was that the pressure drop was decreased for the angles 35° and 45°. For angles less inclined (57.5° and 75°) the pressure drop was increased compared to the 90°; with an explanation of induced stall on the radiator fin. From the illustrations it can be seen that separated areas were created behind the core, in the outlet duct, which most likely influenced the results. It was also observed that the heat transfer rate followed the same behaviour with a lower value for angles of 57.5° and 75°, and higher values for angles of 35° and 45°. Although it should be noted that the core area was doubled for the 30° angle and that the hot fluid was not continuously flowing through the heat exchanger. This results in a transient evolution: which is difficult to apply to real cases. The heat transfer rates were calculated from the velocity at the core, measured from experiments and heat exchanger properties from the manufacturer. From flow visualisation it was observed that the flow over the core was non-uniform, as a result of uneven flow across the entrance duct. The flow downstream became more uneven for a more inclined heat exchanger. The effect of installing turning vanes both in front of, and behind, the core was evaluated. Examples of stall at the forward facing vanes and separation at the rear vanes were seen, showing the difficulties of implementing these devices.

Monheit and Freim [42] showed by experiments that the thermal performance was not affected by the inclination angle. They also reported that the pressure drop increased for angles larger than 40° and that the effect was greater at lower Reynolds numbers.

Alternative positions of heat exchangers have been investigated for different types of vehicles, where the incoming airflow was not perpendicular to the heat exchanger core. For these studies the effect of angling airflow relative to the heat exchanger has not been evaluated. For passenger vehicles an investigation was carried out regarding positioning the heat exchanger towards the rear of the vehicle [43]. Another study used the hood/bonnet of a passenger car as a heat exchanger to reduce the size of the radiator in the engine bay [44]. The study also involved placing the heat exchanger at the underbody of the vehicle, which was also investigated by [45]. For heavy vehicles investigations regarding placing the heat exchanger on the roof of the cab compartment as well as at the very back of the vehicle have been performed by [46] and [47].

### 2.4.2 Preceding work based on simulations

There have been a number of investigations based on simulations of single fin and tube arrangements, with variances in simulation set-ups. Chang et al. [18] carried out a CFD study including fluid flow and thermal effects on a period of a louvered fin, for two different designs. The thickness of the core was  $36\text{mm}$  and one period of a fin with half tube thickness at each side was defined as the calculation domain. The regions up- and downstream were extended by 3 to 5 hydraulic diameters for both the air and water domain. For the simulations the symmetry boundary condition was applied. A grid sensitivity study resulted in a volume mesh consisting of  $6 \cdot 10^6$  cells, predominantly hexahedral cells with polyhedral cells at the surface. Nearest the surface two prism layers were selected. Steady state condition was used with the turbulence modelled by the realizable two-layer  $k - \varepsilon$  model, with the ideal gas condition. For the liquid a constant density was assumed with the same turbulence model as for the airflow. The solid parts were defined as having constant material properties, such as density and thermal conductivity. The simulated heat rejection was compared to experimental data, with a difference of 20%.

Karbach [48] also carried out an early study for a single period of a fin and tube. Both heat transfer and pressure drop were evaluated. The computational domain consisted of  $6 \cdot 10^5$  fluid cells and  $1.5 \cdot 10^5$  solid cells. No prismatic layers were defined for these simulations. The boundary conditions were defined as symmetric at the entrance and exit ducts and cyclic at the core. Calculations were defined for laminar conditions, where the simulated Reynolds numbers were between 200-2000. Correlation with experimental results showed an difference of 2-10% for the two methods.

Tafti et al. [10, 49] investigated geometrical effects on flow transition in multi-louvered fins, by using experiments and simulations. They showed that instability appeared in the wake of the exit louver, which spread upstream. Bouzida and Mignot [50] carried out another study regarding optimization of louvered fin design, with results for different internal designs and number of fins, and their design.

Yuan et al. [27] performed both experiments and CFD simulations to study flow fields and heat transfer rates for a louvered, corrugated airway design. An agreement of 10% was obtained between the two methods; for pressure drop and heat transfer rate. Even though the pressure drops and heat transfer rates for all operating conditions were consistently over-predicted by the CFD simulations compared to the test data, the simulations captured the correct trends as the experiments. The computational domain consisted of one period of a fin with an in- and outlet duct length of eight effective hydraulic diameters.

One of the first attempts to simulate two-dimensional louvered airways was performed by Achaichia and Cowell [51]. They simulated a fully developed laminar flow and evaluated pressure drop characteristics and heat transfer rates, based on airway configuration. They showed that the airflow was louver-directed for higher, and fin-directed for lower, Reynolds numbers.

Moreover, Junjanna et al. [52] carried out a study of the temperature distribution within a louvered finned heat exchanger, as well as analysing the airflow behaviour. Geometrical parameters were varied and the effects were evaluated to increase the compact heat exchanger efficiency.

As can be seen, angled heat exchangers relative to the approaching airflow have been experimentally studied in a number of studies. But, for these experiments the effects of varying thickness of the heat exchanger as a function of heat transfer rate and pressure drop have not been evaluated. It has been seen that the design of the experiments is of great importance to avoid losses arising due to the set-up and not from the angled heat exchanger itself. There has been plenty of work performed for simulations for one single fin. As knowledge and technology progresses larger cases can be simulated resulting in more accurate solutions. For these types of simulations no work considering airflow characteristics, pressure drop, or thermal effects of angling the airflow relative to the heat exchanger have been found. Neither has a study including all three methods: experiments; CFD simulations of the experimental set-up; and CFD simulations of one period of a fin, been performed for evaluating the angled phenomena of the airflow relative the heat exchanger core.



---

### 3 Method

In this project both experimental measurements and numerical simulations have been performed. This chapter will present the set-up of the experiments and the simulations, as well as the heat exchanger specifications. 3D CFD simulations have been performed to find a method of simulating angled heat exchangers, where both simulations of the experimental set-up, as well as one period of a fin of a heat exchanger, were performed. Different information is obtained from the different methods and by combining them increased insight of the problem can be achieved.

#### 3.1 Heat exchanger specification

This study was carried out using three compact, crossflow, heat exchanger designs. Two of them had traditionally louvered fins, which were angled symmetrically at the mid-point, while the third had the louvers angled in only one direction. The later was specially made and is not on the market due to manufacturing issues. The symmetric louvered finned heat exchangers had thicknesses of 19mm and 52mm and the asymmetric 19mm. The projected frontal area was the same,  $0.79m^2$ ; with measurements of  $888mm \times 888mm$ . Each heat exchanger consisted of 88 columns of tubes and fins, between the tanks. Each fin column consisted of 247 periods of fins. Squared tanks were mounted at the entrance and exit of the tubes. The thinner heat exchanger had one tube in depth and the thicker had two. To clarify the internal design one period of a fin for each heat exchanger is shown in figure 3.1a. A centreline view is shown for the same heat exchangers in figure 3.1b.

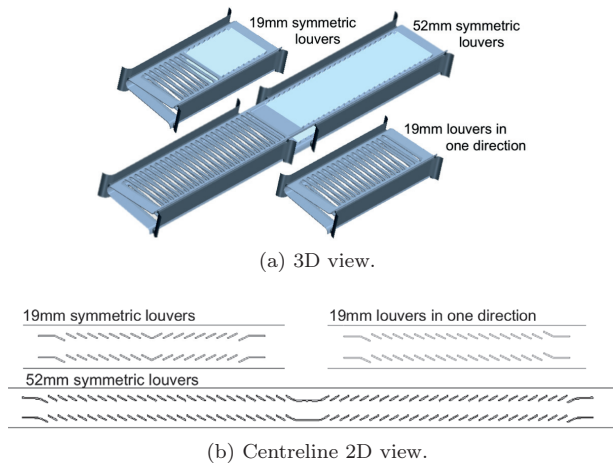


Figure 3.1: Internal design of the heat exchangers investigated.

A heat exchanger is defined by a number of geometrical properties, defined in figure 2.4. In Table 3.1 the values are defined for the parameters, for the heat exchangers used in this study. The values were the same for all three heat exchangers.

Table 3.1: Geometrical properties of the heat exchangers.

Parameter:	For all three geometries:
Displacement	$0.4mm$
Fin density	$1.8mm$ ( $14fins/inch$ )
Louver angle	$26^\circ$
Louver depth	$0.9mm$
Louver inlet	$1.4mm$
Tube pitch	$10mm$
Fin pitch	$1.8mm$

### 3.1.1 Definition of the experiments

From preceding work presented in Chapter 2.4 two main methods were described which could be applied when investigating angled heat exchangers. The duct height can be varied to fit the complete heat exchanger core within the duct for different angles, or the duct height can be constant, resulting in a larger core area for a more inclined heat exchanger. For road vehicles, a given volume is usually available for installing a heat exchanger, which was the argument for applying the second scenario, with a constant duct height. This scenario is defined as  $A$  in figure 2.7. For this scenario the air velocity in the core will decrease for a more inclined heat exchanger, when a constant mass airflow rate is defined, as a result of the increased core area within the duct.

All three heat exchangers were investigated at four angles:  $90^\circ$  which is when the airflow was perpendicular to the core,  $60^\circ$ ,  $30^\circ$  and  $10^\circ$ , relative to the vertical plane. Thus, the  $10^\circ$  arrangement had the most inclined heat exchanger relative to the airflow. A specific test was designed to carry out this investigation, with rectangular entrance and exit ducts, with the heat exchanger mounted in-between.

It was originally planned to run the experiments and simulations with an inlet and outlet duct. However, it was found, and will be shown later, that the outlet duct introduced a severe flow blockage and adverse pressure gradients for the experiments with angled heat exchangers. The increased pressure loss as a consequence of the outlet duct was also seen in preceding work. This explains why the outlet duct was removed for the angled arrangements in figure 3.2. To limit airflow separation at the transition from the inlet chamber to the duct, a bell-mouth was mounted at its entrance, designed with a constant radius. This device decreased the loss of total pressure between the inlet chamber and the entrance duct. In figure 3.2 a sketch on the centreline plane of the test set-up is shown for the  $90^\circ$  configuration, with the angled configurations presented below.

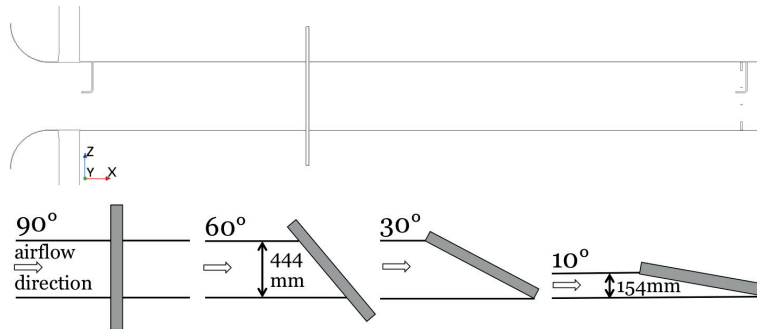


Figure 3.2: Definition of the experimental set-up for the angled heat exchangers.

A constant width of the squared duct was used for all inclinations at  $888\text{mm}$ . For the  $90^\circ$ ,  $60^\circ$  and  $30^\circ$  angles the duct had a height of  $444\text{mm}$ , and  $154\text{mm}$  for the  $10^\circ$  arrangement. The reason for the reduced duct height was the limitation in size of the heat exchanger. If the same height was going to be applied the heat exchanger should have been three times longer, compared to the ones that were used.

Two orientations of the heat exchangers were tested: first when the coolant tanks were at the top and bottom of the core, resulting in a vertical flow of the liquid; for the other set-up the heat exchanger was rotated  $90^\circ$ , resulting in a horizontal flow of the liquid, the tanks then being at the sides. The first scenario was defined as downflow tests and the second scenario as crossflow tests, see figure 3.3. The rectangle defines the area subjected to the incoming airflow for the  $90^\circ$  arrangements. The heat exchangers were thereafter angled downwards, toward the horizontal plane. For an inclination of  $60^\circ$  a larger part of the core was within the duct; and the complete core area was exposed to the incoming airflow for the  $30^\circ$  and the  $10^\circ$  arrangements. It should be pointed out that the heat exchanger with the louvers in only one direction was only tested for the downflow orientation.

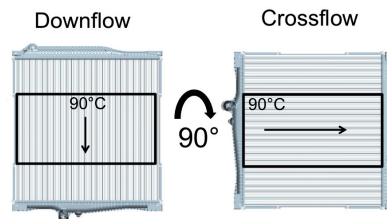


Figure 3.3: Definition of downflow and crossflow orientated heat exchanger.

The experiments were performed in both thermal and isothermal conditions. The reason for the isothermal experiments was to derive the porosity constants, which were used to define the pressure drop properties of the heat exchanger core in CFD. Another reason was to correlate CFD simulations with the experiments

without the influence of thermal effects. By adding heat into the simulations there will be increased complexity for the initial step of the correlation. For the isothermal conditions the air and liquid temperatures were defined to be 25°C in a combination of five mass airflow and no liquid flow rates. The air velocities were defined to be constant in the duct independent of inclination angle. Since the duct height for the 10° angle was 154mm compared to 444mm, used for the other angles, the inlet mass airflow rates were re-calculated to generate the same airspeeds at the inlet duct.

Information from Volvo GTT was that the velocity of the airflow at the cooling package for a truck, driving at 90km/h was approximately 2.5m/s. When the fan is fully engaged, the speed was increased to almost 9m/s. The mass airflow rates defined for the test procedure were based on this information, and the airspeed at the inlet duct was within a range of 1.9 – 9.8m/s. Five mass airflow rates were tested within this range, presented in figure 3.4.

For the thermal experiments the air temperature was the same as for the isothermal tests and the liquid was 90°C. A combination of the five mass airflow rates and five liquid flow rates were tested. The liquid was defined as water, and since the thickness of the heat exchangers varied, the liquid flow rates were re-calculated to have the same velocities. A combination of these parameters resulted in a relatively large test matrix, shown in figure 3.4. As can be seen, 60 tests per heat exchanger and angle were carried out, resulting in a final test matrix of 300 combinations. The mass airflow and liquid flow rates are also defined for each configuration in the matrix.

RAD width [mm]	Direction of Flow	Angle [°]	Height of Duct [mm]	Thermal tests			Isothermal tests		
				Inlet temp (liquid) [°C]	Flow rate (liquid) [kg/s]	Flow rate (air) [kg/s] (25°C)	Inlet temp (liquid) [°C] **	Flow rate (liquid) [kg/s]	Flow rate (air) [kg/s] (25°C)
19***	Cross flow	90	444	90	0.7, 1.2, 1.6, 2.1, 2.5	0.9, 1.8, 2.7, 3.6, 4.6	-25	0	0.9, 1.8, 2.7, 3.6, 4.6
	Cross flow	60							
	Cross flow	30							
	Cross flow	10	154			0.3, 0.6, 0.95, 1.3, 1.6			0.3, 0.6, 0.95, 1.3, 1.6
19°	Down flow	90	444	90	0.7, 1.2, 1.6, 2.1, 2.5	0.9, 1.8, 2.7, 3.6, 4.6	-25	0	0.9, 1.8, 2.7, 3.6, 4.6
	Down flow	60							
	Down flow	30							
	Down flow	10	154			0.3, 0.6, 0.95, 1.3, 1.6			0.3, 0.6, 0.95, 1.3, 1.6
52	Cross flow	90	444	90	2, 3.4, 4.8, 6.1, 7.5	0.9, 1.8, 2.7, 3.6, 4.6	-25	0	0.9, 1.8, 2.7, 3.6, 4.6
	Cross flow	60							
	Cross flow	30							
	Cross flow	10	154			0.3, 0.6, 0.95, 1.3, 1.6			0.3, 0.6, 0.95, 1.3, 1.6
52	Down flow	90	444	90	2, 3.4, 4.8, 6.1, 7.5	0.9, 1.8, 2.7, 3.6, 4.6	-25	0	0.9, 1.8, 2.7, 3.6, 4.6
	Down flow	60							
	Down flow	30							
	Down flow	10	154			0.3, 0.6, 0.95, 1.3, 1.6			0.3, 0.6, 0.95, 1.3, 1.6
19***	Down flow	90	444	90	0.7, 1.2, 1.6 2.1 2.5	0.9, 1.8, 2.7, 3.6, 4.6	-25	0	0.9, 1.8, 2.7, 3.6, 4.6
	Down flow	60							
	Down flow	30							
	Down flow	10	154			0.3, 0.6, 0.95, 1.3, 1.6			0.3, 0.6, 0.95, 1.3, 1.6

\*) Louvers in one direction  
 \*\*) No liquid flow through RAD  
 \*\*\*) Symmetric louvered fin with microprobes

Figure 3.4: Test matrix for angled heat exchangers.

For all experiments, the ducts, tanks, and the parts of the heat exchanger core outside the duct, were covered with insulation to prevent heat loss as well as air leakage.

## 3.2 Experimental measurements

Experiments were conducted on two test rigs: the fan test rig on Volvo GTT was used to calibrate microprobes, mounted within the core of one heat exchanger; and the climate wind tunnel at TitanX Engine Cooling AB was used for the angled arrangements of the heat exchangers.

### 3.2.1 Angled heat exchangers relative to the incoming airflow

The climate wind tunnel at TitanX was used to perform full size tests, where the heat exchangers were mounted at four angles relative to the incoming airflow. This is a semi-closed wind tunnel, where part of the airflow is guided outdoors to lower the airflow temperature, see figure 3.5. It is a plenum-to-plenum type wind tunnel with two nozzles, connected to electric motors, regulating the airflow. The large nozzle has an interval of  $0.8 - 10\text{kg/s}$  and the small  $0.1 - 0.9\text{kg/s}$ . The air can be heated or cooled between  $15 - 55^\circ\text{C}$  and the maximum temperature of the water circuit is  $90^\circ\text{C}$ . The inlet chamber is the pressure chamber and the outlet chamber is maintained at ambient pressure.

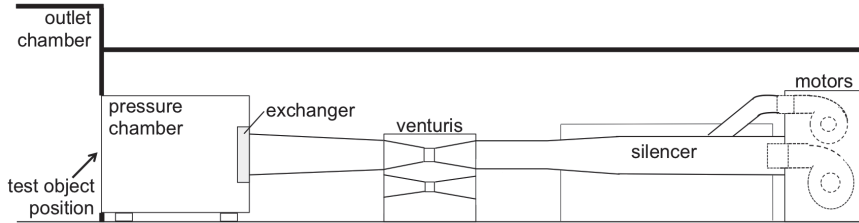


Figure 3.5: The plenum-to-plenum wind tunnel at TitanX.

A Computer Aided Design (CAD) picture of the experimental set-up is shown in figure 3.6. The inlet was located in the left chamber, the pressure chamber, and the outlet in the right chamber. Both the inlet and outlet ducts were mounted on wheels and there was a construction in the middle to rotate the heat exchanger around its central axis to change the angle relative to the airflow. The lengths of the ducts were defined by the hydraulic diameter,  $d_h$ , defined in equation 3.1, based on the area and perimeter of the entrance duct.

$$d_h = 4 \cdot \frac{A}{P} \quad (3.1)$$

The distance from the entrance of the bell-mouth until the heat exchanger was  $3d_{h,444}$ , and from the core until the end of the exit duct was  $5d_{h,444}$ , where the limitations of the lengths was the surrounding laboratory. The hydraulic diameter was here defined by the higher duct height,  $444mm$ . The distance from the bell-mouth to the centre of the core was constant for all inclinations. Therefore for an inclined heat exchanger the upper distance was shorter, and longer at the duct floor.

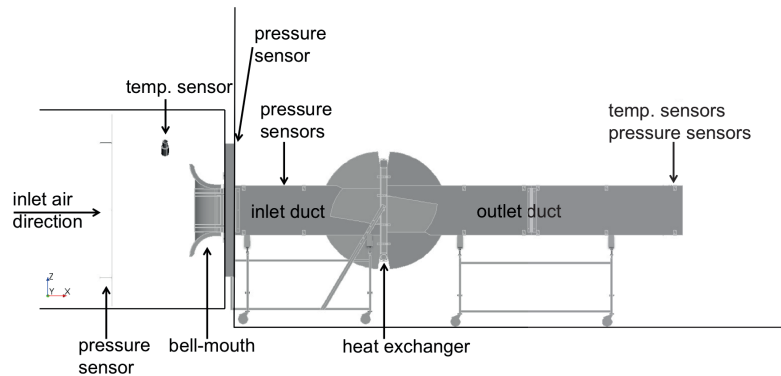


Figure 3.6: CAD picture of the experimental set-up.

To reduce losses at the entrance of the duct a bell-mouth was mounted to it, otherwise the flow-field would behave as in figure 3.7. A separated area at the 90° corner can be seen, where the airflow direction was from the right to the left. Studies have been performed regarding effects of the bell-mouth, for example [53]. Its radius and length are important design parameters to minimize losses. A study including three geometries was simulated in CFD to find the most appropriate for these experiments. The radius for the three geometries were: 104, 180 and 250mm. From the results it was evident that the bell-mouth with a radius of 250mm was the most suitable for preventing total pressure losses. To be able to mount and dismount the test set-up the bell-mouth had to be shortened at the sides, relative to the top and bottom of the duct, to a length of 105mm. The airflow was not ideal in these areas due to this design compromise.

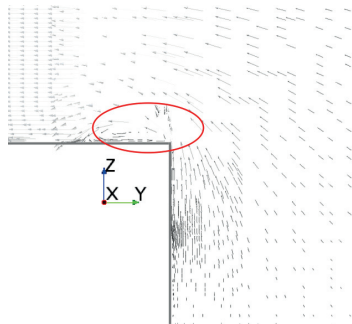
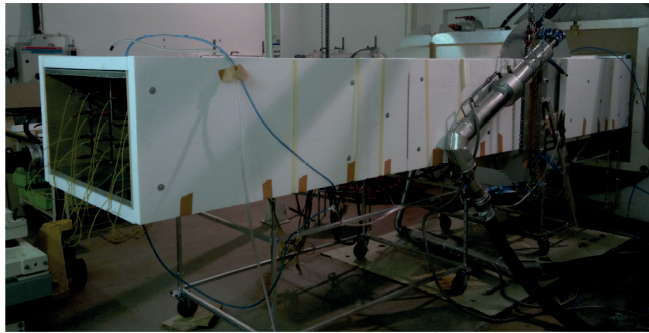
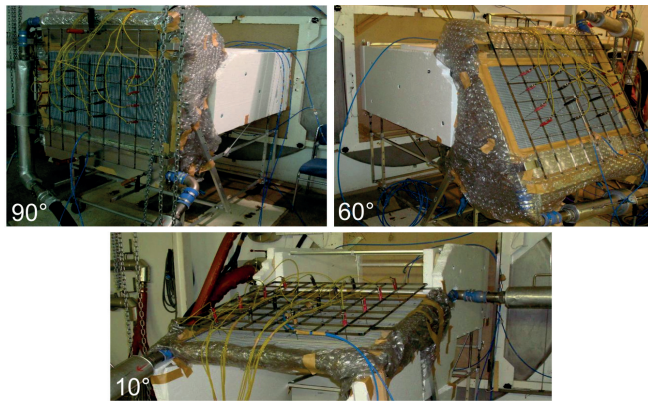


Figure 3.7: Velocity vectors at the entrance of the duct.

In figure 3.8 pictures of the experiments are shown. The top picture, figure 3.8a, shows the experiment carried out with the outlet duct, for the perpendicular arrangement. For the angled arrangements the outlet duct was removed, as can be seen in figure 3.8b.



(a) 90° installation, with the outlet duct present.



(b) Installations without the outlet duct.

Figure 3.8: Pictures of the experiments.

### Measurement specification

Sensors measuring temperature, static and total pressures were positioned along the installation. The temperature was measured at one location at the inlet chamber, and with a grid of 16 sensors at the exit of the outlet duct to cover the complete outlet area. The pressure drop over the rig, was measured from the inlet to the outlet chamber, where the reference position in the outlet chamber was mounted above the duct marked in figure 3.6. Additionally at both the inlet and outlet ducts, three sensors were positioned: one pitot-static tube, which measured total and static pressure, mounted at the centre of the duct; and two pressure taps at the duct roof and floor, measuring the static pressure. These devices were mounted at a distance of  $2.4d_{h,444}$  in front, and  $4.8d_{h,444}$  behind, the heat exchanger core. For the angled configurations the sensors

mounted in the roof and floor, positioned at the outlet duct, were moved to the reference position at the outlet chamber. Whereas the pitot-static tube and the temperature grid was mounted  $10d_{h,fin}$  behind the core, based on the fin. Differential values were recorded for the standard test procedure and absolute values for control measurements. Differential values in the inlet to the outlet duct were recorded for the different measuring positions. Hence, four differential pressure measurements were recorded for each test: the chamber pressure drop; the differential pressure between the pressure taps at the entrance and outlet ducts; the differential static pressure; and total pressure at the pitot-static tubes.

From the test results variations in static pressure drop were seen between the two methods of measuring the pressure loss between the inlet to the outlet duct. An evaluation was conducted to find the most accurate and stable way of measurement. It was found that the differential pressure between the inlet and outlet chambers was the most reliable method, since it was a rig-fixed installation with connecting metal pipes. Variations were seen for the two other methods, most likely due to: a non-ideal airflow, the shape of the hole, the plastic pipes, leakage, or the positions of the holes. From CFD simulations it can be seen that positioning the pressure tap in the roof, just in front of the pitot-static tube, increased the static pressure in this position. For the most inclined heat exchanger, larger variations were seen in static pressure drop measured at the different positions in the ducts. The differential static pressure values measured by the taps and the pitot-static tubes varied by up to  $26Pa$ , which corresponded to a 10% variation. For the lower mass airflow rates the recorded pressure drops were lower, which decreased the measurement accuracy. Due to this the decision was made to have the chamber pressure drop data as reference.

### Correction of measured data

Since the experiments were performed over a period of a year, environmental conditions varied. The measured values were corrected and normalized to standard air condition for density and dynamic viscosity at  $25^{\circ}C$ . The normalization was performed due to variations in inlet temperature and was carried out for the analysed pressure drop.

To correct the pressure drop to an inlet temperature of  $25^{\circ}C$ , density and dynamic viscosity had to be corrected. By applying the Darcy-Forchheimer theory, the inertial,  $k_i$ , and viscous,  $k_v$ , coefficients were derived for each measured pressure drop via linear regression, see equation 3.2.

$$\Delta p = k_v \mu V + k_i \rho V^2 \quad (3.2)$$

The density was calculated by the ideal gas law, defined in equation 2.8 and the dynamic viscosity was plotted as a function of absolute temperature by using the Sutherland law, presented in equation 3.3. Regression was applied to the curve to find coefficients to calculate the dynamic viscosity for the experiments.

$$\mu = \mu_0 \left( \frac{T}{T_0} \right)^{3/2} \left( \frac{T_0 + S}{T + S} \right) \quad (3.3)$$

When the  $k_i$  and  $k_v$  coefficients were derived the pressure drop was re-calculated for the density and viscosity properties to a temperature of 25°C, according to equation 3.4.

$$\Delta p_{25^\circ\text{C}} = k_v \mu_{25^\circ\text{C}} V + k_i \rho_{25^\circ\text{C}} V^2 \quad (3.4)$$

The heat transfer rate was calculated from the temperature difference of the liquid and the measured mass liquid flow rates within the liquid circuit. To ensure heat transfer balance the heat transfer on the liquid side should correspond to the heat transfer rate on the air-side of the heat exchanger. Since the flow rates and temperatures of the mediums varied between the tests, the  $\varepsilon - NTU$  method was applied to make corrections and to derive heat transfer parameters. This method was first developed by Kays and London [28] and is described in Appendix A.

### Detection of losses along the test installation

The airflow through the inlet chamber, bell-mouth, inlet duct, and the heat exchanger core up to the outlet chamber, was affected by the design of the test installation. To be able to validate the difference in static pressure drop of the different heat exchanger inclinations, the airflow effects along the experimental set-up were evaluated. From CFD simulations of the complete test set-up, losses along the installation of the heat exchanger were identified. The losses coefficients were divided into three regions:  $k_1$ ,  $k_2$ ,  $k_3$ , defined in figure 3.9.

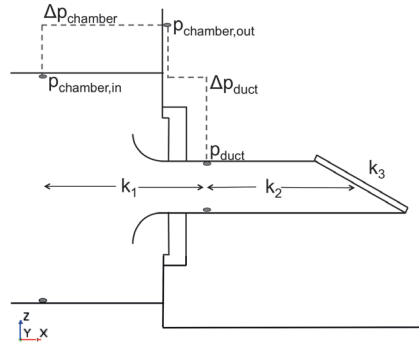


Figure 3.9: Definition of loss regions along the experimental set-up and pressure measurement locations.

To be able to explain the physics and to find the magnitude of each coefficient a set of total pressure balance equations, described by the Bernoulli theory in

equation 3.5, were defined. By assuming no acceleration due to gravity the second term was equal to zero. Since the installation was a closed system the total pressure in one location,  $A$ , was equal to the total pressure at another location,  $B$ , minus losses. The equation can therefore be defined as in equation 3.6. The evaluation was carried out for the isothermal condition, eliminating density variations and acceleration effects of the airflow due to heating. No leakage within the rig was assumed and mass airflow was considered as constant, meaning that the air velocity only changed with varying cross-sectional area. The boundary layer growth, which resulted in an accelerated airflow in the duct, was handled as a loss due to the definition. The conservation of mass equation is defined in 3.7.

$$\frac{v^2}{2} + gz + \frac{p}{\rho} = constant \quad (3.5)$$

$$p_B = p_A + \frac{\rho}{2} (v_A^2 - v_B^2) - losses \quad (3.6)$$

$$\dot{m} = \rho v A \quad (3.7)$$

Total pressure balance equations along the experimental set-up were set-up to determine the loss coefficients. The values of the coefficients may be dependent on the heat exchanger angle and its thickness, resulting in various values for the different set-ups. Therefore, it was important to evaluate them individually and later find dependencies between heat exchangers and their angles. The equations were defined for each loss region, with the notations of figure 3.9. The expression for each loss region is presented in equations 3.8-3.15. The pressure drop over the core was expressed as the difference in Surface Averaged ( $SA$ ) static pressure at the inlet and outlet to the core, see equation 3.10.

Starting at the entrance of the inlet chamber, a uniform flow entered the inlet chamber. Due to the relatively large area of the inlet, compared to the duct area, the dynamic pressure and air velocity were low. The first contraction of the airflow was at the bell-mouth. The airflow accelerated in to the duct, driven by static pressure. The losses in this region,  $k_1$ , may have occurred due to a non-ideal shape of the bell-mouth and due to boundary layer growth until the second measuring position, marked as  $p_{duct}$  in figure 3.9. The total pressure balance for the first loss region applied according to equation 3.8, where the left-hand side represents the total pressure within the inlet chamber and the right side the entrance duct, including the loss coefficient as a function of the dynamic pressure in the duct.

$$p_{chamber,in} + \frac{1}{2}\rho V_{chamber,in}^2 = p_{duct} + \frac{1}{2}\rho V_{duct}^2 + k_1 \frac{1}{2}\rho V_{duct}^2 \quad (3.8)$$

From this position until the front face of the core, losses occurred due to the pitot-static tube, creating a high-pressure region in front and a low-pressure region behind. The pitot-static tube had a diameter of  $10mm$  with a wall thickness of  $2mm$ . Within the second region there were also losses due to boundary

layer growth, which increased viscous losses and losses as a consequence of the angling of the heat exchanger. In equation 3.9 the pressure balance for the second loss region is defined.

$$p_{duct} + \frac{1}{2}\rho V_{duct}^2 = SA_{core,in} + \frac{1}{2}\rho V_{core,in}^2 + k_2 \frac{1}{2}\rho V_{duct}^2 \quad (3.9)$$

Through the heat exchanger core static pressure was lost. In the balance equations this loss was described as in equation 3.10.

$$\Delta p_{core} = SA_{core,in} - SA_{core,out} \quad (3.10)$$

The loss coefficient from the outlet of the heat exchanger until this reference position at the outlet chamber was noted as  $k_3$  and is defined in equation 3.11. At the reference position the velocity of the air at the outlet was zero, whereas the fourth term in equation 3.11 was equal to zero.

$$SA_{core,out} + \frac{1}{2}\rho V_{core,out}^2 = p_{chamber,out} + \frac{1}{2}\rho V_{chamber,out}^2 + k_3 \frac{1}{2}\rho V_{core,out}^2 \quad (3.11)$$

To separate the losses due to the entrance duct and the re-direction of the airflow in the core, the loss coefficient in the second region was further divided into two parts, see figure 3.10. The new loss coefficient in the duct was noted as  $k_4$  and the losses due to the angling effect were expressed as the difference in dynamic pressure in the duct and at the heat exchanger inlet. The loss term for the second region, defined in equation 3.9, was re-defined to equation 3.12, which was re-written as in 3.13.

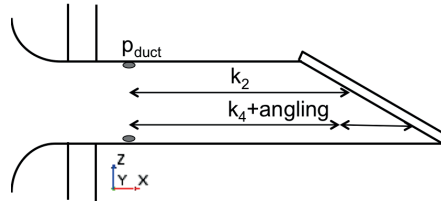


Figure 3.10: Definitions of the loss coefficients in the second region.

$$k_2 \frac{1}{2}\rho V_{duct}^2 = k_4 \frac{1}{2}\rho V_{duct}^2 + \frac{1}{2}\rho V_{duct}^2 - \frac{1}{2}\rho V_{core,in}^2 \quad (3.12)$$

$$k_2 \frac{1}{2}\rho V_{duct}^2 = k_4 \frac{1}{2}\rho V_{duct}^2 + \frac{1}{2}\rho V_{duct}^2 (1 - \sin^2 \alpha) \quad (3.13)$$

The final expression for the second loss region was then re-defined from equation 3.9 to 3.14.

$$p_{duct} + \frac{1}{2}\rho V_{duct}^2 = SA_{core,in} + \frac{1}{2}\rho V_{core,in}^2 + k_4 \frac{1}{2}\rho V_{duct}^2 + \frac{1}{2}\rho V_{duct}^2 (1 - \sin^2\alpha) \quad (3.14)$$

The  $k_4$  coefficient only represents losses in the duct as a result of boundary layer growth and separation behind the pitot-static tube, while the last two terms in equation 3.13 were the dynamic pressure variation as a consequence of the decrease in airflow speed in front of the heat exchanger and the re-direction of the airflow, for the angled arrangements. For the  $90^\circ$  heat exchanger this part was equal to zero. The main dynamic pressure loss over the installation occurred at the forced re-direction of the airflow and at the exit of the core. The third loss region was behind the heat exchanger until the reference position at the outlet of the rig. To find the static pressure drop only over the heat exchanger core the sum of all loss coefficients multiplied by the dynamic pressure in the duct was subtracted from the chamber pressure drop, see equation 3.15.

$$\Delta p_{core} = \Delta p_{chamber} - \left( k_1 + k_4 + (1 - \sin^2\alpha) + k_3 \sin^2\alpha - \left( \frac{A_{duct}}{A_{chamber,in}} \right) \right) \frac{1}{2}\rho V_{duct}^2 \quad (3.15)$$

### Measurement accuracy

To find the uncertainty of the heat transfer rates on the liquid and the air-side, as well as for the pressure drop the measurement accuracy was evaluated. The measurement accuracy in the climate wind tunnel at TitanX is presented below:

- Mass airflow rate in the large venturi:  $\pm 0.01 \text{ kg/s}$  with a range of  $1 - 9 \text{ kg/s}$
- Mass airflow rate in the small venturi:  $\pm 0.01 \text{ kg/s}$  with a range of  $0.2 - 0.8 \text{ kg/s}$
- Mass liquid rate:  $\pm 0.2\%$  of read value
- Barometric pressure:  $\pm 0.15\%$  of the range, resulting in a deviation of  $\pm 0.3 \text{ kPa}$
- Chamber pressure drop:  $\pm 0.065\%$  of the range, resulting in a deviation of  $\pm 1.0 \text{ Pa}$
- Temperature deviation in the venturi:  $\pm 0.2^\circ \text{C}$
- Temperature of the air at the inlet chamber:  $\pm 0.2^\circ \text{C}$
- Temperature in the grid placed behind the heat exchanger:  $\pm 1^\circ \text{C}$

- Temperature of the liquid:  $\pm 0.2^\circ\text{C}$

The uncertainty of the mass airflow rate was  $\pm 0.1 - 5\%$ , and  $\pm 3 - 8\%$  for the temperature, with a heated differential temperature of  $15^\circ\text{C}$  and  $40^\circ\text{C}$ . The final uncertainty for the heat transfer rate on the air-side was  $\pm 7 - 8\%$ .

For the liquid side the uncertainty of the mass liquid flow rate was  $\pm 0.2\%$ , and for the temperature  $\pm 4 - 20\%$ , for a cooled liquid differential temperature of  $2^\circ\text{C}$  and  $10^\circ\text{C}$ . The final uncertainty for the heat transfer rate on the liquid side was  $\pm 4.2 - 20.2\%$ .

### Inaccuracy factors

When performing experiments there are usually inaccuracy factors that can affect the test results. For the angled heat exchangers a repeatability study was not performed to find variations due to the mounting and dismounting of the ducts and the heat exchangers between the tests. Other factors affecting the results could be how and where the sensors were mounted and positioned.

#### 3.2.2 Calibration of Ruijsink microprobes

To be able to investigate the velocity distribution across the heat exchanger, microprobes were mounted inside the core for the  $19\text{mm}$  thick heat exchanger with symmetric louvers. This was a differential pressure system consisting of 48 pitot tube type probes. The system was developed by Ruijsink Dynamic Engineering [54]. The probes were mounted within the core, between two fins and two tubes. Two tubes were connected to each probe, measuring static and total pressure. The total pressure tap was positioned at the centre of the probe, within the shell and in-line with the airflow. The static pressure was taken from a hole, in the wall of the shell, where the airflow was perpendicular to the hole. Figure 3.11a shows the probe design and figure 3.11b shows it mounted in the radiator.

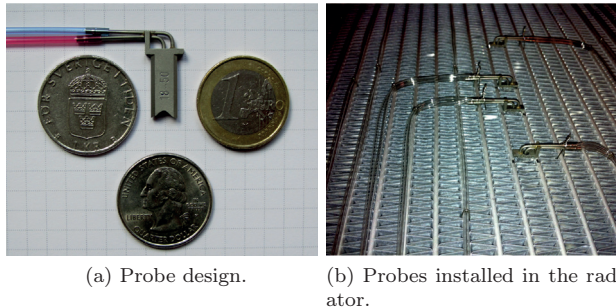
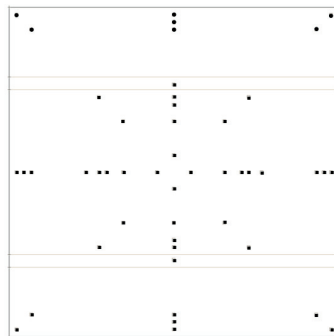


Figure 3.11: Ruijsink microprobes.

For this investigation the probes were mounted in a symmetric, but in a non-homogenous manner to increase the number of probes subjected to the airflow for the less inclined heat exchangers. In figure 3.12a the probe positions are shown.

The calibration of the probes was conducted in the Volvo GTT fan test rig, against a known air velocity. After the calibration the heat exchanger was tested in the angled arrangement in the TitanX wind tunnel, where the local velocity in the heat exchanger was recorded. To record the measured values the output side of the tubes were connected to a double scanivalve system and a differential pressure transducer. A control box and a control system were developed by the manufacturer to be able to control the system from a computer. A plot of the voltage signal and local velocity was obtained by monitoring the voltage signals in the probe as a function of different flow rates in the test rig. To determine the local velocity in each probe the differential pressure over the total and static taps were recorded and compared to the averaged air velocity through the core, obtained by the known volumetric flow rates and core size. To limit entrance effects a bell-mouth was mounted at the entrance to the core, seen in figure 3.12b. To improve accuracy it was recommended to use the system in isothermal conditions.



(a) Probe distribution within the core.



(b) Heat exchanger mounted in the Volvo fan test rig.

Figure 3.12: Probe positions in the heat exchanger.

The fan test rig at Volvo GTT is a plenum-to-plenum closed-loop type rig, where the outlet chamber is maintained at ambient pressure and the inlet chamber is the pressure chamber. Figure 3.13 shows a detailed plan view of the rig. Six venturi-type nozzles are used to measure air mass flow through the rig, which is driven by an electric motor into the pressure chamber. The test object is placed between the pressure and the outlet chamber, which in this case was the Ruijsink microprobes-equipped heat exchanger. The airflow in the outlet chamber is guided back to the nozzles, through a set of heat exchangers to regulate the temperature to a constant value at the pressure chamber.

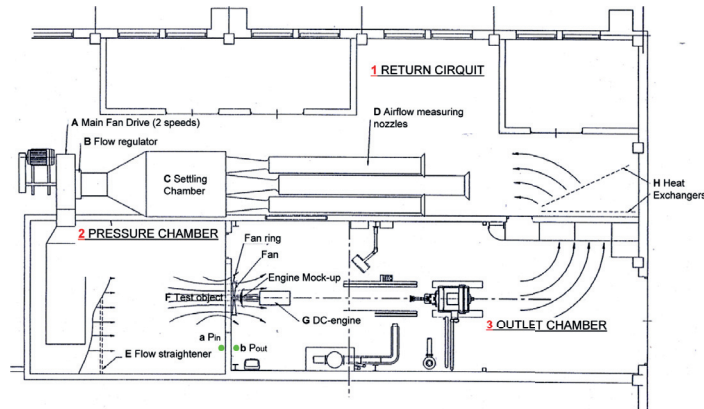


Figure 3.13: Plan view of the Volvo fan test rig.

### 3.3 Numerical simulations

CFD is a numerical approach, commonly based on the Finite Volume Method (FVM) to solve the Navier Stokes equations, defined in Chapter 2.3. In this chapter the CFD procedure and set-up of the models are presented.

The CFD procedure includes a number of steps: pre-processing, solving, and post-processing. Part of the pre-processor step is CAD cleaning, surface meshing and volume meshing. Before the surface can be meshed the geometry has to be improved to obtain a fine grid. In this study the software ANSA from BetaCAE Systems was used for assembling the CAD parts, and to make geometrical changes as well as making a surface mesh. To capture geometry details in important areas the cell size must be considered. The next step is to define a calculation domain where defined models and equations will be solved, further described in this chapter. Thereafter the model was exported to the software StarCCM+, produced by CD-adapco, using versions 8 and 9. In this software the model can be wrapped, re-meshed and volume meshed. Higher resolution areas are thereafter defined, where a higher resolution of the volume mesh will result in a more resolved solution, but at the cost of computational time. A volume mesh corresponds to when the calculation domain is discretized with small volume elements. The sizes of the volume cells are dependent on the expected flow behaviour and its proximity to the solid surface. The final step, after all parameters and models are defined, is the solving procedure. This step was also performed in StarCCM+, and is an iterative procedure, where the conservation equations defined in Chapter 2.3 are solved. After convergence the results were posted in StarCCM+. Included in this step is analysis of the results by looking into different parameter plots. Local values of the various parameters are obtained making it possible to further evaluate experimental results.

### 3.3.1 Simulations of the experimental set-up

To reduce calculation time the original CAD models were simplified compared to the layout of the experimental set-up seen in figure 3.6. The CAD cleaned data used for the simulations, is presented in figure 3.14 for the 30° arrangement.

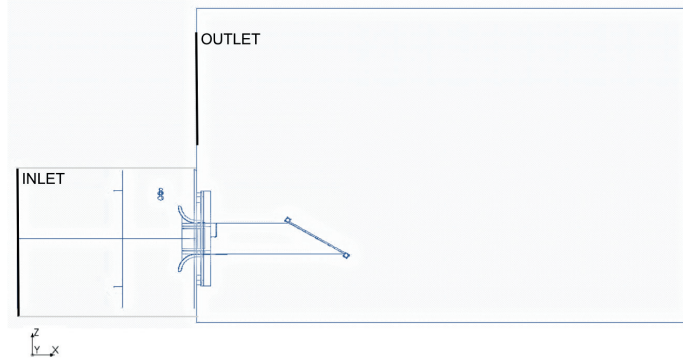


Figure 3.14: The computational domain for the cleaned CAD data of the test set-up.

For these simulations two of the tested inlet-air velocities were defined for each heat exchanger and inclination angle:  $1.25m/s$  and  $0.49m/s$ . Due to the reduced duct height for the 10° angled arrangements the velocities were  $0.43m/s$  and  $0.16m/s$ . These velocities corresponded to a mass airflow rate of  $4.6kg/s$  and  $1.8kg/s$  for the 90°, 60° and 30° inclinations and  $1.6kg/s$  and  $0.6kg/s$  for the 10° inclination.

### Boundary conditions and model definitions

The computational domain was set by the CAD layout of the test rig. In figure 3.14 the circular inlet at the pressure chamber is shown, defined as *velocityinlet* and the outlet of the wind tunnel was defined as *pressure outlet*, set to atmospheric pressure. The heat exchanger was defined as a porous media, further described in chapter 3.3.1.

The main settings in the CFD solver were as follows. This study used the 3D incompressible RANS equations where the turbulence was modelled using the Realizable  $k - \varepsilon$  two layer model, with the segregated solver together with a second order discretisation scheme. The density of the air was defined as constant, with a density of  $1.18kg/m^3$ . Within this boundary layer, the two-layer all  $y^+$  wall treatment model was applied to model the flow, which was recommended by [37]. This model uses either the low or the high  $y^+$  wall treatment depending on the corresponding  $y^+$  value. As  $y^+ \rightarrow 0$  this model provides results similar to the low- $y^+$  treatment, and as  $y^+ > 30$  as high- $y^+$  treatment.

### Grid definition

In order to achieve an accurate and stable solution the mesh resolution must be well specified. Refinement zones were defined around and behind the heat exchanger core, within the ducts, and at the bell-mouth inlet. The cell size was set to  $4mm$  within the core and  $16mm$  within the other refinement areas. For the volume mesh the trimmer function was applied, generating predominately hexahedral cells with polyhedral cells nearest the surface. The resulting volume meshes varied slightly and were in the order of  $40 \times 10^6$  cells. Figure 3.15 shows a section of the essential parts for this test set-up, with a cell density distribution locally around the test object. Prismatic layers were grown at the surface, where attached airflow was assumed, to resolve the viscous sub-layer. The final mesh resulted in an  $y^+$  value below one. 14 layers with a growth rate of 1.5 were defined.

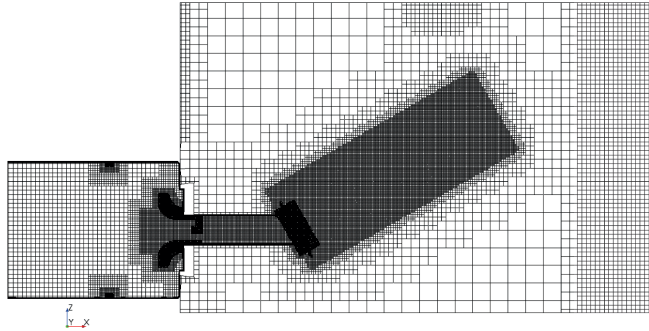


Figure 3.15: Volume mesh at the centreline of the experimental set-up.

### Definition of porosity coefficients

The porosity constants, which defined the properties of the heat exchangers, were calibrated from the  $90^\circ$  arrangements. These constants were used for the  $90^\circ$  simulations, as well as for the other angles. To obtain perfect correlation between experiments and simulations the porosity coefficients should be derived for each heat exchanger and angle. Usually a component test for a heat exchanger is only performed at  $90^\circ$  and to obtain the constants for the inclined heat exchanger, the specific angles must be tested. This would be an expensive and time-consuming procedure. The porosity constants were therefore evaluated for being defined by the constants derived for the  $90^\circ$  configurations to find similarities and deviations.

To find the correct porosity constants simulations were performed in two steps. The initial simulation was based on the porosity constants derived from experiments, for the  $90^\circ$  with an outlet duct, by using equation 2.19. The pressure drop was based on the differential pressure measured at the roof and the floor, at the inlet and outlet duct. Figure 3.16 shows the measuring positions,  $p_{duct}$  and  $p_{duct,out}$ . But, this pressure drop also included some losses in the ducts. After

evaluating the CFD results from the first simulation, pressure losses between the sensor positions and the heat exchanger core were identified, marked as  $X_{in}$  and  $X_{out}$  in the figure. These pressure losses were subtracted from the pressure drop defined at the first stage, since they should not be included in the pressure drop from where the porosity constants were derived. Otherwise, the pressure drop through the radiator would be simulated as a higher resistance relative to reality. The pressure losses in the duct were derived for two inlet velocities and subtracted from the simulated results. Thereafter the pressure drop versus the velocity in the duct was plotted, and to find the relation a regression curve was derived, to obtain the values of the  $P_i$  and  $P_v$  parameters for the losses at the inlet and exit ducts. These values were subtracted from the porosity constants, derived in the first step. New porosity constants were then calculated, and these values were only due to the pressure drop over the heat exchanger itself and did not include losses in the ducts. New simulations for the  $90^\circ$  orientation were performed and these porosity constants were also used for the other inclinations.

The derived coefficients were defined in the longitudinal direction of the core. In the two other directions these coefficients were multiplied by a factor to prevent the air from flowing in the other two directions within the heat exchanger. An influence study of these factors was carried out for different magnitudes to evaluate the impact of the flow. This study is presented in Appendix B. Results from this study showed that the factors should be defined as  $100 \times$  *pressure drop in X*, in the y- and z-direction.

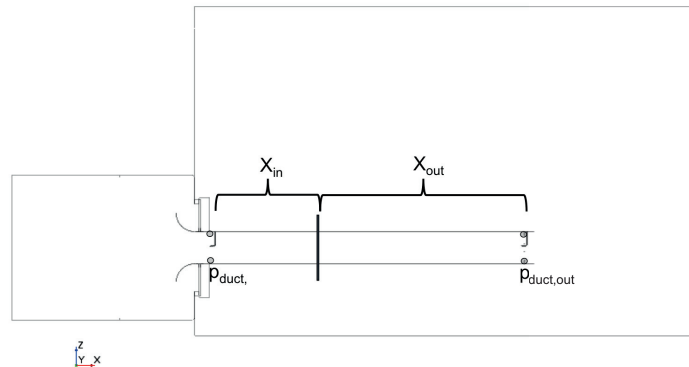


Figure 3.16: Definition for deriving porosity factors for the  $90^\circ$  orientation with an outlet duct.

### 3.3.2 Simulations of one period of a fin

To be able to understand the physical characteristics within the core of the heat exchanger, when the airflow was angled relative to it, simulations were carried out for one period of a fin. For these simulations no effects from duct or edges were included, resulting in pressure drop only due to the core as a function of the re-direction of the airflow. Simulations were performed for both one and two periods of a louvered fin for the  $19\text{mm}$  thick heat exchanger. From the results

it was seen that the airflow characteristics were almost identical, which was also the case for the pressure drop. The pressure drop varied by a maximum of  $0.5Pa$  between the two definitions of the computational domains. Subsequently, the computational domain was defined by one period of a fin with half tubes at each side, seen in figure 3.17. A centreline section is shown, which was later used for post-processing. The size of the computational domain was initially defined to be  $5h_{d,fin}$  in front of the core and  $20h_{d,fin}$  behind it until the outlet. From simulations it was observed that the wake had not fully dissipated. The domain was therefore extended to  $40h_{d,fin}$ , which resulted in an even airflow at the outlet boundary. The same computational domain was used for all inclinations, with varying values of the velocity components in the x- and z-direction to simulate the angling effect. Previous research has shown shorter computational domains behind the fin, for example [27, 18].

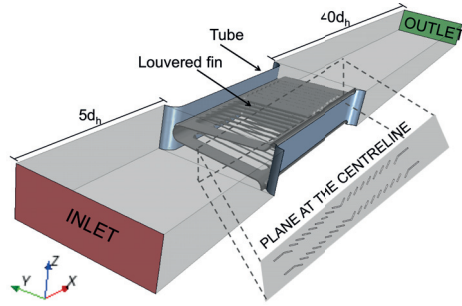


Figure 3.17: The final computational domain for simulations of one period of a louvered fin.

Both isothermal and thermal simulations were carried out for one period of a fin. For the isothermal simulations two types of velocity set-ups were defined. For the first scenario the velocity at the inlet was set to be the same as the velocity within the duct for the experiments: to be able to catch the phenomena that was tested. Two velocities were simulated based on this method, corresponding to the same as mass airflow rates as for the simulations of the experimental set-up. The velocities in the duct were  $3.87m/s$  and  $9.83m/s$ . To obtain the correct velocity the vector was divided into an x- and z-component, to correspond to the correct inclination angle of the airflow. For example, for the  $\pm 30^\circ$  angled cases: the x-component was  $+4.92m/s$  and the z-component was  $\pm 8.52m/s$  for the higher air velocity; and  $+1.94m/s$  and  $\pm 3.35m/s$  for the lower velocity. The other scenario was to simulate a fixed velocity in the x-direction of the core, defined in figure 3.17, where the z-component varied to obtain the correct inclination angle. This method applied a constant velocity of the air in the x-direction through the core, independent of the inclination angle.

Two geometries of the  $19mm$  and the  $52mm$  heat exchanger, with symmetric louvered fins, were simulated: one with sharp edges; and the other, which was modified to be smoother. The modified geometry was generated from visualisations and measures from a section of the heat exchanger used for the experiments. This was carried out for both heat exchangers with symmetric

louvered fins to determine the sensitivity of geometry variations. Figure 3.18 shows the differences for the geometries of both heat exchangers. The shape of the louvers was also smoother for the modified fin as well as the welding between the fin and the tubes. Areas with larger variations are highlighted with circles.

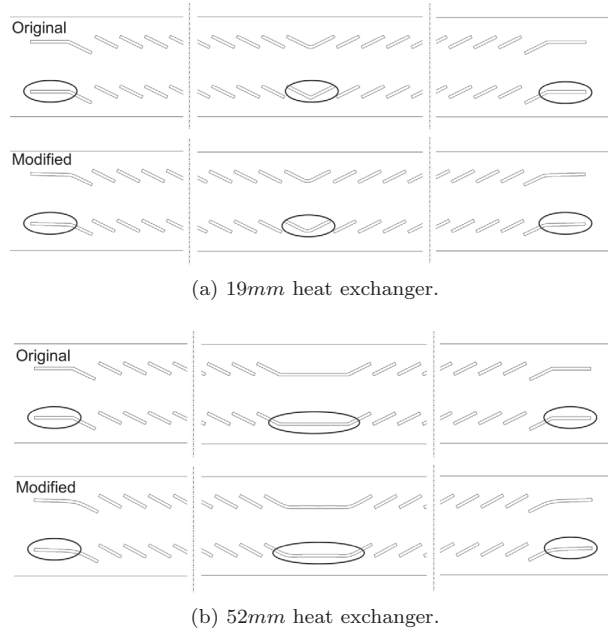


Figure 3.18: The louvered fin, with the original and the modified design.

### Boundary conditions and model definitions

The inlet boundary condition was defined as *velocity inlet* and the outlet of the domain was defined as *pressure outlet*, set to atmospheric pressure. All other duct walls were defined as periodic, assuming an infinite heat exchanger core. The periodicity boundary condition was only valid for the central part of the core and not near its edge, where the flow phenomena behaved differently. For the thermal simulations the louvered fin and tubes were defined as solids. These boundary conditions have been commonly applied in previous research as well.

The Reynolds number is dependent on the defined velocity and the characteristic length of what is simulated. The equation for the Reynolds number is defined in equation 3.16, where the characteristic length,  $L$ , has been defined in two ways in preceding work. When applying the hydraulic diameter of the fin as the characteristic length,  $d_{h,fin} = 2.7mm$ , the number for the two first simulated velocities were 1740 and 685. When applying the louver depth as the characteristic length,  $L = 0.9mm$ , the Reynolds numbers were even lower; 580 and 230.

$$Re = \frac{\rho V L}{\mu} \quad (3.16)$$

Experimental observations for flow in a pipe have been carried out, for example [55], with conclusions that for a fully developed airflow the flow was laminar for  $Re < 2100$  and turbulent for  $Re > 4000$ , based on the pipe diameter. In between these numbers both laminar and turbulent flow behaviour can take place, so called transition flows, which is dependent on surface roughness and other shape parameters. It is important to remember that a transition from laminar to turbulent flow can take place at different Reynolds numbers, depending on the investigated geometry. Due to the complex airflow, with louvers cutting boundary layers and angling the airflow, turbulence could be present even though  $Re < 2300$ . It has been seen in proceeding work that the airflow was commonly defined as laminar for simulations of a single fin and tube arrangement, as a result of relatively low Reynolds numbers. But, it has been shown that a turbulent airflow was created for some of the configurations. Since the resulting pressure drop difference was small for the different set-ups, the airflow was defined as turbulent. An investigation was performed to find a simulation method for this type of problems, where various fluid-flow models were examined, described in Paper I. The results showed that the simulations could be sufficiently defined as steady state with the fluid modelled with the RANS equations, where the turbulence was modelled by the *SST*  $k - \omega$  model. Since the same set-up was defined for the thermal simulations the ideal gas law was applied as well as the 2nd order segregated solver for the fluid temperature model, which solves the energy equation. To model the flow near the wall, the  $y+$  wall treatment model was applied. This is a hybrid approach to find the most appropriate model to simulate the correct airflow behaviour in the boundary layer. Studies carried out for similar geometries with a perpendicular airflow relative the heat exchanger were based on the Realizable two-layer  $k - \varepsilon$  turbulence model [18, 50]; while others have defined the fluid flow as laminar [50, 27]. For the thermal simulations the temperature at the tube walls was set to  $90^\circ\text{C}$ , which was the entry temperature of the liquid in the experiments. Conduction and convection models were applied for calculating the heat transfer.

### Grid definition

A mesh dependency study was carried out for the  $19\text{mm}$  thick heat exchanger. Eight mesh generation configurations were evaluated, defined with a cell base size between  $0.025 - 0.100\text{mm}$ . The mesh was defined by the surface cell size, cell size in the refinement box at the core, number of prismatic layers, and the growth rate of the mesh. The number of prismatic layers was nine for most of the configurations, with a total height of  $0.08\text{mm}$ . In Table 3.2 the static pressure drop as a function of mesh resolution is presented. To evaluate which definition of the mesh generation should be used, the pressure drop over the heat exchanger core was evaluated. It can be seen that the pressure drop was strongly dependent on the mesh definition. For a total cell count larger than  $32.9 \times 10^6$  cells the pressure drop was no longer significantly affected. After evaluation of the airflow

characteristics and the resolution of the boundary layer the configuration with a total cell count of  $32.9 \times 10^6$  was chosen for these simulations. This is a higher cell count in relation to preceding work [27, 26, 50, 18].

Table 3.2: Static pressure drop for varying mesh resolutions.

<i>Growthrate</i>	<i>Surf.[mm]</i>	<i>Ref.fin</i>	<i>prism</i>	<i>cells</i> [ $\cdot 10^6$ ]	$\Delta P_{core}$ [Pa]
slow	0.1	0.5	9	0.5	323
medium	0.05	0.5	9	3.8	284
very slow	0.05	0.05	9	8.8	275
very slow	0.025	0.05	4	25.2	247
slow	0.025	0.1	9	25.4	249
very slow	0.025	0.05	9	32.9	243
very slow	0.025	0.025	9	53.4	245

The mesh for the final set-up can be seen in figure 3.19, where detail pictures show critical areas. The  $y^+$  value for the final mesh was less than one.

For the thermal simulations the mesh was re-produced, as well as the solid parts. The number of cells for the solid parts were  $7.4 \times 10^6$ , where the base size was defined as  $0.025mm$ , resulting in four cells in height for the fin.

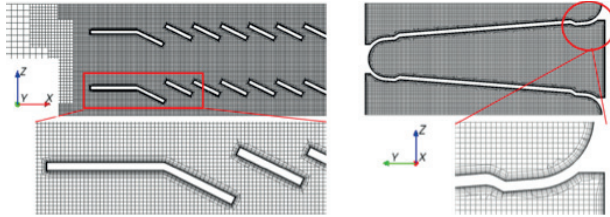


Figure 3.19: Mesh resolution on the centreline plane along, and a plane across, the computational domain.

---

## 4 Results and discussion

In this chapter the results are presented. The first sub-chapter defines the loss coefficients along the experimental set-up as a consequence of its design, based on experimental and simulated results. The three following sub-chapters present results from experiments and simulations of the experimental set-up and for one period of a fin. The final sub-chapter discusses the airflow uniformity over the heat exchanger surface in angled condition.

### 4.1 Airflow observations of experimental set-up

By using the total pressure balance equations for the experimental set-up, defined in Chapter 3.2.1, together with information from experiments and CFD simulations of the experimental set-up in isothermal condition, the airflow loss coefficients can be defined.

The losses from the inlet chamber to the angling of the heat exchanger was described by the loss factors  $k_1$  and  $k_4$ , in equation 3.8 and 3.12. The sum of the coefficients had a value between 0.06 and 0.25, resulting in a pressure drop of  $5 - 14Pa$  at a mass airflow rate of  $4.6kg/s$ . The higher values were seen for the  $60^\circ$  angled heat exchangers. The pressure drop mainly arose within the duct as the  $k_1$  coefficient was significantly smaller. Losses were created at the bell-mouth, at the pitot-static tube, as well as in the boundary layer. In figure 4.1 a plot of total pressure contours on the centreline plane is shown for a heat exchanger angled in  $30^\circ$ , at the highest simulated velocity. Note the narrow range of the scale and that values outside the margins were not included. It was seen that there were negligible losses over the bell-mouth and the static pressure was converted into dynamic pressure due to the area contraction, a constant mass airflow rate and small losses. This was also observed for control measurements from the experiments, where the static pressure loss from the inlet chamber over the bell-mouth and to the Prandtl tube, was within 1.5% of the differential pressure drop from the inlet chamber to the reference position in the outlet chamber. The values were recorded for a number of tests and confirmed the behaviour seen in CFD. The study carried out by Kim et al. [40], where no bell-mouth was mounted to the inlet duct, presented a pressure drop due to the entrance duct of up to 11% of the static pressure drop.

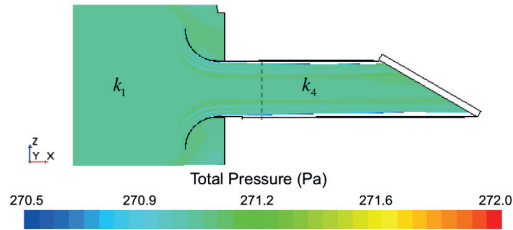


Figure 4.1: Plot of total pressure on the centreline plane for the  $30^\circ$  configuration.

Therefore, the shape of the bell-mouth was of great importance to minimize pressure losses. The one used for the experiments had the same radius,  $250\text{mm}$ , on all four sides, but not the same length on the sides as at the top/bottom of the duct. It was seen that the airflow at the sides of the bell-mouth, which had a length of  $105\text{mm}$ , having too short profile, generated a small detached flow region. The top/bottom rounding had a length of  $250\text{mm}$ . In figure 4.2 a velocity vector plot at the bell-mouth is presented. The left picture shows the plot of the top, and the right picture shows the side, with the detached area highlighted.

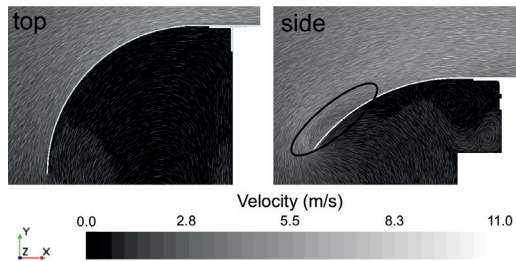


Figure 4.2: Plot of velocity vector at the bell-mouth.

From CFD simulations the flow-field effects from the pitot-static tube, which was mounted at the inlet duct, were observed. Its diameter was  $10\text{mm}$  and a separated region was created behind it. Even though it was mounted  $1.4\text{m}$  in front of the heat exchanger, the airflow was not totally uniform at the core entrance. The effect can be seen in figure 4.3, where a low velocity region can be seen at the centre of the core.

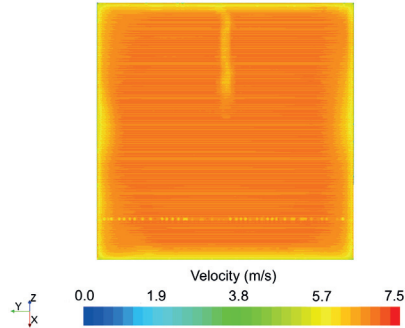


Figure 4.3: Velocity distribution at the heat exchanger entrance.

Since the same pitot-static tube was used for all tests its effect became more significant for the  $10^\circ$  angled heat exchanger, where it covered a larger part of the duct. In figure 4.4 the velocity magnitude contours are plotted on the centreline for the  $10^\circ$  and the  $60^\circ$  arrangements.

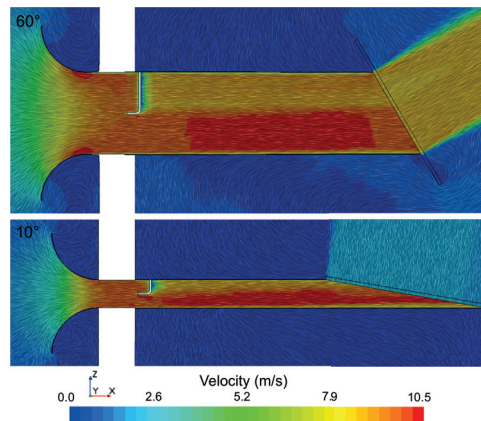


Figure 4.4: Plot of velocity magnitude on the centreline plane.

The boundary layer was growing as the air travelled along the duct, seen in figure 4.1. The increased boundary layer thickness decreased the cross-sectional area available for the air to pass, which accelerated the airflow. As Bernoulli theory tells, the static pressure was reduced. This can be observed in the duct between the measuring position,  $p_{duct}$ , and the heat exchanger core, seen in the static pressure plot in figure 4.5. First the static pressure was reduced as a result of boundary layer growth, which increased the dynamic pressure. As the airflow reached the core the air decelerated for the angled arrangements, as a consequence of the area expansion at the core. The dynamic pressure near the core was decreased, which increased the static pressure, also seen in figure 4.5. Hence, the total pressure along the duct was approximately constant, due to small losses.

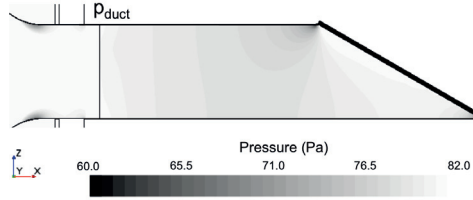


Figure 4.5: Static pressure within the duct

From the CFD simulations it was seen that a large area of losses was created just at the core entrance, where the airflow was forced to be re-directed into the heat exchanger. This angling loss was described by the change in dynamic pressure in the duct and at the core entrance, defined in equation 3.12. The losses increased for a more inclined heat exchanger, described by the term:  $1 - \sin^2\alpha$ , which was equal to 0.25, 0.75, and 0.97 for the  $60^\circ$ ,  $30^\circ$  and the  $10^\circ$  angled heat exchangers, since it was only dependent on the magnitude of the angle. To calculate the pressure loss, the term was multiplied by the dynamic pressure in the duct. The resulting loss just in front of the heat exchanger, due to the re-direction of the airflow, had a higher contribution to the total loss for a more angled heat exchanger. The values were independent of the core thickness and were equal to 14, 43 and 56Pa for the  $60^\circ$ ,  $30^\circ$  and the  $10^\circ$  arrangements respectively, at the highest tested mass airflow rate. In figure 4.4, where the velocity is plotted, the reduced velocity at the entrance of the core can be seen. For the  $10^\circ$  inclination a much higher loss in dynamic pressure can be seen relative to the  $60^\circ$  arrangement.

Excluding the losses over the core, the other main loss occurred at the exit of the heat exchanger, where the dynamic pressure was lost. The fourth term in the expression describing the total pressure balance in equation 3.11, was equal to zero since the velocity in the reference position in the outlet chamber was zero. The loss factor,  $k_3$ , was near a value of 1, which was multiplied by the dynamic pressure at the radiator outlet. By re-defining the loss factor to be dependent on the dynamic pressure in the duct, the loss factor would be multiplied by  $\sin^2\alpha$ . This term followed the opposite behaviour to the loss term at the entrance region of the heat exchanger, with a decreased value for a more inclined arrangement. Therefore, the loss factor at the outlet was smaller for a more inclined heat exchanger, due to the larger loss at the core entrance. The exit loss factor as a function of the dynamic pressure in the duct was equal to 1.0, 0.8, 0.25, 0.03 respectively, when starting with the least inclined arrangement,  $90^\circ$ .

The total loss factor for the complete test set-up varied between the inclinations, where the averaged value was 1.13 for both thicknesses of the heat exchangers. In Table 4.1 the individual total loss factors are presented for the  $19\text{mm}$  and the  $52\text{mm}$  thick heat exchangers with symmetric louvered fins. It can be seen that the individual  $K_{tot}$  value for a specific inclination was independent of the core thickness for the tested heat exchangers, but varied for different inclination magnitudes. The individual values of the coefficients were a little higher for the  $60^\circ$  angle. From these results the  $K_{tot}$  factor was defined as 1.13 for all

inclinations. Though, it is important to bear in mind that the value varied a bit between the inclination angles.

Table 4.1: Individual and averaged total loss factor values,  $K_{tot}$ , for the different heat exchangers and inclination angles.

Thickness	90°	60°	30°	10°	Averaged $K_{tot}$
	Individual $K_{tot}$				
19mm	1.10	1.24	1.05	1.11	1.13
52mm	1.09	1.25	1.07	1.12	1.13

To evaluate the static pressure drop due only to the core, from the experiments, the derived total loss factor multiplied by the dynamic pressure in the duct, should be subtracted from the differential chamber pressure. In order to obtain the losses just over the heat exchanger core, the dynamic pressure at the chamber inlet should also be subtracted. The equation to find the static pressure drop over the heat exchanger is defined in equation 4.1, where  $K_{tot}$  is the total loss factor, defined in equation 4.2.

$$\Delta p_{core} = \Delta p_{chamber} - K_{tot} \frac{1}{2} \rho V_{duct}^2 \quad (4.1)$$

$$K_{tot} = k_1 + k_4 + (1 - \sin^2 \alpha) + k_3 \sin^2 \alpha - \left( \frac{A_{duct}}{A_{chamber,in}} \right)^2 \quad (4.2)$$

To obtain the pressure drop from the entrance duct to the reference position at the outlet chamber, equation 4.3 was applied. Since the  $k_1$  coefficient and the area ratio term was small, the differential pressure at the duct and the reference position, was approximately equal to the chamber pressure drop minus one dynamic pressure defined in the duct.

$$\Delta p_{duct} = \Delta p_{chamber} - \left( 1 + k_1 - \left( \frac{A_{duct}}{A_{chamber,in}} \right)^2 \right) \frac{1}{2} \rho V_{duct}^2 \quad (4.3)$$

## 4.2 Experimental results

The sub-chapters for the experiments are divided into three parts, representing results based on isothermal and thermal conditions as well as a comparison of heat exchanger thicknesses and inclination angles for different dimensioning criterias.

### 4.2.1 Isothermal experimental results

According to the information defined in the methodology the differential pressure drop presented from the experimental data was based on the chamber pressure drop,  $\Delta p_{chamber}$ . When the differential pressure drop is provided from the duct to the reference position or over the core, the previously defined equations in Chapter 3.2.1 have been applied with the derived loss coefficients in Chapter 4.1.

As a reminder: since the mass airflow rate was definition as constant for the 90°, 60° and 30° inclinations, the velocity through the heat exchanger core was decreased for a higher inclination. The results can either be evaluated regarding a constant mass airflow rate or the velocity of the air through the core. Since the pressure drop is a function of the speed of the air through the core, it is important to evaluate both scenarios. In figure 4.6 and 4.8 the duct differential pressure is presented as a function of both parameters, for the symmetric louvered finned heat exchangers in the downflow orientation. For an installation in a vehicle, where a pre-defined area is available, a larger core area would be seen for a more inclined heat exchanger. The pressure drop as a function of mass airflow rate should then be evaluated. From these graphs it can be seen that the pressure drop decreased for an increased inclination angle, as a result of the decreased airspeed through the core, which is according to equation 2.1.

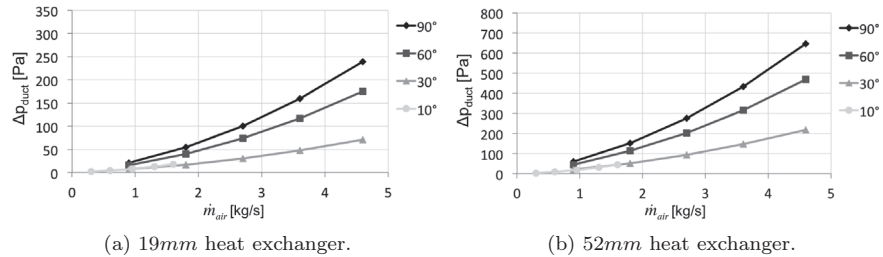


Figure 4.6: Duct pressure drop as a function of mass airflow rate, for the symmetric louvered finned heat exchangers.

The velocity in the duct was defined to be the same for all arrangements, resulting in lower mass airflow rates for the 10° inclination. To be consistent the pressure drop values for these cases should be re-calculated for a duct height of 444mm. Though, since the velocity in the ducts was constant, as well as in the core, the pressure drop was not affected. Therefore, the mass airflow rates for the 10° angle were multiplied by a factor of 444/154 to find the mass airflow rate in the higher duct. The curves for the 10° angles were translated to be under the 30° curves, with the same pressure drop values as previous but with the higher mass airflow rates seen in figure 4.7. Consequently, these arrangements generated the lowest pressure drops at a specific mass airflow rate, when comparing all inclinations for the same duct height. With the higher duct height the core of the heat exchanger was approximately three times larger than for the lower one, which result in an unrealistic large heat exchanger.

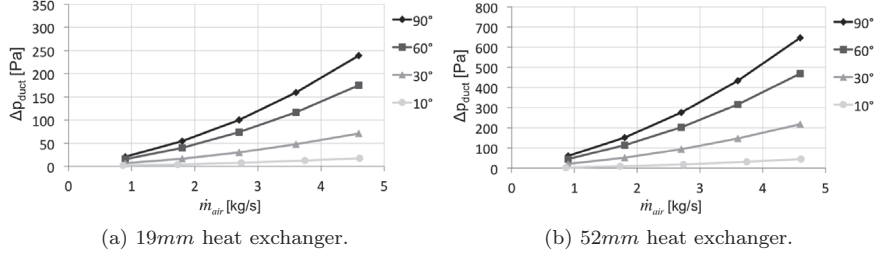


Figure 4.7: Duct pressure drop as a function of mass airflow rate, for the symmetric louvered finned heat exchangers.

When the pressure drop was evaluated as a function of the airspeed through the core the values were more similar, seen in figure 4.8. The curves were almost in-line, and the static pressure drops were marginally affected by the angling. This result was independent of the thickness of the heat exchanger. It can be seen that the perpendicular arrangement generally generated the highest pressure drop for a given core speed. For this set-up an outlet duct was present, which added somewhere between  $4 - 9Pa$  to the static pressure loss. These values were obtained from control measurements, performed with and without an outlet duct for the  $90^\circ$  arrangement. An extra loss when having the outlet duct was as a consequence of friction losses in the boundary layer as well as the acceleration of the airflow due to the area contraction of the boundary growth. This increase in dynamic pressure was lost behind the duct. The presented values in the plot are not compensated for this pressure loss.

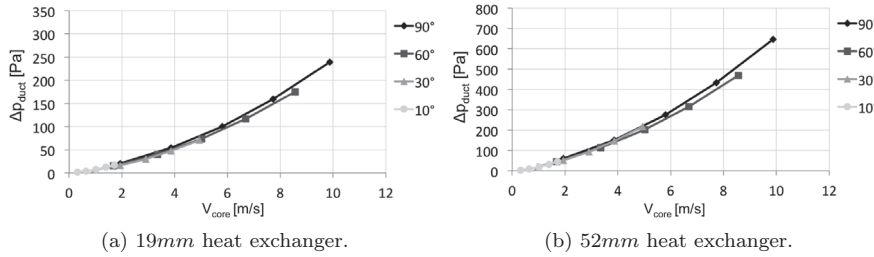


Figure 4.8: Duct pressure drop as a function of airspeed through the core, for the symmetric louvered finned heat exchangers.

It has been shown that the static pressure loss was marginally affected by the angle of the heat exchanger. By plotting the total pressure drop from the duct to the reference position the dynamic effects will also be counted. Due to small losses from the entrance chamber until the duct, the total pressure drop over the chambers and from the duct to the outlet chamber could be considered as constant. Together with low dynamic pressure at the inlet chamber the static chamber pressure loss as a function of the core velocity can be plotted to evaluate the total pressure loss from the duct to the outlet chamber. In

figure 4.9 these parameters are plotted for the symmetric louvered finned heat exchangers. It can be seen that the total pressure drop was increased for a more inclined arrangement, which was the dynamic pressure loss effect. It can also be seen that the total pressure drop for 60° angled heat exchanger was not affected compared to the 90° arrangement. Therefore, the results indicated that the angling of the heat exchanger only affected the dynamic pressure and not the static pressure, which also can be seen in figure 4.8. CFD simulations of one period of a fin were carried out to gather more information of the airflow phenomena within the core, to be able to better understand the experimental results.

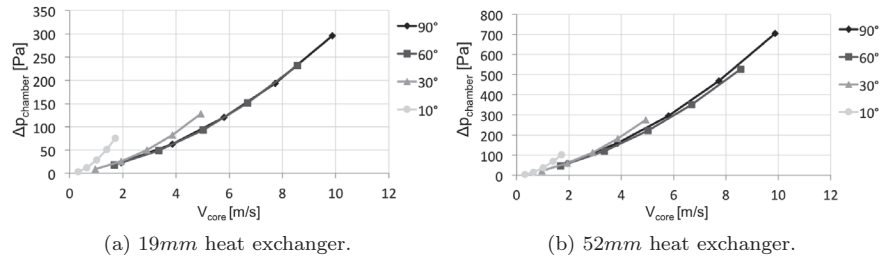


Figure 4.9: Chamber pressure drop as a function of airspeed through the core.

To evaluate the percentage increase in pressure drop relative to the perpendicular arrangement, the relative duct pressure drop can be plotted for different inclinations. In figure 4.10 this information is shown for the 19mm heat exchanger with symmetric louvered fins, with a core velocity of 2m/s. It can be seen that the pressure drop was fairly constant.

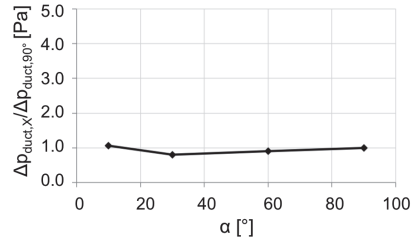


Figure 4.10: Percentage variation in differential pressure drop between the duct and the outlet chamber, for an inclined heat exchanger, relative to the perpendicular arrangement.

The corresponding graph for the total pressure drop would look like in figure 4.11. It can be seen that the pressure drop was increased for an increased angle, where it was substantially increased for the 10° arrangement. A similar graph was plotted by Nichols [39], with similar behaviour of the pressure drop at different inclination angles. This study also showed a substantial increase at an angle of 10°, where the pressure drop went towards infinity.

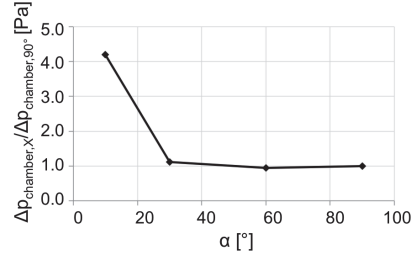


Figure 4.11: Percentage variation in differential pressure drop between the inlet and outlet chamber, for an inclined heat exchanger, relative to the perpendicular arrangement.

### Heat exchanger orientation and internal design

The heat exchangers were mounted in two orientations; downflow and crossflow to evaluate if one orientation was preferable regarding pressure drop. In figure 4.12 the chamber pressure drop is presented for the symmetric louvered heat exchangers. For both thicknesses of heat exchangers the crossflow orientations generated a higher pressure drop. The pressure drop was increased by 2–6% for all inclinations for the highest tested mass airflow rate. The larger percentage deviations were seen for more inclined heat exchangers and at lower airflow rates.

The pressure drop was expected to be lowered for the crossflow-oriented heat exchanger since airflow was angled relative the tube. Due to the greater radius of the tube compared to the fin the detached areas at the inlet, as well as at the outlet of the core, were expected to be reduced.

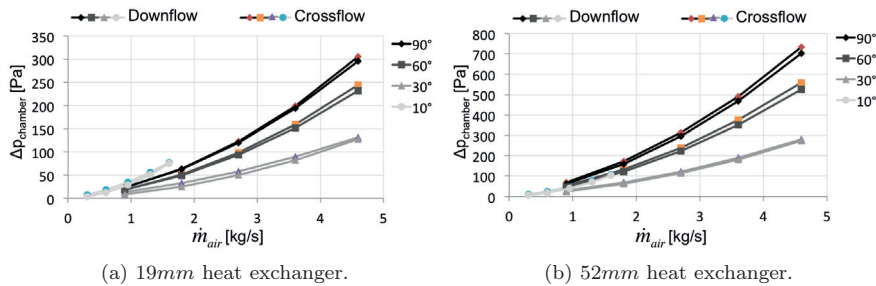


Figure 4.12: Chamber pressure drop as a function of mass airflow rate, for the downflow and crossflow orientations.

Two 19mm thick heat exchangers were evaluated with different internal designs. One had symmetric louvered fins and the other had the louvers in only one direction: asymmetric louvered fins. The experiments were limited to test the

latter heat exchanger in only downflow condition. A comparison of the chamber pressure drop for the different core geometries is presented in figure 4.13.

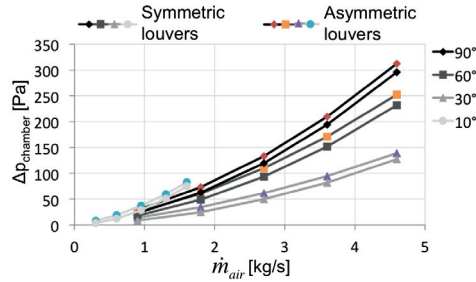


Figure 4.13: Chamber pressure drop dependence on core geometry, for the 19mm thick heat exchangers.

For the asymmetric heat exchanger the chamber pressure drop was increased for all inclinations and mass airflow rates, compared to the symmetric louvered heat exchanger. The percentage deviation became smaller for increased mass airflow rates. For the highest airflow rate the difference in chamber pressure drop was 5 – 9%.

#### 4.2.2 Thermal experimental results

The pressure drop for the different installations followed the same trends as for the isothermal results. The values were a little higher since the specific volume was increased due to the decreased density, which resulted in an accelerated airflow due to the expansion effect of the heated air. The increased air velocity will increase the pressure drop, which is according to equation 2.1. This chapter will focus on heat transfer, where the  $\epsilon - NTU$  method, described in Appendix A, was applied to the experimental data.

Five liquid flow rates were tested, where the main presented results are based on the highest rested value. In figure 4.14 the chamber pressure drop and the heat transfer rate for the 19mm heat exchanger in 90° is presented for all mass liquid flow rates. It can be seen that the chamber pressure drop was not significantly affected by the mass liquid flow rate. The heat transfer rate on the other hand increased for an increased mass liquid flow rate.

## 4.2 Experimental results

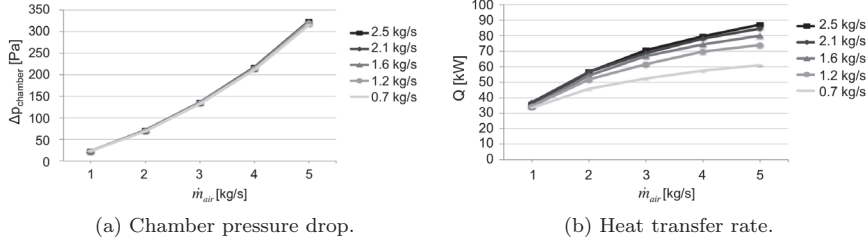


Figure 4.14: Pressure drop and heat transfer rates for all tested liquid flow rates, for the 19mm symmetric louvered finned heat exchanger.

In figure 4.15 the heat transfer rate is presented as a function of mass airflow rate, for the symmetric louvered finned heat exchangers in downflow arrangement. The values presented are based on the highest tested liquid flow rate.

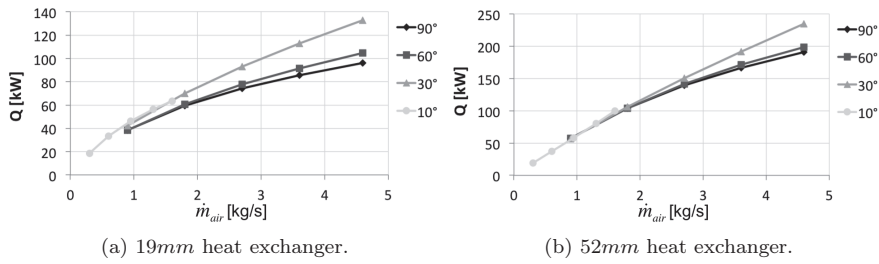


Figure 4.15: Heat transfer as a function of mass airflow rate, for the symmetric louvered finned heat exchangers.

There are two explanations to the increased heat transfer rate for a more inclined heat exchanger, for the same mass airflow rate: the first being the increased transmitting area; the second being the decreased velocity of the airflow, which increased the temperature of the air exiting the core. This resulted in a higher temperature difference of the air at the in- and outlet of the core, which increased the heat transfer rate according to equation 2.3. For the 10° and the 30° angles the heat transfer rates were almost in-line; the reason being that the complete core was exposed to the incoming airflow. A lower gain in heat transfer rate was observed for the thicker heat exchanger since the temperature of the air was heated to the coolant temperature as a consequence of the increased depth of the core. Hence, the temperature difference of the air and the liquid was lower after passing half the core thickness, and even less at the exit, compared to the thinner heat exchangers. Bigger changes in heat transfer rates were seen at higher mass airflow rates of the air, due to the increased temperature difference of the liquid to the air. At lower airflow rates the heat transfer rate was almost independent of the heat exchanger angle, due to the small temperature difference between the coolant and the air.

It will be seen in figure 4.16, where heat transfer is presented as a function of velocity through the core, that the heat transfer rate was constant for the 10° and 30° angles, for a constant airspeed through the core.

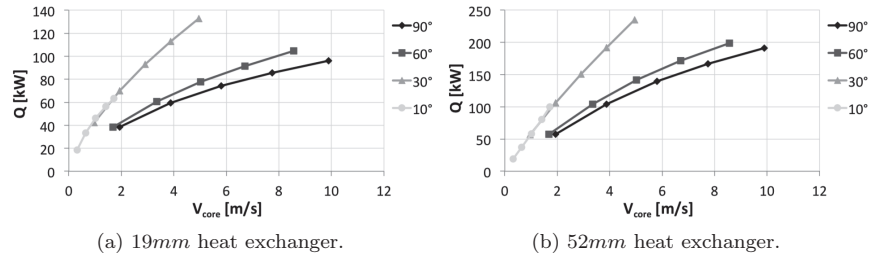


Figure 4.16: Heat transfer rate as a function of airspeed through the core.

It can be seen in the graph that the heat transfer rate for the 30° arrangement was nearly twice the value for the 90° arrangement. The core area was doubled as well as the mass airflow rate, to achieve the same air velocity through the core compared to the perpendicular mounted heat exchanger. The heat transfer rate was less than double since the 90° orientation functioned more efficiently. CFD simulations of the inner parts of the core will explain the physical phenomena to this result.

### Heat exchanger orientation

In figure 4.17 the heat transfer rate as a function of mass airflow rate for the 19mm heat exchanger is shown. It can be seen that the heat exchanger in downflow arrangement generated increased heat transfer and at the same time achieved a slightly lower static pressure drop than the crossflow orientation, seen in figure 4.12.

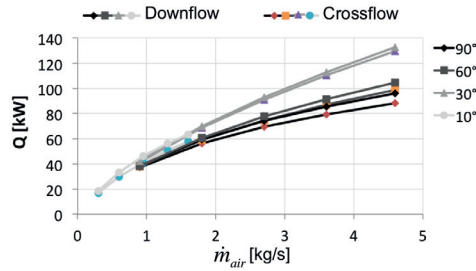


Figure 4.17: Heat transfer as a function of mass airflow rate, for the downflow and crossflow orientations for the 19mm thick heat exchanger.

When evaluating the downflow compared to the crossflow orientation, the number of tubes subjected to the incoming airflow varied even though the total

tube lengths were constant for both scenarios. For the downflow arrangement all tubes were exposed to the incoming airflow. Though, at  $90^\circ$ , only half the length of the tubes were within the duct. For the crossflow configurations the number of tubes subjected to the incoming airflow increased for a more inclined arrangement; for the  $90^\circ$  and  $60^\circ$  configurations some of the tubes were not exposed to the airflow at all. As a consequence of not having all tubes exposed to the air, the temperature of the liquid at the exit for some of the tubes was the same as at the entrance:  $90^\circ\text{C}$ . Within the outlet tank the liquid from the tubes was mixed, resulting in an averaged temperature, which was the one that was measured. In figure 4.18 an example of the temperature difference between the downflow and crossflow orientations, from experimental data, is shown for the  $90^\circ$  configurations. For this example the mass airflow was set to  $2.7\text{kg/s}$  and the liquid flow rate to  $1.25\text{kg/s}$ .

The measured temperature at the outlet was higher for the crossflow orientation, resulting in a lower temperature difference between the in- and outlet, generating a lower heat transfer rate, also visible in figure 4.17. The resulting heat transfer rates were  $73\text{kW}$  and  $66\text{kW}$ , for the two orientations.

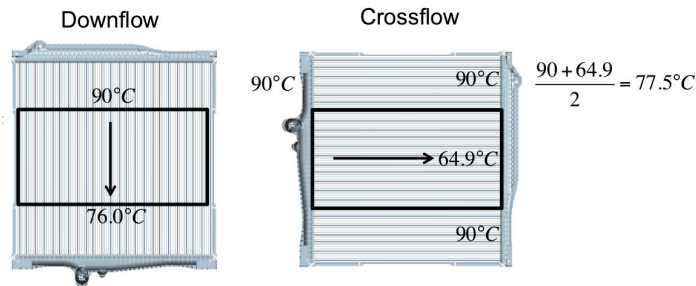


Figure 4.18: Temperature differences for the downflow and the crossflow configurations.

When installing an angled heat exchanger in a vehicle the complete core would be exposed to the incoming airflow, for both orientations. The size of the heat exchanger would therefore not be as the ones that were tested. For a downflow arrangement the heat transfer rate would not be affected for a real installation compared to the experimental data. The reason being that all tubes were subjected to the incoming airflow and since parts of the core outside the duct were insulated. For the crossflow-oriented heat exchanger the heat transfer rate would vary for a real installation compared to the tests. In an installation all tubes would be exposed to the airflow, which was not the scenario for the experiments for the  $90^\circ$  and  $60^\circ$  angles.

When assuming a constant velocity of the liquid through the core, a higher temperature difference of the liquid at the in- and outlet of the tubes would be seen for the crossflow orientation in  $90^\circ$ , with all tubes exposed to the air, compared to the downflow orientation. The reason being the longer distance between the tanks. This would affect the heat transfer rate compared to the

measured test values. This can also be seen in figure 4.18, where the temperature at the outlet tank was 64.9°C for the crossflow-oriented heat exchanger, when the velocity of the liquid in the core was the same.

In table 4.2 and 4.3 a comparison of both scenarios, with the temperature at the outlet of the tubes, the thermal conductivity, and the heat transfer rate presented. For this example the core areas were defined, as it should have been in a vehicle installation, with the complete core area subjected to the air. The inlet temperature of the air was 25°C and for the liquid, 90°C. It can be seen that when the liquid flow rate was half for the crossflow orientation, which resulted in the same velocity in the core compared to the downflow configuration, the overall heat transfer rate was increased for the downflow arrangement. This was because the mass liquid flow rate was doubled, for the downflow orientations and the temperature difference of the liquid, at the in- and outlet, was not doubled for the crossflow-oriented heat exchanger. For the second scenario, with a constant mass liquid flow rate in the system, resulting in doubled velocity of the liquid for the crossflow configurations, this case also resulted in a higher heat transfer rate. As a result of the increased speed of the liquid, the convective heat transfer coefficient at the tube wall,  $\alpha$ , increased for an increased Reynolds number, whereas the overall heat transfer coefficient,  $K$ , increased, according to equation A.5 in Appendix A.

Table 4.2: Constant velocity of the liquid within the tubes.

Orientation	$\dot{m}_{liquid}$ [kg/s]	$\dot{m}_{air}$ [kg/s]	$T_{out,liquid}$ [°C]	$KA$ [kW/K]	$Q$ [kW]
Downflow	2.50	4.6	81.5	1.76	88.9
Downflow	2.50	2.7	82.5	1.75	79.1
Downflow	2.50	0.9	85.3	1.74	48.9
Crossflow	1.25	4.6	74.0	1.78	83.9
Crossflow	1.25	2.7	75.7	1.77	75.3
Crossflow	1.25	0.9	80.9	1.76	47.8

Table 4.3: Constant flow rate of the liquid within the cooling circuit.

Orientation	$\dot{m}_{liquid}$ [kg/s]	$\dot{m}_{air}$ [kg/s]	$T_{out,liquid}$ [°C]	$KA$ [kW/K]	$Q$ [kW]
Downflow	2.50	4.6	81.5	1.76	88.9
Downflow	2.50	2.7	82.5	1.75	79.1
Downflow	2.50	0.9	85.3	1.74	48.9
Crossflow	2.50	4.6	81.3	1.82	91.3
Crossflow	2.50	2.7	82.3	1.81	80.9
Crossflow	2.50	0.9	85.3	1.80	49.5

The heat transfer rate can be evaluated in a more general way by deriving the overall heat transfer coefficient,  $K$ , for each configuration. This parameter is dependent on the speed of the fluids. For this evaluation the highest tested

liquid flow rate in combination with an airspeed of  $2m/s$  were defined. The  $\varepsilon - NTU$  method was applied to obtain the  $K$  values presented in figure 4.19 as a function of the inclination angle, for the thinner symmetric louvered finned heat exchanger in downflow condition. The results indicated that the overall heat transfer coefficient decreased for an increased inclination angle. These results indicate that the heat exchanger was more efficient for less inclination angles, which was also seen in figure 4.16.

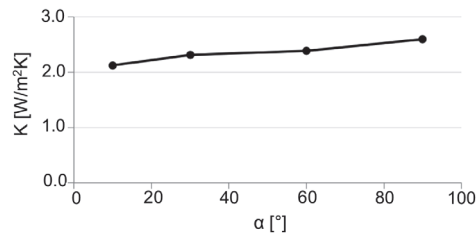


Figure 4.19: The overall heat transfer coefficient,  $K$ , as a function of heat exchanger inclination angle, for the  $19mm$  heat exchanger, in downflow condition.

### Internal geometry of the heat exchanger

Generally, increased heat transfer rates of 2 – 6% were seen for the asymmetric, compared to the symmetric louvered finned heat exchanger, for all mass airflow rates. For all mass airflow values the averaged percentage increase in heat transfer rate, for the  $30^\circ$  compared to the  $90^\circ$  orientation, was 26% for the symmetric and 30% for the asymmetric  $19mm$  thick heat exchanger. For the  $52mm$  heat exchanger the corresponding value was 11%.

#### 4.2.3 Heat exchanger layouts for angled installations

From this investigation the results give an indication of which heat exchanger thickness and inclination that should be used for a specific installation. To be able to draw such conclusions, dimensioning criterias have to be defined for parameters such as pressure drop, heat transfer rate and available mass airflow rate. The results can be evaluated by plotting the parameters in different combinations and holding some of them as constants.

In figure 4.20 these parameters as a function of inclination angle of the heat exchanger are plotted for all three heat exchangers in a downflow orientation. The values are plotted for the highest airflow and liquid flow rates, from the thermal experiments. To make the  $10^\circ$  angle comparable with the other angles the heat transfer and static pressure drop were re-calculated for a duct height of  $444mm$ . Since the experimental set-up was designed in a way that the velocity in the duct was equal for the two duct heights, the pressure drop was unaffected for the  $10^\circ$  angled arrangement. Hence, the pressure drop was independent of the duct height since the air velocity through the radiator was not changed.

The heat transfer rate on the other hand was affected due to the increased core area. To re-calculate the heat transfer rate for a  $10^\circ$  angled heat exchanger in a duct height of  $444\text{mm}$ , the  $\varepsilon - NTU$  method was applied. An increase from  $154\text{mm}$  to  $444\text{mm}$  resulted in an increased core area of approximately three times ( $444/154$ ), which affected the heat transfer rate. The mass airflow rate was increased to correspond to the same velocity in the duct as for the lower duct height. Since the thermal conductivity,  $KA$ , is dependent on the core area this parameter was first derived for the tested mass airflow rate and divided by the core area for the tested heat exchanger, to obtain the overall heat transfer coefficient,  $K$ . When calculating the heat transfer rate for the increased core area in the higher duct the derived  $K$  value, together with the increased core area were used to calculate the final heat transfer rate.

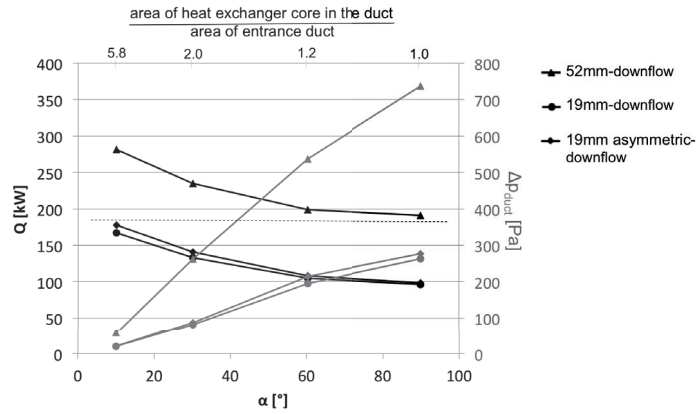


Figure 4.20: Heat transfer rate and pressure drop as a function of inclination angle, for the highest tested liquid and airflow rates.

Both pressure drop and heat transfer rate behaved similarly for all three heat exchangers. It can be seen that a more inclined arrangement resulted in higher heat transfer rates and at the same time gave lower static pressure drops. These results were to be expected since they were not normalized to the core area exposed to the incoming airflow. A dotted line is drawn in the plot in figure 4.20, enabled a comparison of implementing a thinner heat exchanger at a greater angle compared to a thicker heat exchanger at smaller angles. The heat transfer rate was approximately equal to  $180\text{kW}$  at the horizontal line. The corresponding pressure drop for the  $52\text{mm}$  heat exchanger at  $90^\circ$  was  $740\text{Pa}$ , and for the  $19\text{mm}$  heat exchanger at  $10^\circ$  was  $20\text{Pa}$ . Hence, the pressure drop for the thicker was higher compared to the thinner heat exchanger, at the same heat transfer rate. It should be mentioned that the core area at an inclination of  $10^\circ$  was unrealistic large.

A limitation could also be defined for pressure drop. Assuming a permitted pressure drop of  $280\text{Pa}$ : either a heat exchanger with a thickness of  $52\text{mm}$  at an angle of  $30^\circ$  or a  $19\text{mm}$  thick heat exchanger at  $90^\circ$  could be used. For the thicker heat exchanger the heat transfer rate was  $230\text{kW}$  and for the thinner  $100\text{kW}$ .

If the mass airflow was lowered to  $2.7\text{kg/s}$  and the liquid flow rate was unchanged, the diagram would be like figure 4.21. In this graph the dotted line is plotted for a pressure drop of  $120\text{Pa}$ . It can be seen that the heat transfer rate for the thicker heat exchanger at  $30^\circ$  was  $150\text{kW}$  and  $75\text{kW}$  for the thinner at  $90^\circ$ , resulting in a doubled heat transfer rate.

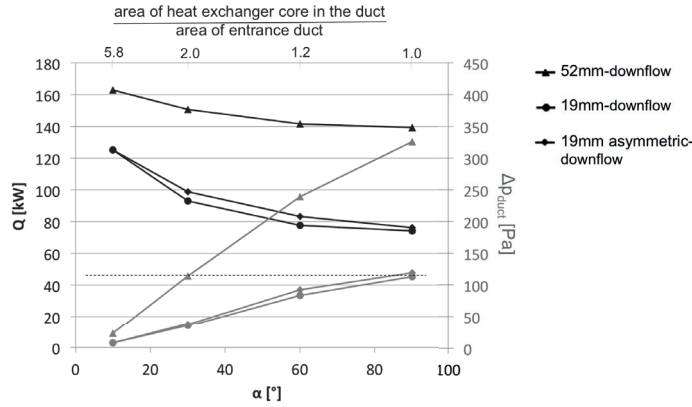


Figure 4.21: Heat transfer rate and pressure drop as a function of inclination angle, for a mass airflow rate of  $2.7\text{kg/s}$ .

To find the most suitable design of heat exchangers and its angle it is of great importance to know the operating condition, for the system to define critical parameters, which the system has to be dimensioned for. Another way to interpret the results, and to evaluate heat exchanger thickness and angle, is by defining a permitted static pressure drop. The mass airflow through the cooling package and the heat transfer will then vary between the inclined configurations. In figure 4.22 these parameters are plotted as a function of inclination angle, at a pressure drop of  $100\text{Pa}$  between the duct and the outlet chamber, for the downflow-oriented heat exchangers. To include the  $10^\circ$  configuration in the evaluation, the pressure drop and the heat transfer rates were re-calculated to the same duct size as was applied for the other angles, by using the  $\varepsilon - NTU$  method. The mass flow rate of the liquid was defined to be  $2.5\text{kg/s}$  and  $7.5\text{kg/s}$  for the  $19\text{mm}$  and  $52\text{mm}$  thick heat exchangers respectively, corresponding to a constant velocity of the liquid for both heat exchangers. It can be seen that the heat transfer rate increased for a more inclined heat exchanger, as a result of the increased core area and decreased velocity through the core. It can also be seen that the heat transfer rates were in-line for both thicknesses of the heat exchangers for angles tested between  $30^\circ$ - $90^\circ$ , with a mass airflow rate for the thinner approximately twice as large as for the thicker heat exchanger. For the most inclined configuration the mass airflow rates were outside the tested range, requiring extrapolation to find these results.

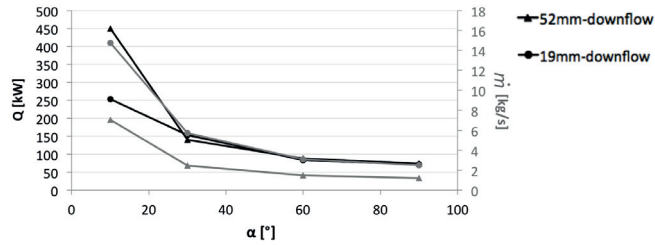


Figure 4.22: Heat transfer and mass airflow rate at a differential pressure drop of  $100Pa$  from the duct to the chamber outlet.

Another way to evaluate the impact of an angled heat exchanger within an installation is to include the fan in the analysis. Let's assume a comparison of a heat exchanger at  $90^\circ$  and one at  $30^\circ$  with the doubled core area and with the same thickness. Assume a constant air velocity through the core, resulting in double mass airflow rate through the system for the angled installation. No extra losses appear due to installation variations. Figure 4.23 shows a sketch of the two installations for the  $19mm$  heat exchanger. The pressure drop and heat transfer rate for the  $90^\circ$  installation were  $62Pa$  and  $54kW$ ; where the corresponding values for the  $30^\circ$  installation were  $48Pa$  and  $110kW$ . Pressure drop was decreased and heat transfer rate increased for the angled installation. If the same fan is used the rotation speed must increase for the angled arrangement to double the mass airflow rate. The system curve for the fan will be lowered, resulting in a higher volumetric flow rate and higher power consumption. To specify the size or speed of the fan the fan laws, defined in Appendix C, can be applied to re-calculate the values of the parameters.

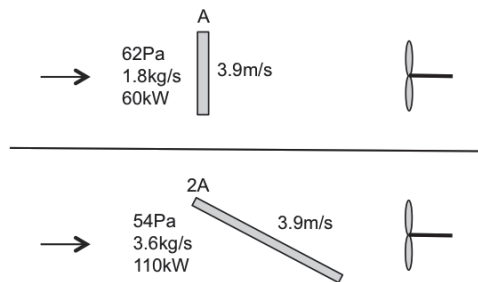


Figure 4.23: Sketch of hypothetical installations for the  $19mm$  heat exchanger at  $90^\circ$  and  $30^\circ$ .

If a higher heat transfer rate is required for the perpendicular installation a thicker heat exchanger could be installed. If the  $52mm$  thick heat exchanger would be installed instead, the heat transfer rate would be increased to approximately  $104kW$ . Although, for this installation the pressure drop would be increased to  $183Pa$ , for the defined mass airflow rate. This specific scenario is shown in figure 4.24.

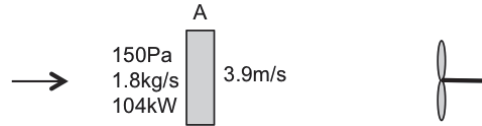


Figure 4.24: Sketch of hypothetical installations for the  $52\text{mm}$  heat exchanger at  $90^\circ$ .

### 4.3 CFD simulations of the experimental set-up

When the test set-up was initially defined, it was planned to include a downstream duct behind the heat exchanger to measure static and total pressure. CFD simulations were performed at an early stage in the project, in parallel with the experiments. From CFD it was detected that the outlet duct generated a significant flow resistance and the pressure drop over the rig increased substantially. In figure 4.25 velocity contour plots, on the centreline plane of the test set-up, with and without the downstream duct, are shown. For the  $90^\circ$  orientation the airflow characteristics and pressure drop were not significantly affected. The chamber pressure drop was increased by  $4 - 9\text{Pa}$  with a downstream duct, for the highest mass airflow rate, obtained from experiments control measurements. From the CFD simulation the corresponding value was around  $6\text{Pa}$ . Larger effects were seen when the heat exchangers were tilted, seen in the lower pictures.

As a consequence of the outlet duct a separated flow area was created behind the heat exchanger, reducing the area available for the airflow to pass, which accelerated the air at the upper part of the duct. For the  $30^\circ$  angle the chamber pressure drop was increased from  $139\text{Pa}$  to  $297\text{Pa}$  when the downstream duct was installed, for the highest tested mass airflow rate. Hence, the geometry around the heat exchanger generated a higher pressure drop than the heat exchanger itself. Effects due to the outlet duct are further explained in Paper II. The flow-separated areas, created at the downstream duct were also observed in the work presented by Rivers et al. [41]. From the results obtained from CFD simulations it was concluded that tests for angled heat exchangers should be performed without the downstream duct.

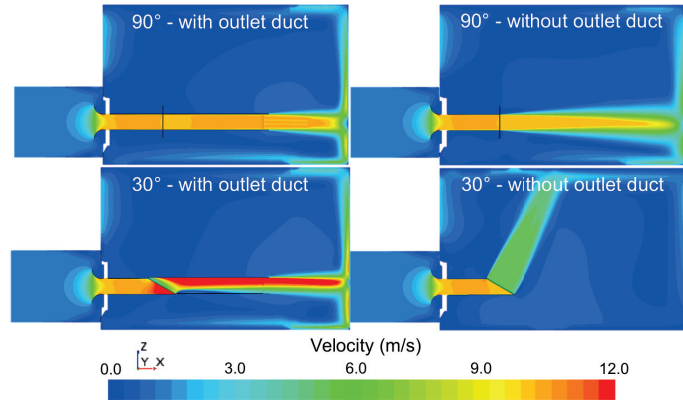


Figure 4.25: Effects of a downstream duct.

The flow-field was affected as in figure 4.26, with and without an outlet duct behind the core. It can be seen that the airflow uniformity was affected by the downstream duct. The flow-field was directed downward in the duct in front of the core, whereas a higher velocity can be seen in the lower parts of the core. For the configuration without the downstream duct the airflow was more uniform.

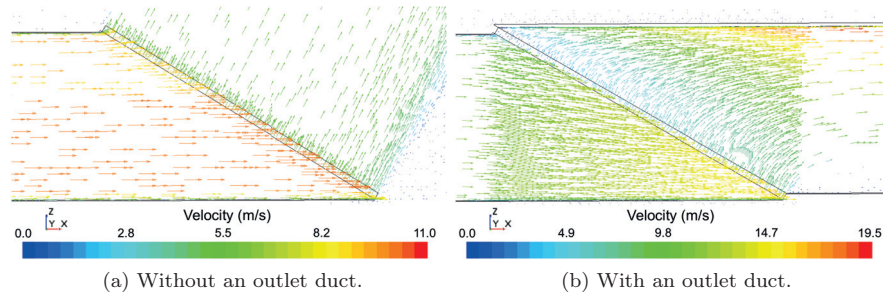


Figure 4.26: Velocity vectors at the inlet duct, the core and behind the core for the 19mm heat exchanger for the highest mass airflow rate.

As for the experiments differential static pressure measured at the inlet and outlet chambers,  $\Delta p_{chamber}$ , was used as a reference for pressure analysis. The values of this parameter were compared for the experimental and the simulated results, to evaluate the correlation between the methods. This is shown in figure 4.27, based on the final porosity factors and core mesh definition, described in Appendix B. The values from CFD were obtained by defining measuring points at the same locations as in the experiments. In the diagram the CFD results are marked as points, while the test results are marked as lines. It can be seen that the results from the two methods correlated well.

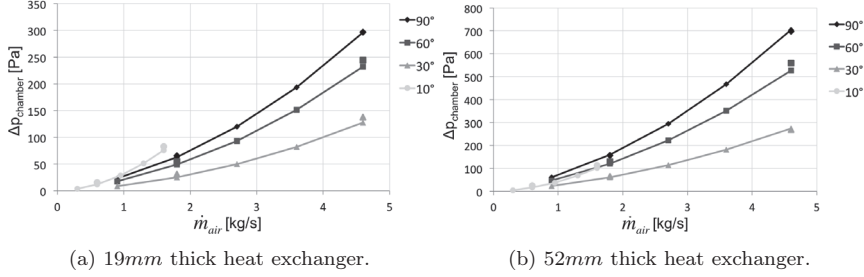


Figure 4.27: Chamber static pressure drop as a function of mass airflow rate, from experiments and CFD simulations of the experimental set-up.

At  $90^\circ$  the pressure drops were identical for the two methods, because the porosity coefficients were derived from the experimental data with the heat exchanger perpendicular to the airflow. It can be seen that there were deviations between simulations and experiments for the tilted configurations. The percentage deviation increased with an increased inclination angle, up to a maximum value of 9%. Lower deviations were seen for the less inclined heat exchangers, with a deviation of 5% for the  $60^\circ$ , and 7% for the  $30^\circ$  arrangement. If the porosity coefficients were derived for each inclination the deviations would be reduced. Since heat exchanger components are normally tested at  $90^\circ$  and not in angled arrangements, porosity coefficients derived from the perpendicular case are preferable. An accurate approximation of the resistance for an angled heat exchanger can be obtained by using this method, where the deviations are estimated.

To obtain the pressure drop solely due to the core in a specific arrangement, the core pressure drop defined by equation 4.1, with the derived loss coefficients, were analysed for the experimental and simulated results. The comparison is shown in figure 4.28. For the  $90^\circ$  and  $60^\circ$  inclinations variations were within 7%. For the more inclined heat exchangers, which experienced lower airspeeds through the core, larger variations were seen. One reason for the deviation was due to the forced re-direction of the airflow at the core entrance, as a consequence of the porosity definition in CFD. The airflow experienced an abrupt variation in condition and some of the losses appeared in the cell just in front of the core interface and some at the first cell behind it, within the core. In reality the airflow was forced to be re-directed as well, but most likely not as abruptly as at the interface of two continuums.

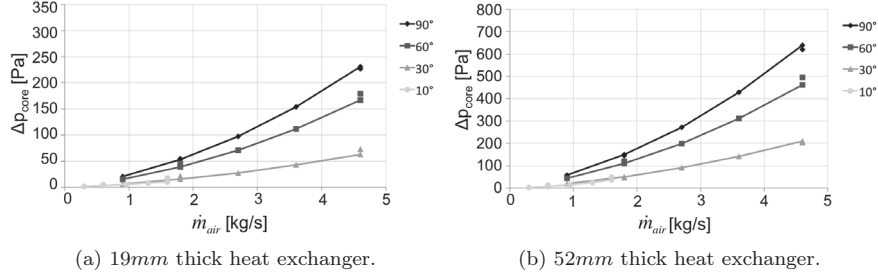


Figure 4.28: Pressure drop solely due to the heat exchanger core, as a function of mass airflow rate.

From CFD simulations, detailed information can be extracted, which can be hard to measure in an experiment. To evaluate the airflow through the test set-up the velocity and static pressure distribution can be plotted, presented in figure 4.29 for the 19mm heat exchanger in 30° angle. An acceleration of the airflow can be seen at the entrance of the bell-mouth into the duct, as a result of the area contraction. Since there was no leakage within the set-up, and small losses in this region have previously been shown, the increase in dynamic pressure corresponded to almost exactly to the reduction in static pressure, seen in the pressure plot. In figure 4.29 the disturbances in the flow-field as a consequence of the pitot-static tube can be seen, which affected the velocity of the air approaching the heat exchanger core. The static pressure was lost through the core and was almost equal to zero in the outlet chamber. Behind the core the dynamic pressure was dissipated and equal to zero at the reference position, where the gauge pressure was also zero.

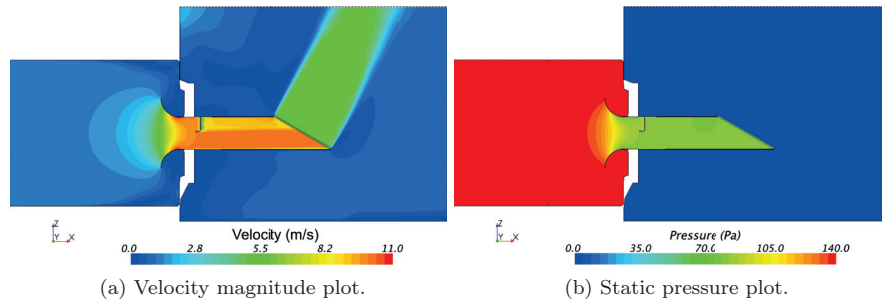


Figure 4.29: Velocity and static pressure visualisation on the centreline of the experimental set-up, for the 19mm heat exchanger in 30° angle, at a mass airflow rate of 4.6kg/s.

Areas of losses can be illustrated by plotting iso-surfaces of total pressure equal to the pressure at the chamber inlet. The plotted zones correspond to areas where lower total pressure, compared to at the entrance, occurred and therefore

represent areas of losses. These zones at the entrance duct are shown in figure 4.30 for the  $90^\circ$  and  $10^\circ$  angled heat exchangers, with a mass airflow rate of  $4.6\text{kg/s}$  and  $1.6\text{kg/s}$  respectively. For the two other inclinations the iso-surface areas were almost the same as for the  $90^\circ$ . All cases displayed similar physical behaviour, with a boundary layer growth on the surface of the bell-mouth and at the duct. Vortex structures were created at the duct sides, as a result of the design of the bell-mouth, which was shortened at the sides to fit the rig. These areas generated losses, which are described by the loss coefficients.

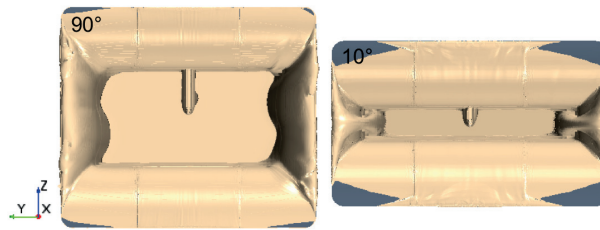


Figure 4.30: Iso-surfaces of total pressure equal to the entrance total pressure for the  $19\text{mm}$  heat exchanger at the highest tested mass airflow rate.

In the velocity plot, in figure 4.29, it can also be seen that the airflow just in front of the core did not seem to be affected by the angling of the heat exchanger, when no outlet duct was present. Previous research has shown that the flow-field over the core was affected by the angling, resulting in a more variable flow for a more inclined arrangement [41]. Close examination at the core showed that the airflow was almost parallel to the duct and was re-directed within the core and not within the duct. The definition of the porosity model forced the airflow to be angled within the core. In figure 4.31 a detail view of the velocity vectors on the centreline plane, including the inlet duct and the core, is shown. It can be seen that the re-direction of the airflow occurred within the core and not in front of it.

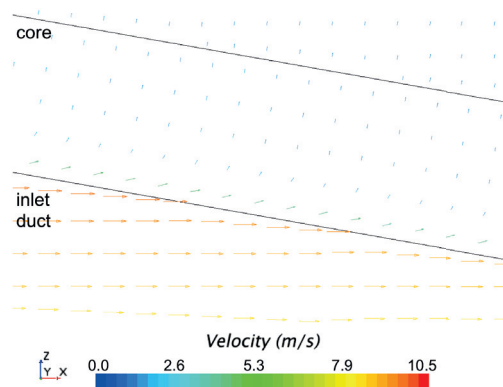


Figure 4.31: Velocity vector at the inlet duct and at the core.

#### 4.4 CFD simulations of one period of a fin

Simulations of one single period of a fin were conducted to evaluate internal flow variations within the heat exchanger core. The chapter is divided into three parts, where: the first represents the results based on the inlet velocity being set to be the same velocity as in the duct for the experiments, where two velocities were simulated; the second part represents a constant velocity in the x-direction at the inlet of the computational domain for one period of a louver, which was independent of the magnitude of the angling; and the final section handles the thermal effects from simulations of a period of a fin.

Simulations were also carried out for two different internal geometries of the core, the original and the modified; where the later was based on the tested heat exchanger design. Smaller variations were seen for the airflow characteristics and the static pressure drop varied up to 3.3% for the 19mm thick heat exchanger and 5.3% for the 52mm thick heat exchanger. Results regarding internal design variation are further evaluated in Appendix D.

##### 4.4.1 Constant mass airflow rate

The results showed that the flow-field within the core was greatly affected by the entrance angle and direction. In figure 4.32 the velocity plots for the four angled heat exchanger are shown on the centreline plane for the 19mm thick heat exchanger, where the air entered from above, parallel to the louvre angle. Generally, a decreased velocity through the core was seen and a more detached airflow at the entrance, for a more inclined heat exchanger.

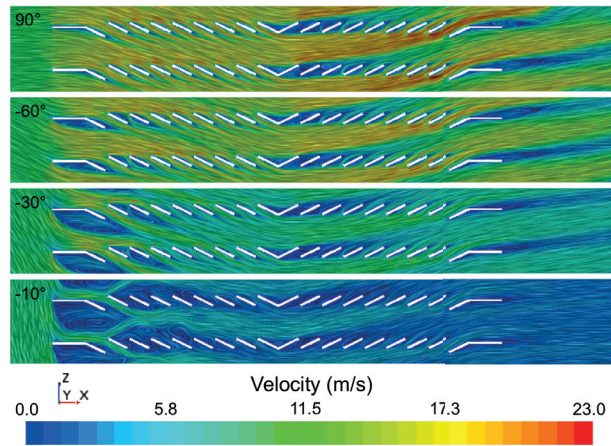


Figure 4.32: Velocity plot, where air entered non-parallel to the louver angle, for the 19mm heat exchanger.

For these simulations the mass airflow rate as well as the velocity magnitude at the inlet duct were constant for the different angles. As can be seen in

the picture, the dynamic pressure for the  $90^\circ$  arrangement was not lost at the entrance, which was also seen for the loss coefficients of the experimental set-up, defined in Chapter 4.1. The airflow accelerated within the core due to area contraction. At the mid-point, where the louvers changed direction, detached regions were created. For a more angled arrangement a larger loss in dynamic pressure was seen at the entrance. The difference in velocity in the x-direction at the in- and outlet was insignificantly affected, meaning that the dynamic loss at the entrance was mainly due to losses originated from the z-component. This was observed for all inclinations of the heat exchangers.

By plotting the turbulent kinetic energy,  $k$ , areas where turbulence was created can be visualised. To find areas where the turbulence was dissipated, the turbulent dissipation,  $\varepsilon$ , can be plotted. In figure 4.33 these parameters are plotted for the  $19\text{mm}$  heat exchanger at  $90^\circ$  and  $30^\circ$  angle, for the highest simulated velocity. It can be seen that turbulence was created and dissipated at the entrance of the core for the  $30^\circ$  inclination and behind the core for the  $90^\circ$  heat exchanger.

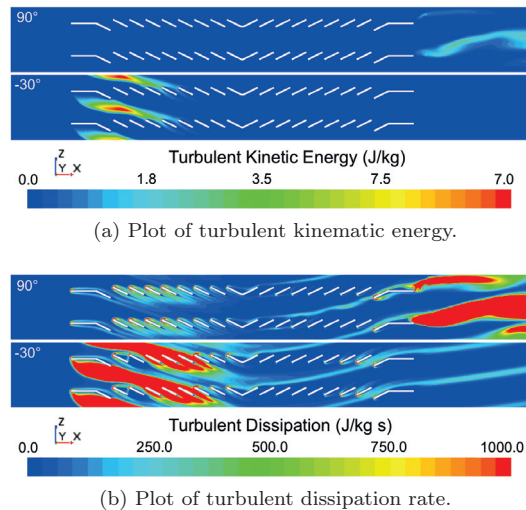


Figure 4.33: Plots of the  $19\text{mm}$  heat exchanger in an angle of  $90^\circ$  and  $30^\circ$ , for the highest simulated mass airflow rate.

Some of the preceding work based on simulations carried out for one period of a fin were defined as laminar. For perpendicular arrangement this assumption is satisfying, at least for the tested Reynolds numbers. For the angled arrangements turbulence was created at the entrance to the core, which is one of the reasons for applying a turbulence model to the solver.

To clarify the flow phenomena, the total pressure, static pressure, and the velocity, is plotted for the  $19\text{mm}$  heat exchanger for angles of  $90^\circ$  and  $30^\circ$ , in figure 4.34. Note, that the scales are not the same for the two cases. It can be seen that the total pressure and static pressure were lost along the core. Behind the

core some of the dynamic pressure was recovered into static pressure, which can be seen in the middle pictures, behind the core. When the airflow was angled relative the core the stagnation position was moved to the upper side of the fin, which can be seen for the 30° arrangement. For the perpendicular arrangement the stagnation position is located at the front edge of the fin.

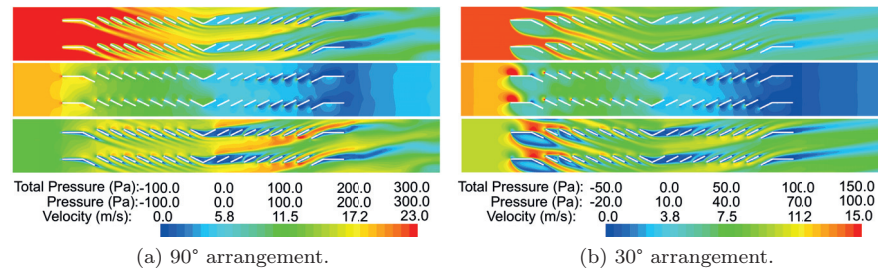


Figure 4.34: Total pressure, static pressure and velocity for the 19mm symmetric louvered heat exchanger.

### Heat exchanger orientation

To find the most optimal position of a heat exchanger in angled condition, both crossflow and downflow orientation, as well as having the downflow arrangement mounted in both an upward and downward direction, resulting in an inverse of the louver angle, were tested. The inlet direction of the airflow affected the flow-field characteristics, which can be seen in figure 4.35 where the velocity is plotted when the air entered from below, defined as the positive direction. The flow-field was fairly similar to when the air entered from above, except at the entrance where the airflow was greatly affected. Even though the flow-field was affected the static pressure drop through the core was almost in-line for the same inclination arrangement.

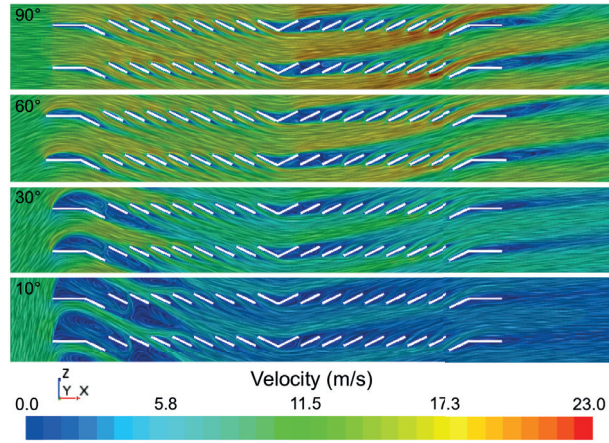
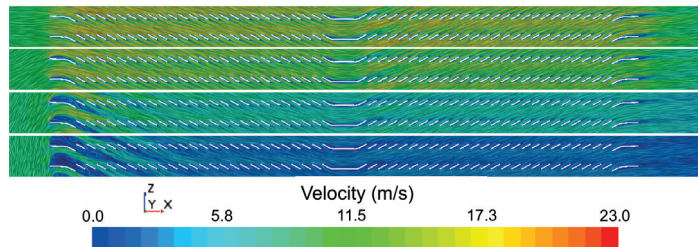
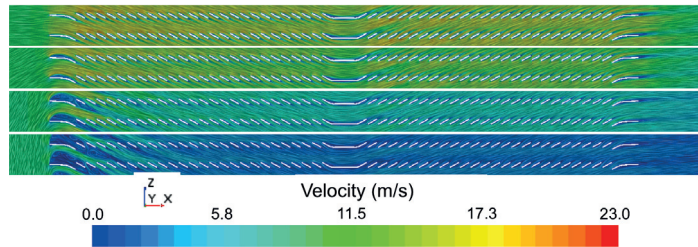


Figure 4.35: Velocity magnitude plot, where air entered parallel to the louver angle, for the 19mm heat exchanger.

Similar flow phenomena were observed for the 52mm heat exchanger, where the results are plotted in figure 4.36. The detached flow-fields at the entrance were similar to the 19mm heat exchanger. At the mid-point, where the louvers changed direction, the flow-field was improved, as can be seen by the decreased low speed areas. In these areas the thermal exchange between the air close to and further away from the surface was increased, as a consequence of more mixing of the air.



(a) Airflow entered non-parallel to the louver angle.



(b) Airflow entered parallel to the louver angle.

Figure 4.36: Velocity plots for the 52mm heat exchanger, for two entrance directions.

From the experimental results it was seen that the overall heat transfer coefficient,  $K$ , was a bit lowered for a more inclined arrangement, see figure 4.19. The thermal efficiency was therefore decreased for these arrangements, one explanation could be the increased detached areas at the entrance, seen in for example figure 4.32: these areas decreased the thermal exchange between the fin and the air.

Additional simulations for the  $19\text{mm}$  thick heat exchanger were conducted in the crossflow orientation, where the airflow entered from the  $yx$ -direction for the different angles. The velocity distribution at the horizontal plane is shown in figure 4.37. The wake at the entrance was located at the leeward side of the tube, which increased in size for a more inclined arrangement. For the crossflow-oriented heat exchangers the velocity plot on the centreline was similar as for the downflow arrangement.

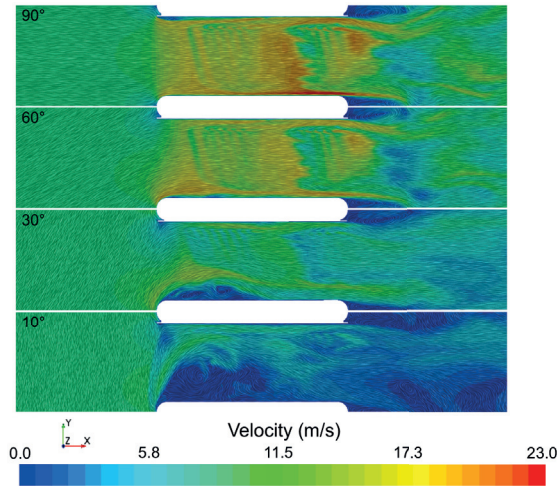


Figure 4.37: Velocity plot at the horizontal plane for the crossflow-oriented  $19\text{mm}$  heat exchanger, with symmetric louvered fins.

To investigate whether the pressure drop increased gradually for increasing inclination angle, simulations were conducted for angles between  $10^\circ$  to  $90^\circ$ , at increments of  $5^\circ$ . These simulations were carried out for the symmetric louvered finned heat exchangers at two additional velocities,  $3.87\text{m/s}$  and  $9.83\text{m/s}$ , which entered parallel to the louver angle. The results showed that the static pressure drop trend was independent of the thickness of the heat exchanger, seen in figure 4.38. The static pressure drop for the  $19\text{mm}$  heat exchanger was  $33 - 36\%$  of that for the  $52\text{mm}$  heat exchanger, for both inlet velocities. From the graph it can be seen that the curves were steeper for heat exchangers inclined more than  $65^\circ$ , resulting in a higher relative loss. Less inclined arrangements resulted in a lower relative loss. For the  $52\text{mm}$  heat exchanger the pressure drop difference for inclinations from  $65^\circ$  to  $90^\circ$  was  $100\text{Pa}$  for the thicker heat exchanger at the higher simulated velocity. For angles greater than  $65^\circ$ , a pressure loss of  $100\text{Pa}$  occurred for every second simulated angle.

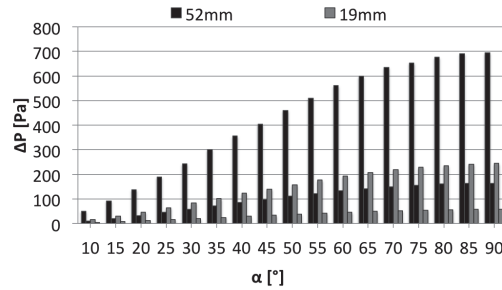
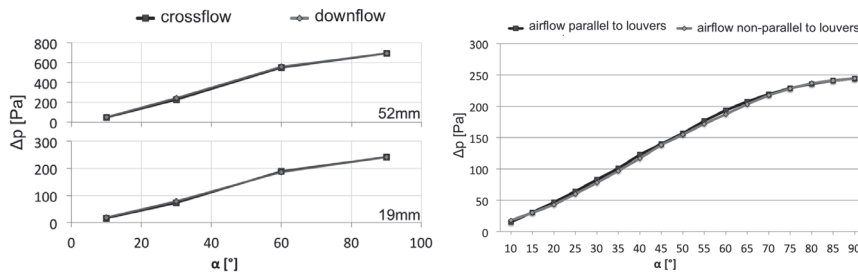


Figure 4.38: Static pressure drop as a function of inclination angle for the symmetric louvered finned heat exchangers.

From the experiments it was seen that the downflow-oriented heat exchangers gave a lower pressure drop compared to the crossflow orientations. From these simulations the pressure drop was almost identical for the downflow compared to the crossflow orientations, which can be seen in figure 4.39a. An earlier study, carried out by [39], showed the opposite results; a reduced pressure drop for crossflow compared to downflow orientated heat exchangers. The explanation of this result was that the airflow could enter the core more gradually. This investigation was carried out during the 1940's, and it is hard to determine the internal design of the heat exchangers the results were based on.

Figure 4.39b shows the pressure drop when the airflow entered parallel, and non-parallel, to the louver angle, for the 19mm heat exchanger. Even though the airflow characteristics were greatly affected by the entrance direction the pressure drop remained constant.



(a) Pressure drop for the downflow and crossflow (b) Pressure drop for the fin with the airflow entered parallel and non-parallel to the louver angle.

Figure 4.39: Static pressure drop for different orientations of the heat exchangers and airflow entrance directions.

For the heat exchanger with the louvers in one direction the flow-field at the entrance was fairly similar to the symmetric louvered finned heat exchangers. Since the louvers had the same angle throughout the fin the midway flow-field

followed the same angle, and smaller separated areas were seen, figure 4.40. The pressure drop trend for the asymmetric  $19\text{mm}$  heat exchanger was similar to the results for the symmetric geometry as well. As was obtained from the experiments, slightly higher static pressure values were seen with the louvers in one direction.

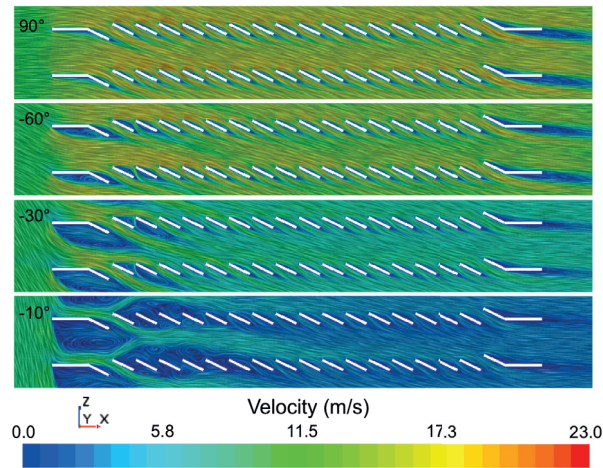


Figure 4.40: Velocity plot for the  $19\text{mm}$  heat exchanger with asymmetric louvered fin, where the airflow entered parallel to the fin.

### Outlet airflow angle

From the results it was seen that the angle, and the direction of the outlet airflow, was independent of the entrance direction. Kim et al. [40] suggest that the airflow direction at the exit of the core was dependent on the inlet direction and was the same for a symmetric louvered finned heat exchanger. Figure 4.32 and 4.35 shows that the outlet angle of the airflow had the same direction as the louver angle at the outlet, and not as the entrance direction of the airflow. Hence, the outlet angle was not dependent on the direction of the entrance airflow into the core, which was suggested by preceding work. It was also seen that the flat section at the outlet of the fin straightened the flow-field into the longitudinal direction. The outlet angle was calculated by taking the mass airflow averaged velocity in x-, y- and z-direction for a number of yz-planes downstream of the core. The outlet airflow angle was decreased for a lower core velocity, since the flow-field was more “louver-directed” for higher Reynolds numbers. For lower Reynolds numbers the airflow was travelling straighter through the core, “array-directed”. This flow phenomena was stated by for example Yuan et al. [27], and confirmed in figure 4.41, where streamlines show the airflow direction at two Reynolds numbers. As a consequence of this, it is important to consider which orientation the heat exchanger should be mounted in a vehicle installation to reduce losses due to the surrounding environment.

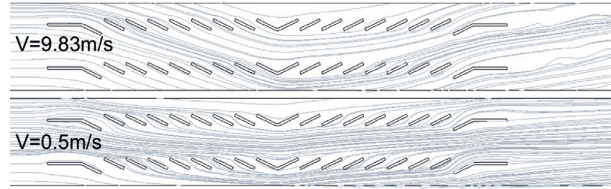


Figure 4.41: “Louver-directed” and “array-directed” flow-field for various Reynolds numbers.

### Dynamic pressure recovery at the exit of the core

It was seen that some of the dynamic energy in the flow within the core was recovered into static pressure, due to the tube design and the flow interactions. In figure 4.42 detail pictures of the outlet core at the horizontal plane are shown with velocity and static pressure plotted, for the  $19\text{mm}$  thick heat exchanger, with an inlet velocity of  $9.83\text{m/s}$ . In the velocity plot the wakes behind the tubes can be seen, with an accelerated airflow attached to it. Diffusion of the flow-field occurred at the outlet. It was also seen that there was a transient behaviour of the flow, and the described effect was stronger on the side of the tube where the distance to the fin was shorter. In the static pressure plot a negative pressure area located at the very back of the fin is visible. The negative pressure zone was moved downstream for higher, and upstream for lower, air velocities. For the highest mass airflow rate for the  $90^\circ$  arrangement the zone reached approximately  $7d_h$  behind the core. The static pressure was defined as atmospheric at the outlet of the computational domain, whereas the pressure was recovered at the outlet. It should be mentioned that the airflow acted in all three dimensions, even though  $2D$  planes are shown.

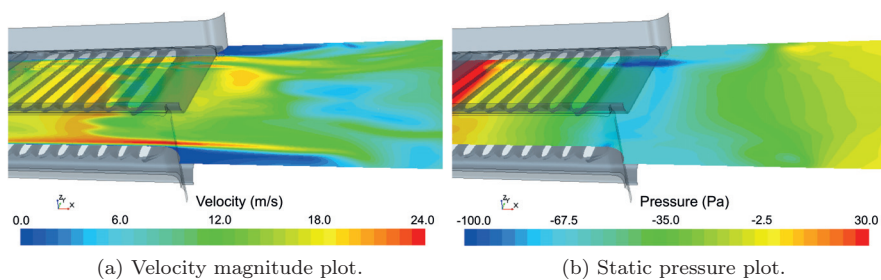


Figure 4.42: Plots of velocity and pressure at the exit of the core.

Pressure recovery was determined from the simulations of one period of a fin. From classical theory the loss coefficient due to sudden expansion can be found for different geometries, for example in [38]. For a high area ratio, larger separated areas are created generating a higher loss factor, whereas for a smaller

diameter ratio the loss factor approaches zero. To calculate the expansion loss this factor is multiplied by the dynamic pressure, based on the velocity in the smaller pipe. In figure 4.43 loss coefficients,  $\xi$ , are presented for various outlet geometries. The first scenario had a loss coefficient equal to 1 since the distance to the walls at the expansion was infinite. For the second and third scenarios the distance relation was 0.75, which was the proportions of the fin and tube geometry used in this study. When walls are present at the exit the loss coefficient would correspond to approximately  $\xi \approx 0.18$  [38]. For this investigation no walls were present at the outlet. Instead the outlet airflow from each side of the tubes acted as diffusion in the flow-field at the symmetry plane. The loss coefficient for this scenario should therefore be between 0.18 and 1. By analysing the CFD results, where the averaged values of the air velocity and the pressure were recorded at a  $yz$ -plane just before the expansion of the tubes, the loss coefficient was derived for this specific case. It was found to be  $\xi \approx 0.36$ .

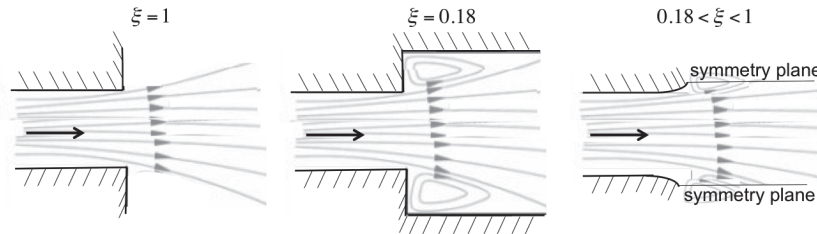


Figure 4.43: Loss coefficients due to expansion of flow-field.

### Correlation with experiments

Compared to experimental data the pressure drop from CFD of one period of a fin was over-predicted. In figure 4.44 the data is presented and it will be seen that the CFD results followed the same trend as the experimental data. Better correlation was achieved for the 19mm thick heat exchanger, with a maximum deviation of 9% at the highest tested airflow rate. An over-prediction of 10% for pressure drop and heat transfer rate from CFD relative to experimental results was also obtained by Yuan et al. [27] for a similar study, regarding perpendicular airflows. The relatively good correlation validates the simulation model of a period of a fin.

A perfect correlation was not expected, since there were a number of factors that were not identical for the two methods. For example the experiments were carried out for heat exchangers with a size of  $888mm \times 888mm$ , which were mounted with an upstream duct. The simulations of one period of a fin, with boundaries defined as periodicity, did not experience any effects at the core edges, as was the case for the experiments. Another reason for the deviation could be that the geometries of the simulated louvered fins were not completely identical to the one used for the experiments.

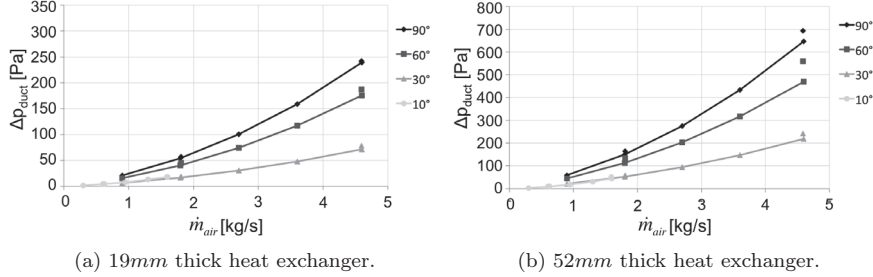


Figure 4.44: Comparison between experiments and CFD simulations of one period of a fin.

#### 4.4.2 Constant velocity in the x-direction

A reason for carrying out these simulations was that the results obtained from the experiments, showed a constant static pressure drop over the core, independent of the magnitude of inclination. A detailed insight can be provided by simulations of this kind. To obtain a constant velocity of the air through the core, the velocity in the x-direction at the inlet was defined as constant for all inclinations. The correct angle of the airflow, relative to the heat exchanger core was obtained by varying the z-component.

Two velocities were simulated as constants in the longitudinal direction, for the four inclinations:  $1\text{m/s}$  and  $4.92\text{m/s}$ . Unstable solutions were seen for  $10^\circ$ , a reason could be the high magnitude of the velocity in the vertical direction. In figure 4.45 the velocity magnitude is presented on the centreline plane for the higher defined velocity. It can be seen that the velocity magnitude was higher in front of the core for a more inclined heat exchanger since the velocity component in the z-direction was increased. It was previously defined that an increased angle of the heat exchanger generated a higher loss in dynamic pressure, which can also be seen in figure 4.45. The large separated area at the entrance limited the area available for air to entry, thus accelerating the airflow. Therefore, a large velocity gradient was obtained at the entrance, for the  $30^\circ$  and the  $10^\circ$  arrangements. At the outlet of the core the velocity plot was similar in magnitude for all inclinations. Hence, the velocity in the z-direction was lost as a consequence of the forced re-direction of the airflow at the entrance. Behind the core the averaged velocity was approximately as in the x-direction at the inlet boundary.

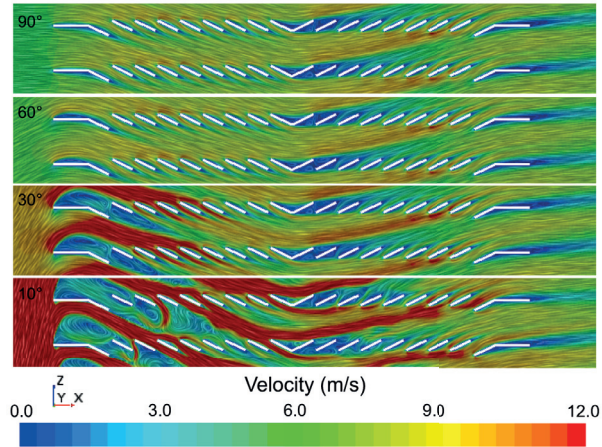


Figure 4.45: Velocity contours for a constant inlet velocity in the x-direction equal to  $4.92\text{m/s}$ .

The static pressure drop was not significantly affected by the inclination angle, seen in figure 4.46 for both velocities. For the  $60^\circ$  arrangements the pressure drop were slightly decreased, while the  $30^\circ$  had approximately the same as the perpendicular arrangement. The pressure drop for the most inclined configuration had a bit higher value. From the experiments similar results were seen for all inclinations.

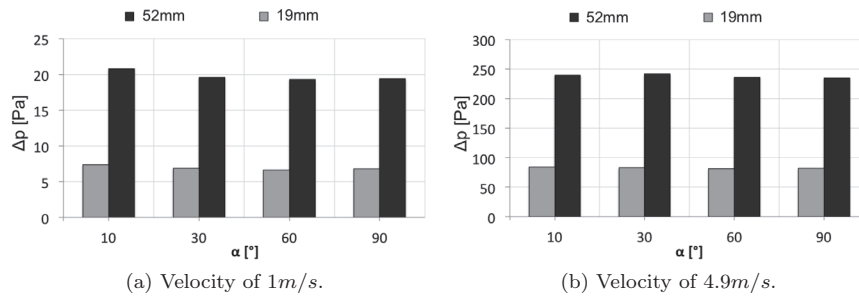


Figure 4.46: Static pressure drop over the core at the two inlet velocities in the x-direction.

Higher variations were seen between the inclinations when plotting the total pressure drop. In figure 4.47 this graph is presented. A slightly increased pressure drop for arrangements up to  $30^\circ$  can be seen. For more inclined heat exchangers the pressure drop increased substantially. These results are in-line with the results from the experiments as well as the results obtained by Nichols [39]. The investigation carried out by Nichols evaluated a higher air velocity,  $5\text{m/s}$ , for a CAC core with a thickness of  $24\text{cm}$ .

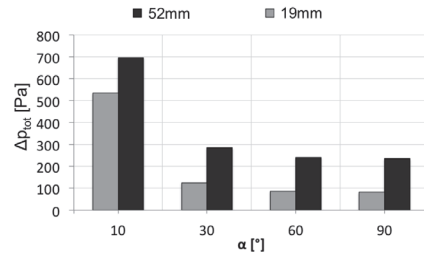
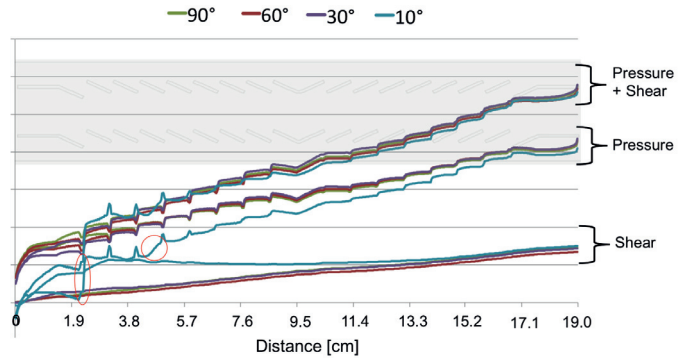


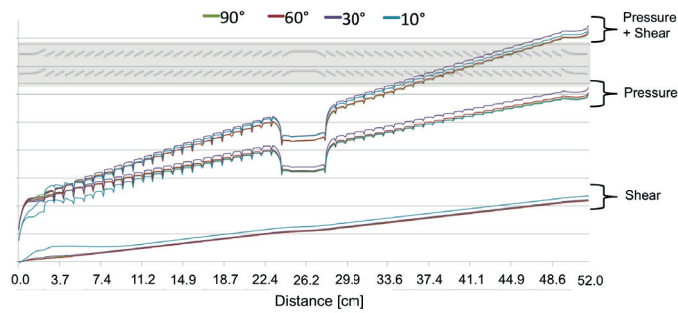
Figure 4.47: Total pressure drop over the core at an inlet velocity of  $4.9m/s$  in the x-direction.

To identify areas affecting the losses along the fin, the accumulated pressure and shear losses can be plotted along the louvered fin, in the x-direction of the core. These parameters are plotted for both heat exchangers with symmetric louvered fins in figure 4.48: the velocity in the x-direction was defined as  $4.92m/s$ . Similar trends were seen for both geometries with a higher pressure than shear loss. For the  $90^\circ$ ,  $60^\circ$  and  $30^\circ$  arrangements the shape of the curves were almost identical, with only a small variation in between. Over the core entrance the pressure loss was increased due to the stagnation. At the flat section, at the inlet, the pressure loss was only slightly increased, whereas at the start of the louvers the losses were increased for each louver. Areas of high pressure can be seen in figure 4.49a at the front face of the louvers. The percentage pressure loss for these arrangements was between 71 – 76% of the total loss. The increase in shear stress was fairly linear along the core.

Exceptions were seen for the  $10^\circ$  arrangement, where the phenomena were dissimilar to the other angles, but similar for the two heat exchanger depths. At the entrance of the core the pressure loss was negative, since the stagnation point was located on the upper surface of the fin, parallel to the horizontal plane. The front edge of the fin was therefore located within a separated region, with a negative pressure, seen in figure 4.49a. In the accumulated plot two areas are highlighted with red circles, showing areas where static pressure increased rapidly. High pressures were created in these areas due to the airflow direction, which can be seen in figure 4.50. From the accumulated plot it can be seen that the losses due to shear effects, for the  $10^\circ$  arrangements, was larger compared to the other angles. Between the separated areas and the accelerating airflow, there was a large velocity gradient. High shear stress was created between these layers, since shear stress is the velocity gradient multiplied by the dynamic viscosity.



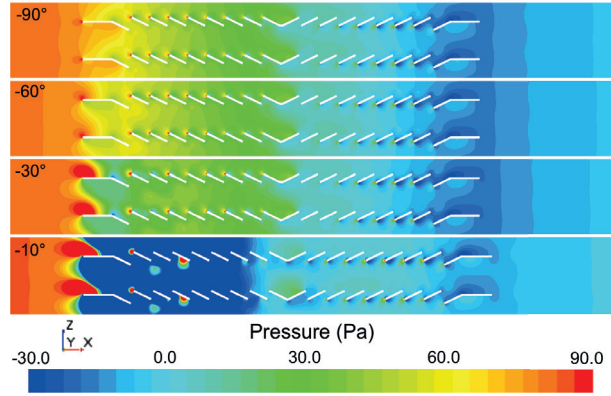
(a) 19mm heat exchanger.



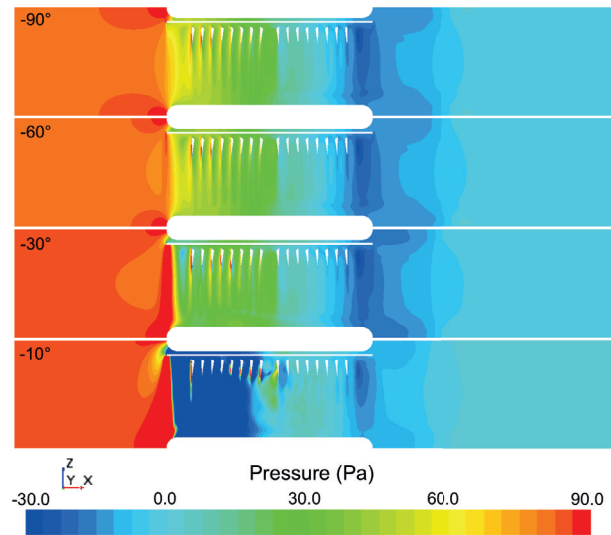
(b) 52mm heat exchanger.

Figure 4.48: Accumulated losses along the louvered fin.

The static pressure is plotted, on the centreline and the horizontal plane, for the 19mm heat exchanger, in figure 4.49a and 4.49b; to support the arguments for the accumulated plot. It should be noted that the range was set between  $-30$  and  $90Pa$ . For the  $10^\circ$  configuration an even lower negative pressure was created. As the airflow inclination angle relative the core was increased the stagnation position moved towards the upper side of the fin, see figure 4.49a. The plot for the  $10^\circ$  arrangement was unlike the others, with a larger negative-pressure area at the first part of the core.



(a) Static pressure on the centreline plane.



(b) Static pressure at the horizontal plane.

Figure 4.49: Pressure drop along the fin, where the air entered parallel to the louver angle.

For the  $10^\circ$  angled configurations, larger separated areas were created at the entrance, seen in figure 4.50. As a consequence of the contraction of the airflow at the entrance high airspeed was created in between the fins and the separated regions. Large velocity gradients were seen in these areas. The static pressure plot in the same figure, shows that there was a large area of negative pressure, which diffused to positive pressure downstream. The recovery of dynamic into static pressure occurred as a result of the fin design and area expansion at the angled louver, which allowed the airflow to expand. This interaction of the surface and flow-field resulted in a recovery of dynamic pressure. The third picture in figure 4.50 shows turbulent viscosity ratio, indicating low magnitudes. Hence, no numerical induced error, due to turbulent model, was suspected to

cause these phenomena. To improve the convergence of the most inclined heat exchanger the mesh resolution and the solver strategy were considered, presented in Appendix E.

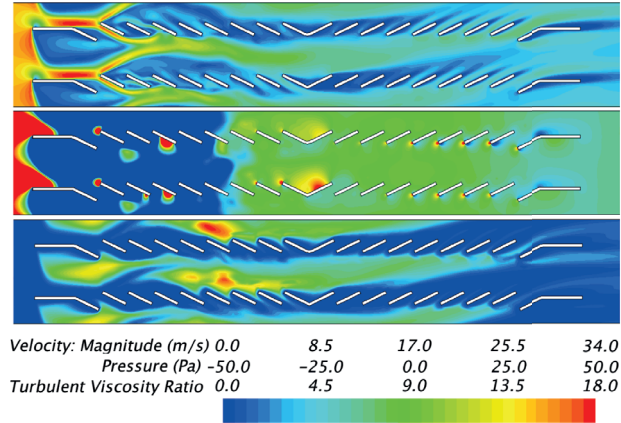


Figure 4.50: Velocity magnitude, static pressure and turbulent viscosity ratio for the  $10^\circ$  configuration.

#### 4.4.3 Thermal simulations

To evaluate the effect of heat transfer as a function of the inclination angle, thermal simulations for the  $19\text{mm}$  thick heat exchanger were performed. In figure 4.51 the temperature distribution on the centreline plane is shown, where the air velocity was defined as  $9.83\text{m/s}$ . The temperature at the tube was set as  $90^\circ\text{C}$ . It can be seen that the temperature of the air was increased at the outlet for a more inclined heat exchanger. The reason being the decreased velocity of the airflow in the core, seen in figure 4.35, which allowed the air to be heated over a longer time period. The heat transfer rate is defined by equation 2.2 and is dependent on the the specific heat of the fluid, the mass flow rate, and the temperature difference of the medium at the entrance and the exit of the heat exchanger. To compare the  $90^\circ$  and  $30^\circ$  inclinations it is important to bear in mind that the size of the core was doubled and the velocity through the core was half for the  $30^\circ$  compared to the  $90^\circ$ . Hence, a constant mass airflow rate through the core. To obtain the same heat transfer rate the temperature difference of the in- and outlet airflow must be the same according to equation 2.2. From the simulations the surface averaged temperature at the outlet was recorded. For the  $90^\circ$  the temperature difference was  $24^\circ\text{C}$ , and  $35^\circ\text{C}$  for the  $30^\circ$  configuration. From these values the heat transfer rate was calculated, which was higher for the angled configurations, as a result of the greater core area.

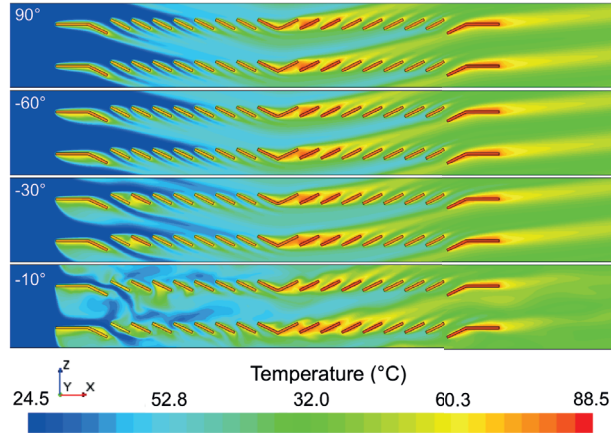


Figure 4.51: Temperature distribution at the solid fin and in the flow-field, for an inlet velocity of  $9.83\text{m/s}$ .

The other method to evaluate heat transfer for angled heat exchangers was by simulating a constant velocity in the x-direction at the entrance, and increasing the velocity magnitude in the z-direction for a more inclined heat exchanger. This method corresponds to having an inlet duct, which varied in height to achieve a constant core area within the duct, for different inclinations. The method enables evaluation of variances in temperature to determine the most efficient angle. In figure 4.52 the temperature distribution is plotted for this set-up. It can be seen that the plots were almost identical between the different inclinations after the mid-point, based on magnitudes and behaviour. Again, the heat transfer rates could be calculated by using equation 2.2. For this set-up the mass airflow was constant for the different inclinations as well. Although, for a more inclined heat exchanger the velocity in the entrance duct must be increased to obtain the same mass airflow rate for the varying inclinations. The temperature difference in front of, and behind, the core was  $42^\circ\text{C}$  for the  $90^\circ$ ; and  $35^\circ\text{C}$  for the  $30^\circ$  angled heat exchanger. Therefore, the heat transfer rate was higher for the  $90^\circ$  configuration.

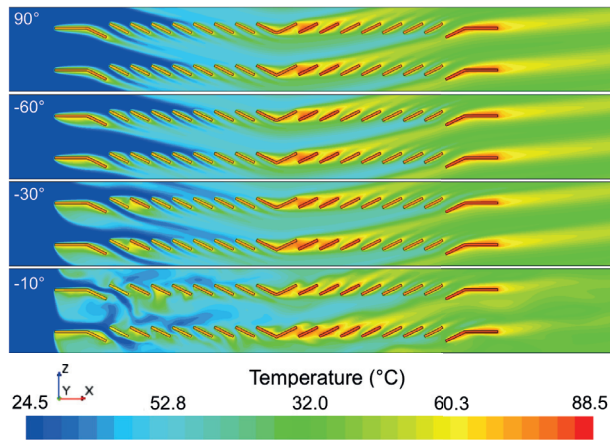


Figure 4.52: Temperature distribution at the solid fin and in the flow-field, for a constant velocity in the x-direction of  $4.92\text{m/s}$ .

#### 4.5 Confirmation of airflow distribution

From the Ruijsink microprobe system the airflow distribution at the face of the core was obtained. The microprobe equipped heat exchanger was tested at  $30^\circ$  angle, both with and without the outlet duct. The airflow distribution for the two tests is plotted in figure 4.53, confirming that the outlet duct had a negative influence on the airflow uniformity. Nichols [39] showed that the airflow was fairly uniform up to an angle of  $30^\circ$ , by carrying out a tuft survey. For more inclined heat exchangers the tuft survey indicated a more irregular velocity distribution, due to the sharp angle between the duct and the core.

From CFD simulations of the test set-up it was seen that the airflow was fairly uniform for both the  $30^\circ$  and the  $10^\circ$  configuration without a downstream duct, at the highest airflow rate. For the  $10^\circ$  arrangement the velocity was decreased slightly at the lower part of the core. For all arrangements lower velocities were seen at the edges of the core, due to the boundary layer at the duct.

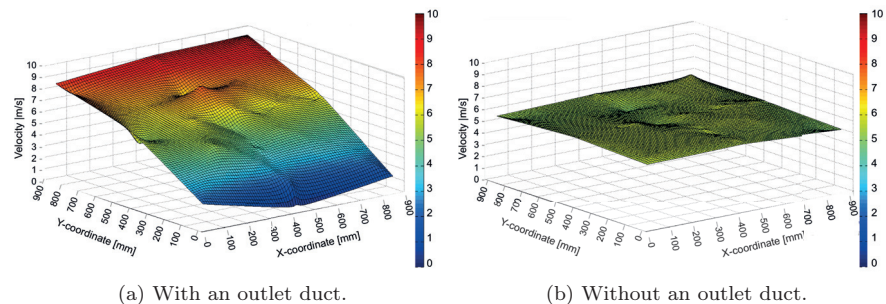


Figure 4.53: Airflow distribution over the heat exchanger core.

High airflow uniformity is desirable [56], in order to obtain a higher heat transfer rate between the surrounding air and the medium within the core. If the air velocity through the core was  $0.8m/s$  in one half and  $1.2m/s$  in the other, the heat transfer rate would be lower compared to a velocity of  $1.0m/s$  over the whole surface. A uniform airflow is more important for a CAC than for a radiator since the charge air usually has a higher temperature than the coolant.

A comparison of the velocity on the centreline, in the vertical direction of the core, was carried out for the results from the CFD simulations and from the microprobes. In figure 4.54 the results are plotted for the scenarios with and without the outlet duct. Similar trends were seen for both scenarios. When the outlet duct was present the results were more similar, whereas without the duct a relatively constant offset of the velocity for the two methods was seen.

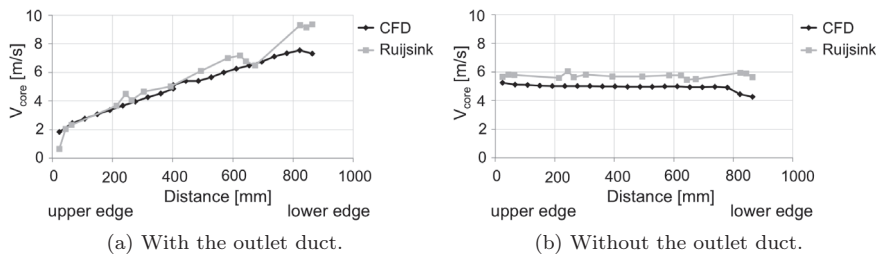


Figure 4.54: Comparison of velocity on the centreline in the vertical direction, in the core.

## 4.6 Final remarks

From this work some final remarks regarding implementations to further decrease total pressure losses, as well as consequences of increased core size for angled installations are discussed.

### 4.6.1 Ideas to decrease the static pressure drop

To decrease the static pressure drop over the angled heat exchangers the entrance loss must be reduced. This could be achieved by the use of guiding vanes in front of the core. The airflow will then be angled before it reaches the heat exchanger core without the great loss seen in this investigation, if designed appropriately. Vanes could also be installed behind the core to reduce losses at the exit. These could play an important role for reducing pressure losses, when installing angled heat exchangers in a vehicle. Turning vanes have been evaluated by for example [41]. From these investigations it was shown that it is hard to implement turning vanes that work properly, and not create, instead of decreasing losses.

Another solution could be to re-design the core of the heat exchanger. If the fins had been angled relative the heat exchanger, similar to the heat exchanger angle relative to the airflow, resulting in a parallel flow of the air compared to the duct, pressure drop would have been improved as well as heat transfer. The limitation of this design is the manufacturing procedure. Currently, there is no technique for manufacturing this kind of heat exchanger in serial production, which is the reason for not including such heat exchanger designs in this study.

#### 4.6.2 Consequences of increased size of the heat exchanger

By angling the heat exchanger an increased size of the component is possible. Therefore it is important to bear in mind that an increased size of a heat exchanger will also increase the weight of the component itself, as well as the increased volume of the cooling medium. For the  $52\text{mm}$  thick heat exchanger the weight of the fin and the tubes is  $14\text{kg}/\text{m}^2$ , and  $5\text{kg}/\text{each}$  for the side beams, per length of  $1000\text{mm}$ . For a heavy truck with a  $16\text{l}$  engine, and retarder, the amount of coolant is up to  $75\text{l}$ . Within the tubes there is approximately  $6\text{l}$ , for a core size of  $888\text{mm} \times 1000\text{mm}$ . If the heat exchanger is mounted with a downflow orientation the size of the tanks would be constant, independent on the heat exchanger angle. Installing a heat exchanger in a crossflow orientation will extend the length of the tanks in an angled position, which will increase the weight.

Compare a  $52\text{mm}$  thick heat exchanger at  $30^\circ$  compared to  $90^\circ$ ; with a doubled core area for the angled installation. If assuming downflow condition the additional weight for the angled installation would be due to the increased size of the core, the beams, and due to the increased coolant volume. Assume a core area for the perpendicular case of  $0.444 * 1.0 = 0.444\text{m}^2$ , with the tanks on the longer edge. For the  $30^\circ$  installation, with the doubled core area the increased weight would be:  $6.2\text{kg}$  for the core,  $4.4\text{kg}$  for the beams, and  $3\text{kg}$  for the coolant. The resulting additional weight total  $13.6\text{kg}$ . Since the size of the tanks remains the same the additional weight is lower compared to the weight for the  $90^\circ$  installation. This type of weight analysis must be taken into consideration when investigating angled heat exchangers and the requirement of increased heat transfer rate.

---

## 5 Conclusions

The simple answer to the question “What is the most efficient heat exchanger thickness and angle relative to the airflow?”: is that there is no general formula to answer such a question. It is the application and the specific usage of the component that affect the operating conditions of the heat exchanger, which will affect the design of the installation. This thesis explains the dynamics and performance of heat exchangers in inclined airflows. If a specific installation is going to be evaluated the information presented in this thesis is of great importance and could be used to find an optimal design for the specific application.

In this thesis different dimensioning criteria for heat exchangers have been defined, to be able to perform a comparative study of heat exchanger thickness and angle. Several cases have been evaluated to predict this type of information and to present the usage of the results.

It has been shown that the static pressure drop through the core was insensitive to the heat exchanger inclination angle, for a constant air velocity in the core. The airflow characteristic was greatly affected for a more inclined heat exchanger, with a detached area at the entrance of the core. The results indicated that the angling of the heat exchanger only affected the dynamic pressure where a larger loss was seen at the core entrance for a more inclined heat exchanger. Therefore, the airflow due to the forward motion of the vehicle, will be sufficient for longer before the fan has to start to operate for a perpendicular, instead of an angled, installed heat exchanger. For a constant mass airflow rate through the system the pressure loss was decreased for the angled installations, due to the decreased airspeed through the core.

It has been shown that the heat transfer rate was increased for an increased inclination angle, for a constant mass airflow rate. The explanation being that the increased core area subjected to the incoming airflow, as well as the decreased velocity of the air through the core. This increased the temperature difference of the air at the entrance and exit of the core, which consequently increased the heat transfer rate. For an unchanged core area and air speed through the core, the heat transfer rate was approximately constant; where the less inclined arrangements functioned more thermally efficient.

Another experience from the experiments and the simulations was the knowledge of the significant impact the surrounding geometry had on the pressure losses. This is important to bear in mind when designing an installation for a vehicle application; to minimize unnecessary pressure losses within the system. In this thesis the flow-field effect at the core outlet has been documented, where it was shown that the outlet angle relative to the core was independent on the airflow entrance angle. The surrounding geometry behind the heat exchanger should have the same direction as the louver angle at the outlet. Ensuring a uniform

airflow through the core and decreasing losses of the geometrical design in front of the heat exchanger, is as important as behind it. It has been shown that the airflow was uniform when the heat exchanger was mounted at  $30^\circ$ , if no duct was placed behind it. A uniform flow is advantageous for heat transfer efficiency.

A method has been developed to simulate angled heat exchangers with information from component tests from the perpendicular arrangement. It has been shown that for the investigated heat exchangers, an angled radiator in a vehicle installation can be simulated in CFD with the porosity coefficients defined from the perpendicular arrangement. The deviation between tests and corresponding CFD simulations, where the porosity coefficients were derived for  $90^\circ$  installation, were at the most 9%. This method could be used to obtain an indication of the performance of an angled heat exchanger relative to the airflow. Consequently, it would not be necessary to test the component in angled condition to derive the porosity coefficients that would later be used for simulations.

---

## 6 Summary of papers

### Paper I

#### **CFD Method and Simulations on a Section of a Detailed Multi-Louvered Fin where the Incoming Air is Directed at 90° and 30° Relative to the Compact Heat-Exchanger**

*Presented at SAE Commercial Vehicle Engineering Congress 2013, Chicago.*

This article presented a method to simulate a single period of a louvered fin, of a crossflow heat exchanger for automotive application. Two inclination angles of a heat exchanger, relative the incoming airflow, were evaluated by using CFD. The developed method was based on pressure drop and flow-field characteristics, where the recommendation was made that those types of simulations could be defined as steady state, and with the *SST k $\omega$*  turbulence model. The static pressure drop was reduced significantly for the  $\pm 30^\circ$  compared to the perpendicular arrangement,  $90^\circ$ , to approximately one third, when comparing for the same mass airflow rates. Since the test section area was defined as constant the velocity through the heat-exchanger core varied for the  $90^\circ$  and the  $30^\circ$  cases. When comparing a constant core velocity, minor pressure losses were observed due to the forced re-direction of the airflow for the  $30^\circ$  angle compared to the  $90^\circ$  case. Even though small variations were seen in pressure drop, the flow-field was greatly affected by the entrance direction of the airflow relative to the core.

### Paper II

#### **CFD Simulation and Experimental Investigation of Pressure-Drop through 90° and 30° Angled Compact Heat-Exchangers Relative to the Incoming Airflow**

*Presented at VTMS11 2013, Coventry.*

The paper presented a study based on experiments, and simulations of the experimental set-up, for two inclination angles of the heat exchanger relative to the airflow. Both pressure drop, and heat transfer rates, were presented from the experiments. A method was generated to simulate angled heat exchangers, where a relatively good correlation was achieved to get an indication of the heat exchanger performance. This study also highlighted the importance of the shape of the surrounding geometries to the heat exchanger installation. When an outlet duct was placed behind the angled heat exchanger a substantial increase in pressure loss was seen.

## Paper III

**Experimental Investigation of Heat Transfer Rates and Pressure Drops through Compact Heat Exchangers**

*Published in International Journal of Automotive Engineering 6, pp. 7-14, 2015.*

The two previous papers focused on two inclination angles of the heat exchanger relative to the incoming airflow. This article presented a detailed investigation of four inclination angles for two heat exchanger designs, with symmetric louvered fins. The heat exchangers were mounted such that the tubes within the core of the heat exchanger, where the coolant flowed, were parallel to the vertical plane. This scenario was mentioned as the downflow orientation, where the heat exchanger later was angled downwards. Each heat exchanger was mounted in a duct, where it was tested for thermal and isothermal conditions. The inlet temperature of the coolant was defined to two temperatures; ambient temperature and  $90^{\circ}C$ . For the ambient scenarios the coolant had the same temperature as the surrounding air; these tests were performed for five airflow rates. When the coolant had a temperature of  $90^{\circ}C$ , a combination of five coolant flow rates and the five airflow rates were tested. Both pressure drop and heat transfer rates obtained from experimental data, were investigated for the different inclinations. The main results from this investigation showed that a more inclined heat exchanger resulted in lower static pressure drop and at the same time achieved a higher heat transfer rate, for a specific mass airflow rate through the core. When analysing the parameters at the same core speed it was seen that the static pressure drop was independent to the inclination angle.

## Paper IV

**Experimental Investigation of Heat Transfer Rate and Pressure Drop through Angled Compact Heat Exchangers Relative to the Incoming Airflow**

*Published in SAE International Journal of Commercial Vehicles 7 (2), pp. 448-457, 2014.*

This article was a continuation of Paper III, which was extended to include the heat exchangers arranged in a crossflow orientation. For this scenario the tubes were parallel to the horizontal plane and thereafter angled downward. An additional heat exchanger was included in the study, which was specially made with the louvers in only one direction throughout the core. As for the previous paper both isothermal and thermal conditions were studied, based on experimental results. It was seen that neither pressure drop, nor heat transfer rate, was affected by the orientation of the heat exchanger, with the tubes parallel to the horizontal or the vertical plane. Rather small variations were observed for the two scenarios. A comparison of heat exchanger thickness and angle was carried out, where the static pressure drop was defined as  $200Pa$  over

---

the heat exchanger. It was seen that either a  $19mm$  thick heat exchanger at  $60^\circ$  or a  $52mm$  heat exchanger at  $90^\circ$  could be used to obtain the same heat transfer rate.

#### Paper V

#### **CFD Simulations of one Period of a Louvered Fin where the Airflow is Inclined Relative to the Heat Exchanger**

*To be published in SAE International Journal of Engines 8 (4), 2015.*

This paper continued the study from Paper I, where the derived CFD method was applied to simulate various inclination angles of the airflow relative to the core, for a period of a fin. All three heat exchangers were simulated where the airflow entered both from above and below, relative to the horizontal plane. Simulations were also carried out where the airflow entered from the side, representing the heat exchanger to be angled relative to the vertical axis. Pressure drop and heat transfer rates, as well as flow-field characteristics, were studied in detailed. The pressure drop over the core was not significantly affected by the direction of the entering airflow, even though large separated areas were created at the entrance of the core for a more inclined arrangement. The results were correlated with experimental data and it was observed that the pressure drop followed the same trend as the experimental data, even though the values were over-predicted.



---

## References

- [1] <http://www.ideiasustentavel.com.br/pdf/file51139.pdf>, December 2014.
- [2] Boundy R.G. Davis S.C. Diegel S.W. <http://cta.ornl.gov/data/teadb30/>. Transportation Energy Data Book 30th Edition, September 2011.
- [3] <http://www.erdoel-vereinigung.ch/UserContent/Shop/2010%20The%20Outlook%20for%20Energy.pdf>, November 2014.
- [4] <http://epp.eurostat.ec.europa.eu/tgm/table.do?tab=table&init=1&plugin=1&language=en&pcode=tsdpc320>, September 2014.
- [5] David S.C. Diegel S.W. Boundy R.G. *Transportation energy data book*. 33rd Edition, 2014.
- [6] <http://www.epa.gov/otaq/climate/documents/420f13033a.pdf>, September 2014.
- [7] Stanton D.W. *Systematic Development of Highly Efficient and Clean Engines to Meet Future Commercial Vehicle Greenhouse Gas Regulations*. SAE Paper 2013-01-2421, 2013.
- [8] Gullberg P. *Optimization of the Flow Process in Engine Bays - 3D Fan Modelling Strategies*. Licentiate Thesis, ISSN 1652-8565, Chalmers University of Technology, Sweden, 2009.
- [9] Wamei L. Sundén B. *A Review of Cooling System in Electric/Hybrid Vehicles*. ASME Paper IMECE2010-37636, 2010.
- [10] Tafti D.K. Zhang X. *Geometry Effects on Flow Transition in Multilouvered Fins - Onset, Propagation, and Characteristic Frequencies*. International Journal of Heat and Mass Transfer 44, pp. 4195-4210, 2001.
- [11] Sahnoun A. Webb R.L. *Prediction of Heat Transfer and Friction for the Louvered Fin Geometry*. Journal of Heat Transfer 114, pp. 893-900, 1992.
- [12] Chang Y. Wang C. *Air Side Performance of Brazed Aluminium Heat Exchangers*. Journal of Enhanced Heat Transfer 3, pp. 15-28, 1996.
- [13] Leong K.Y. Saidur R. Kazi S.N. Mamun A.H. *Performance investigation of an automotive car radiator operated with nanofluid-based coolants (nanofluid as a coolant in a radiator)*. Journal of Applied Thermal Engineering 30, pp. 2685-2692, 2010.
- [14] Kim K. Choi K. Kim Y. Lee K. Lee K. *Feasibility study on a novel cooling technique using a phase change material in an automotive engine*. Journal of Energy 35, pp. 478-484, 2010.

- 
- [15] Lin W. Sundén B. Yuang J. *A Performance Analysis of Porous Graphite Foam Heat Exchangers in Vehicles*. Journal of Applied Thermal Engineering 50, pp. 1201-1210, 2013.
- [16] Klett J. Ott R. McMillan A. *Heat exchangers for heavy vehicles utilizing high thermal conductivity graphite foams*. SAE Paper 2000-01-2207, 2000.
- [17] Yu Q. Straatman A.G. Thompson B.E. *Carbon-foam finned tubes in air-water heat exchangers*. Journal of Applied Thermal Engineering 26, pp. 131-143, 2006.
- [18] Chang S.I. Goldasteh I. Maaita S. Mathur G. *Numerical Simulation of Fluid Flow and Heat Transfer in Finned Tube Heat Exchanger: Comparison of Two Different Designs*. SAE Paper 2014-01-0650, 2014.
- [19] [http://europa.eu/rapid/press-release\\_IP-13-328\\_en.htm](http://europa.eu/rapid/press-release_IP-13-328_en.htm), December 2014.
- [20] Harsh V. Chinmaya P. Vasilios T. Mihai D. *Analysis of Hybrid Heavy Duty Powertrains for Commercial Vehicles in the Face of Advanced Vehicle and Exhaust Energy Recovery Technologies*. SAE Paper 2014-01-1808, 2014.
- [21] Teng H. Klaver J. Park T. Hunter G. Velde B. *A Rankine Cycle System for Recovering Waste Heat from HD Diesel Engines - WHR System Development*. SAE Paper 2011-01-0311, 2011.
- [22] Arunachalam P.N. Shen M. Tuner M. Tunestal P. Thern M. *Waste Heat Recovery from Multiple Heat Sources in a HD Truck Diesel Engine Using a Rankine Cycle - A Theoretical Evaluation*. SAE Paper 2012-01-1602, 2012.
- [23] Takatoshi F. Masaaki N. Koichi M. Kiyohiro S. *A Study of the Rankine Cycle Generating System for A Study of the Rankine Cycle Generating System for Heavy Duty HV Trucks*. SAE Paper 2014-01-0678, 2014.
- [24] <http://www.volvogroup.com>, May 2011.
- [25] Webb R.L. *Advances in air-cooled heat exchanger technology*. Proceedings of the International Conference on Heat Exchangers for Sustainable Development, pp. 677-692, 1998.
- [26] Ha M.Y. Kim K.C. Koak S.H. Kim K.H. Kim K.I. Kang J.K. Park T.Y. *Fluid Flow and Heat Transfer Characteristics in Multi-Louvered Fin Heat Exchanger*. SAE Paper 950115, 1995.
- [27] Yuan Y. Jackson A. Nelson M. *CFD Simulation of Flow and Heat Transfer in Airways*. SAE Paper 2001-01-1712, 2001.
- [28] Kays W.M. London A.L. *Compact Heat Exchangers*. 3rd Edition McGraw-Hill, 1984.
- [29] Kuthada T. Wiedemann J. *Investigations in a Cooling Air Flow System under the Influence of Road Simulation*. SAE Paper 2008-01-0796, 2008.
- [30] Barnard R.H. *Road Vehicle Aerodynamic Design*. 2nd Edition, MechAero Publishing, 2001.

- 
- [31] Larsson L. Wiklund T. Löfdahl L. *Cooling Performance Investigation of a Rear Mounted Cooling Package for Heavy Trucks*. SAE Paper 2011-01-0174, 2011.
- [32] Wong J.Y. *Theory of Ground Vehicles*. 3rd Edition, John Wiley and Sons Inc., 2001.
- [33] Lögberg O. *Turbulent Boundary Layer Separation and Control*. PhD Thesis, ISSN 0348-467X, Royal Institute of Technology, Sweden, 2008.
- [34] Martini H. Bergqvist B. Hjelm L. Löfdahl L. *Influence of Different Truck and Trailer Combinations on the Aerodynamic Drag*. SAE Paper 2011-01-0179, 2011.
- [35] Panton R.L. *Incompressible Flow*. 3rd Edition, John Wiley and Sons, Inc., 2005.
- [36] <http://www.cfd-online.com>, September 2011.
- [37] CD-Adapco. *StarCCM+ Manual, 5.06.010 Edition*.
- [38] White F.M. *Fluid Mechanics*. 5th Edition, McGraw-Hill, New York, 2005.
- [39] Nichols M.R. *Investigation of flow Through an Intercooler set at Various Angles to the Supply Duct*. NACA L-408, 1942.
- [40] Kim M.H. Youn B. Bullard C.W. *Effect of inclination on the Air-side Performance of a Brazed Aluminium Heat Exchanger under Dry and Wet Conditions*. International Journal of Heat and Mass Transfer 44, pp. 4613-4623, 2001.
- [41] Rivers D.A. Poulter J.E. Lamont P.J. *Aerodynamics of inclined radiators on grand prix cars*. Proc. Vehicle Aerodynamics Conference, pp. 13.1-9, 1994.
- [42] Monheit M. Freim J. *Effect of Tube Bank Inclination on the Thermal Hydraulic Performance of Air Cooled Heat Exchangers*. Proceedings 8th International Heat Transfer Conference, pp. 2727-2732, 1986.
- [43] Santer R.M. Gleason M.E. *The Aerodynamic Development of the Probe IV Advanced Concept Vehicle*. SAE Paper 831000, 1983.
- [44] Malvicino C. Mattiello F. Seccardini R. Rostagno M. *Flat Heat Exchangers*. VTMS10, 2011.
- [45] Khaled M. Harambat F. Peerhossaini H. *Underhood Thermal Management: Temperature and Heat Flux Measurements and Physical Analysis*. Journal of Applied Thermal Engineering 30, pp. 590-598, 2010.
- [46] Lin W. Yuang J. Sundén B. *Performance Analysis of a Countercurrent Flow Heat Exchanger Placed on the Truck Compartment Roof*. Journal of Thermal Science and Engineering Applications 4, pp. 041004-1-041004-7, 2012.

- 
- [47] Larsson L. Dahl E. Wiklund T. Löfdahl L. *Yaw- and Trailer Dependence for Rear-Mounted Cooling Installations for Heavy Vehicles*. ASME 2012 Fluids Engineering Summer Meeting, FEDSM2012-72248, 2012.
- [48] Karbach K. *Determination of Air Side Fluid Flow and Heat Transfer Characteristics in Heat Exchangers using CFD*. SAE Paper 971847, 1997.
- [49] Tafti D.K. Wang G. Lin W. *Flow Transition in a Multilouvered Fin Array*. International Journal of Heat and Mass Transfer 43, pp. 901-919, 2000.
- [50] Bouzida S. Mignot C. *Optimization of Fin Louver Design Based on CFD*. SAE Paper 970832, 1997.
- [51] Achaichia A. Cowell T.A. *Heat Transfer and Pressure Drop Characteristics of Flat and Louvered Plate Fin Surface*. Journal of Experimental Thermal and Fluid Science, 1:147-57, 1988.
- [52] Junjanna C. Kulasekharan N. Purushotham H.R. *Performance Improvement Of A Louver-Finned Automobile Radiator Using Conjugate Thermal CFD Analysis*. International Journal of Engineering Research and Technology 1 Issue 8, 2012.
- [53] Gullberg P. *Optimisation of the Flow Process in Engine Bays - 3D Modelling of Cooling Airflow*. PHD Thesis, ISSN 0346-718X, Chalmers University of Technology, Sweden, 2011.
- [54] <http://www.ruijsink.nl/rdehoofd.htm>, May 2013.
- [55] Holman J.P. *Heat Transfer*. 8th Edition, McGraw-Hill, 2002.
- [56] Ng E.Y. Johnson P.W. Watkins S. *An Analytical Study on Heat Transfer Performance of Radiators With Non-Uniform Airflow Distribution*. Journal of Automobile Engineering, Vol. 219, No. D12, 2005.
- [57] <http://www.wwwmetrics.com/shopping.htm>, December 2014.
- [58] <http://www.ideiasustentavel.com.br/pdf/file51139.pdf>, December 2014.
- [59] Henriksson L. Dahl E. Gullberg P. Contet A. Skåre T. Löfdahl L. *CFD Simulation and Experimental Investigation of Pressure-Drop Through 90° and 30° Angled Compact Heat-Exchangers Relative to the Oncoming Airflow*. VTMS11, 2013.
- [60] Wamei L. *Modeling and Performance Analysis of Alternative Heat Exchangers for Heavy Vehicles*. PHD Thesis, ISSN 0282-1990, Lund University of Technology, Sweden, 2014.
- [61] LaGrandeur J. Crane D. Hung S. Mazar B. Eder A. *Automotive Waste Heat Conversion to Electric Power using Skutterudite, TAGS, PbTe and BiTe*. International Conference on Thermoelectrics, pp. 343-349, 2006.
- [62] Beamer H.E. Ghosh D. Bellows K.D. Huang L.J. Jacobi A.M. *Applied CFD and Experiment for Automotive Compact Heat Exchanger Development*. SAE Paper 980426, 1998.

- 
- [63] Larsson L. Martini H. *Aerodynamic Drag Reduction of a Heavy Vehicle with Variable Cooling Air Intake Area*. Master's Thesis, ISSN 1652-8557, Chalmers University of Technology, Sweden, 2009.
- [64] Wamei L. *Modeling and Performance Analysis of Alternative Heat Exchangers for Heavy Vehicles*. Licentiate Thesis, Lund University of Technology, Sweden, 2011.
- [65] Dahl E. Volvo gtt, personal communication, September 2011.
- [66] <http://www.titanx.com>, August 2011.
- [67] Paish M.G. Stapleford W.R. *A Study to Improve the Aerodynamics of Vehicle Cooling Systems*. MIRA Reports, Nos. 1966/15, 1966 and 1968/4, 1967.
- [68] Söderblom D. *Investigation of Wheel Housing Flow on Heavy Trucks*. Licentiate Thesis, Chalmers University of Technology, Sweden, 2009.
- [69] Pope A. Harper J. *Low-Speed Wind Tunnel Testing*. John Wiley and Sons Inc., 1966.
- [70] Baeder D. Indinger T. Adams N. Decker F. *Comparison of Numerical Simulations with Experiments of Bluff Bodies Including Under-Hood Flow*. SAE Paper 2011-01-0171, 2011.
- [71] Fernández A.L. *Heat Recovery from Diesel Engines in Vehicles by using Rankine Cycles for Power Production*. Master's Thesis, Chalmers University of Technology, Sweden, 2010.
- [72] Othmer C. *CFD Topology and Shape with Adjoint Methods*. Internationaler Kongress, VDI Fahrzeug - and Verkehrstechnik 13, 2006.
- [73] Barnard R.H. *Theoretical and experimental investigation of the aerodynamic drag due to automotive cooling systems*. Proc. Institute of Mechanical Engineers, ImechE, Vol 214, Part D, 2000.
- [74] Hucho W.H. *Aerodynamik des Automobils*. 5th Edition, Vieweg and Sohn Verlag/GWV Fachverlage GmbH, 2005.
- [75] <http://www.beodom.com/en/education/entries/peak-oil-the-energy-crisis-is-here-and-it-will-last>, September 2011.
- [76] <http://www.dieselnet.com/standards/eu/hd.php>, June 2011.
- [77] Chronéer Z. Volvo gtt, personal communication, May 2011.
- [78] Mlinaric P. *Investigation of the Influence of Tyre Deformation and Tyre Contact Patch on CFD Predictions of Aerodynamic Forces on a Passenger Car*. Master's Thesis, Chalmers University of Technology, Sweden, 2007.
- [79] Gullberg P. Sengupta R. *Axial Fan Performance Predictions in CFD, Comparison of MRF and Sliding Mesh with Experiments*. SAE Paper 2011-01-0652, 2011.

- [80] Shih T.H. Liou W.W. Shabbir A. Yang Z. Zhu J. *A new k-epsilon Eddy-Viscous Model for High Reynolds Number Turbulent Flows*. Journal of Model Development and Validation, Computers and Fluids, Vol. 24, Nr 3, pp. 227-238, 1995.
- [81] Gullberg P. Löfdahl L. Adelman S. Nilsson P. *An Investigation and Correlation Method of Stationary Fan CFD MRF Simulations*. SAE Paper 2009-01-3067, 2009.
- [82] Larsson L. Dahl E. Wiklund T. Löfdahl L. *Continuing Cooling Performance Investigation of a Rear Mounted Cooling Package for Heavy Vehicles*. SAE Paper 2011-01-2285, 2011.